Directed Assembly Techniques for Nano-Manufacturing of Scalable Single Walled Carbon Nanotube based Devices

A Dissertation Presented

by

Prashanth Makaram

to

The Department of Mechanical and Industrial Engineering

in partial fulfillment of the requirements

for the degree of

Doctor of Philosophy

in the field of

Mechanical Engineering

Northeastern University

Boston, Massachusetts

January, 2009

Abstract

Single Walled Carbon Nanotubes (SWNTs) are being considered building blocks for next generation electronics due to their unique electrical, mechanical and thermal properties. A number of SWNT based devices including scanning probes, field emitters, field effect transistors, biological and chemical sensors, and memory devices have been demonstrated. Despite successful demonstration of these single devices, the success of SWNT based nanoelectronics is hampered due to the lack of a successful nano-manufacturing method. Precise alignment and placement of SWNTs is necessary for successful integration of SWNTs into nanoelectronics.

The work described in this thesis is focused on developing electric field assisted assembly techniques for precise placement and controlled orientation of SWNTs. In a first set of experiments we evaluate the use of micro/nano finger shaped metal electrodes to assemble SWNTs. Eventhough this assembly technique help in understanding the electrophoretic behavior of SWNTs, problems related with orientation, assembly at nanoscale and electrode degradation demanded evaluating alternative techniques.

Nanotemplates that use trenches made in PMMA on a conductive substrate are utilized for the directed, controlled assembly of SWNTs This technique uses a combination of electrophoretic forces and fluidic forces to assemble and align the SWNTs. We were able to assemble SWNTs in trenches that are as small as 80 nm wide and 100,000 nm long over a 2.25 cm^2 area in 30-90 seconds. Based on the experimental results and analysis a model is proposed to explain the assembly and alignment mechanism of SWNT s. The technique has been utilized to fabricated interconnects and field effect transistors to demonstrate the feasibility to make devices.

Finally we introduce a novel room temperature assembly technique for fabricating a three dimensional single walled carbon nanotube platform. A top down lithographic approach is used to fabricate the platform while a bottom-up dielectrophoresis method is used to assemble the SWNTs in a 3D architecture. This is a scalable, high throughput and room temperature technique making it compatible with current CMOS technology. We demonstrate the ability to precisely control the density of SWNTs. A finite element model is used to simulate and study the behavior the SWNTs during assembly. We also demonstrate that these structures can be utilized directly as 3D interconnects. Finally, we show that the packaging of these devices, using a conformal pin-free parylene layer, provides a complete process flow for making SWNT based 3D nano-devices.

Dedicated to my parents, family and friends

Acknowledgement

It is a pleasure to acknowledge the people who helped and motivated me along the way to the completion of this thesis.

First and foremost, I would like to thank my adviser Prof. Ahmed Busnaina, for his guidance and patience during my time at NEU. I enjoyed the independence and freedom I got in the lab to pursue my ideas.

There are many collaborators at NEU and elsewhere who deserve my gratitude. I would like to thank Prof. Yung Joon Jung for his knowledge and guidance on carbon nanotubes, Prof. Mehmet Dokmeci, for the work on 3D nanotube architectures and Prof. Nick McGruer for his guidance with the electrical engineering part of my research. I also want to thank the people at Nantero especially Dr. Ramesh Sivarajan and Dr. Brent Segal for providing the nanotubes and related information. It was a great pleasure working with Selvapraba Selvarasah on the 3D nanotube architecture project. I am greatly indebted to Dr. Jaun Aceros, Andy Pamp, Tae Hoon Kim, Peter Ryan, MyungGHwan Ham, Salome Siavoshi and Cihan Yilmaz for invaluable discussions and companionship within and outside the lab. Special thanks to Dr. Xugang Xiong for his expertise with the electrophoretic assembly of particles. Working in an interdisciplinary research group wouldn't have been easier without the help and knowledge of all the post docs, Dr. Nam Goo Cha, Dr. Steve Ryle, Dr. Sivasubramanian Somu and Dr. Yolanda. I would also like to thank all the current and past graduate students for making our lab a friendly and fun environment to work. Special thanks to Scott McNamara and David McKee for their invaluable help with fabrication and in the cleanroom. I also want to extend my thanks to all the collaborators at UNH and UML. Outside the lab I

am very thankful to the many friends that I had over the years who helped in maintaining my sanity and get through my PhD.

I owe a large debt of gratitude to my parents Dr. Singaperumal and Mythily for all the support they have given me in various endeavors in my life. I am also very grateful to my relatives and family, especially my younger brother Harish, my cousin Ramesh and my uncle Dr. Raghunandan for their constant support and encouragement.

Contents

1. Chapter 1: Introduction 1
   1.1. Nanotechnology 1
   1.2. Carbon Nanotubes and Moore's Law 2
   1.3. Carbon Nanotubes 2
   1.4. Manufacturing of Carbon Nanotubes 5
      1.4.1. Arc Discharge Method 5
      1.4.2. Laser Ablation Method 6
      1.4.3. Chemical Vapor Deposition 7
      1.4.4. Ball Milling 8
   1.5. Carbon Nanotube Purification and Functionalization 9
   1.6. Nanotube Electronics 10
   1.7. Top – Down and Bottom-Up Nanomanufacturing 12
   1.8. Top-Down Methods: 13
      1.8.1. Photo-lithography 13
      1.8.2. Electron Beam Lithography 15
      1.8.3. Nano-Imprint Lithography 17
   1.9. The Necessity of Assembling CNTs 18
   1.10. Assembly Techniques for Carbon Nanotubes 20
      1.10.1. Direct Synthesis of CNT 20
      1.10.2. Post- Synthesis Assembly of CNTs 22
2. Chapter 2: Background 28
   2.1 Van der Waals Force 28
   2.2 Surface Tension Force due to Trapped Liquid 30
   2.3 Hydrodynamic Drag Force 32
   2.4 Electric Field Assisted Assembly 36
      2.4.1 Electrophoresis 36
      2.4.2 Dielectrophoresis 41
   2.5 Fluidic Assembly 46
3 Chapter 3: Assembly on Interdigitated Finger Electrodes 48
   3.4 Introduction 48
   3.5 Experimental Procedure 49
      3.5.1 Fabrication of Microelectrodes 49
      3.5.2 Fabrication of Nanoelectrodes 50
      3.5.3 Preparation of CNT suspension 51
      3.5.4 Procedure 52
   3.6 Results and Discussion 53
      3.6.1 Microelectrode 53
      3.6.2 Nanoelectrodes 57
   3.7 Summary 62
4 Chapter 4: Assembly in PMMA Trench Templates 64
   4.4 Introduction 64
      4.4.1 Preparation of the PMMA Trenches 65
      4.4.2 Procedure 66
   4.5 Results and Discussion 67
      4.5.1 Mechanism of nanotube Assembly and Alignment 71

4.6 SWNT Interconnects ... 91
4.7 SWNT based Field Effect Transistor ... 94
4.7.1 Fabrication of Nanotube FET ... 96
4.8 Summary ... 100
5 Chapter 5: 3D SWNT Architecture Using Dielectrophoresis ... 102
5.1 Introduction ... 102
5.2 Dielectrophoresis ... 106
5.3 Experimental Procedure ... 107
5.3.1 Fabrication of 3D Architecture ... 107
5.3.2 Procedure ... 109
5.4 Results and Discussion ... 109
5.4.1 Assembly on Flexible Substrates ... 112
5.5 Discussion ... 114
5.6 Conclusion and Future Work ... 117
6 Chapter 6: Summary and Future Work ... 119
6.1 Future Work ... 121
Appendix A: Fabrication Materials and Method ... 124
A1. Oxidation and Standard Cleans ... 124
A2. Metal Depostion ... 125
A2.1 Sputtering ... 125
A2.2 Electron Beam Evaporation System ... 127
A3. Lithography ... 128
A4. Etching ... 130
A4.1 Wet Etch of Metal ... 130
A5. Dry Etching of Metals ... 131
A5.1 Ion Beam Milling ... 131
A5.2 Plasma Etching ... 133
Appendix B: Characterization Tools and Techniques ... 135
B1. Imaging ... 135
B1.1 Scanning Electron Microscope ... 135
B1.2 Atomic Force Microscopy ... 136
B2. Contact Angle Measurements,, ... 138
B3. Raman Spectroscopy ... 140
Appendix C: Nanotube Solution ... 143
7 Bibliography ... 147

1. Chapter 1: Introduction

1.1. Nanotechnology

Nanotechnology pertains to the understanding and controlling of matter at dimensions of roughly 1 to 100 nanometers. At nanoscale, the physical, chemical, and biological properties of materials are unique and differ in fundamental and valuable ways from the properties of individual atoms and molecules or bulk matter. Nanotechnology involves making use of the unique properties that exist in this scale for novel applications. A nanometer is one-billionth of a meter. To put it into perspective, the diameter of a single strand of human hair is about 100,000 nm. The chart in figure1 gives a scale of things both man-made and natural.

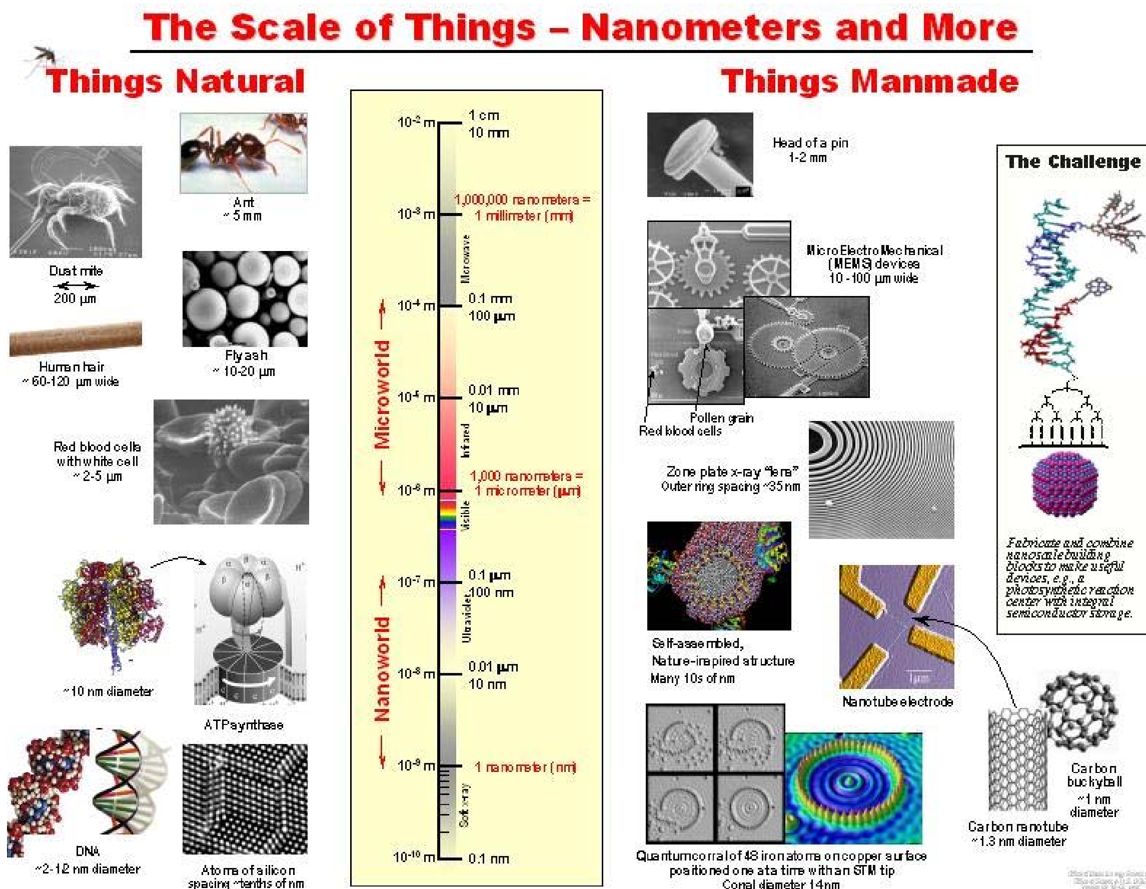

Figure 1.1: Scale of Things

1.2. Carbon Nanotubes and Moore's Law

"The complexity for minimum component costs has increased at a rate of roughly a factor of two per year ... Certainly over the short term this rate can be expected to continue, if not to increase. Over the longer term, the rate of increase is a bit more uncertain, although there is no reason to believe it will not remain nearly constant for at least 10 years. That means by 1975, the number of components per integrated circuit for minimum cost will be 65,000. I believe that such a large circuit can be built on a single wafer." – Gordon Moore[1]. This observation made by Gordon Moore, co-founder of Intel corporation in 1965 translates to the number of transistors that can be crammed on an integrated circuit cost effectively doubles approximately every two years. This law has governed the development in chip technology for the last few decades. Chip makers have been able to keep up with this trend by shrinking components on a chip. Unfortunately miniaturization cannot continue forever and would eventually be limited by physical laws. Researchers around the world are continuously advancing the technology by developing new components and augmenting new materials for silicon. But as components shrink, critical elements like gate dielectric don't perform as well due to tunneling. Currently this has been addressed by replacing SiO_2 with hafnium. But even Hafnium has limitations and the industry and researchers are looking for new materials that can help in going beyond Moore's law. Carbon nanotubes due to their small size and superior electrical properties are excellent candidates for driving the technology beyond Moore's law.

1.3. Carbon Nanotubes

Carbon nanotubes are the most promising building blocks for future nanotechnology products. Carbon Nanotubes exhibit extraordinary strength and unique electrical and thermal

properties making them an excellent candidate for nanoelectronics, optics and a variety of other nanotechnology applications. There structure can be conceptualized as a sheet of graphene (an individual graphite layer) that is rolled into a cylindrical geometry such that the open ends match to form a seamless structure. The rolling of the graphene sheet can be done in several different ways while still satisfying the matching of dangling bonds. A pair of indices called chiral vector can be used to represent this wrapping around of the graphene sheet. The unit vectors a_1 and a_2 denote two directions on the honeycombed crystal lattice of graphene. Depending on the chiral vectors, the nanotubes are called zigzag ($a_2=0$), armchair ($a_1=a_2$) or chiral otherwise. The chirality of the nanotubes controls its electrical properties. There are four popular techniques that are used to produce CNTs, namely arc discharge, laser ablation, high pressure carbon monoxide (HiPco), and chemical vapor deposition (CVD).

Carbon nanotubes generally exist in two modes, single walled carbon nanotubes and multi walled carbon nanotubes. As the name denotes, SWNTs have a single rolled sheet of graphene, whereas MWNTs have multiple concentric cylinders of graphene. SWNT exhibit very important electrical properties that are not shared by MWNTs and thus are likely candidates for future miniaturization of beyond current micro electronic technology. The average diameter of SWNTs is about 2 nm while the average length is 3- 5 μm.

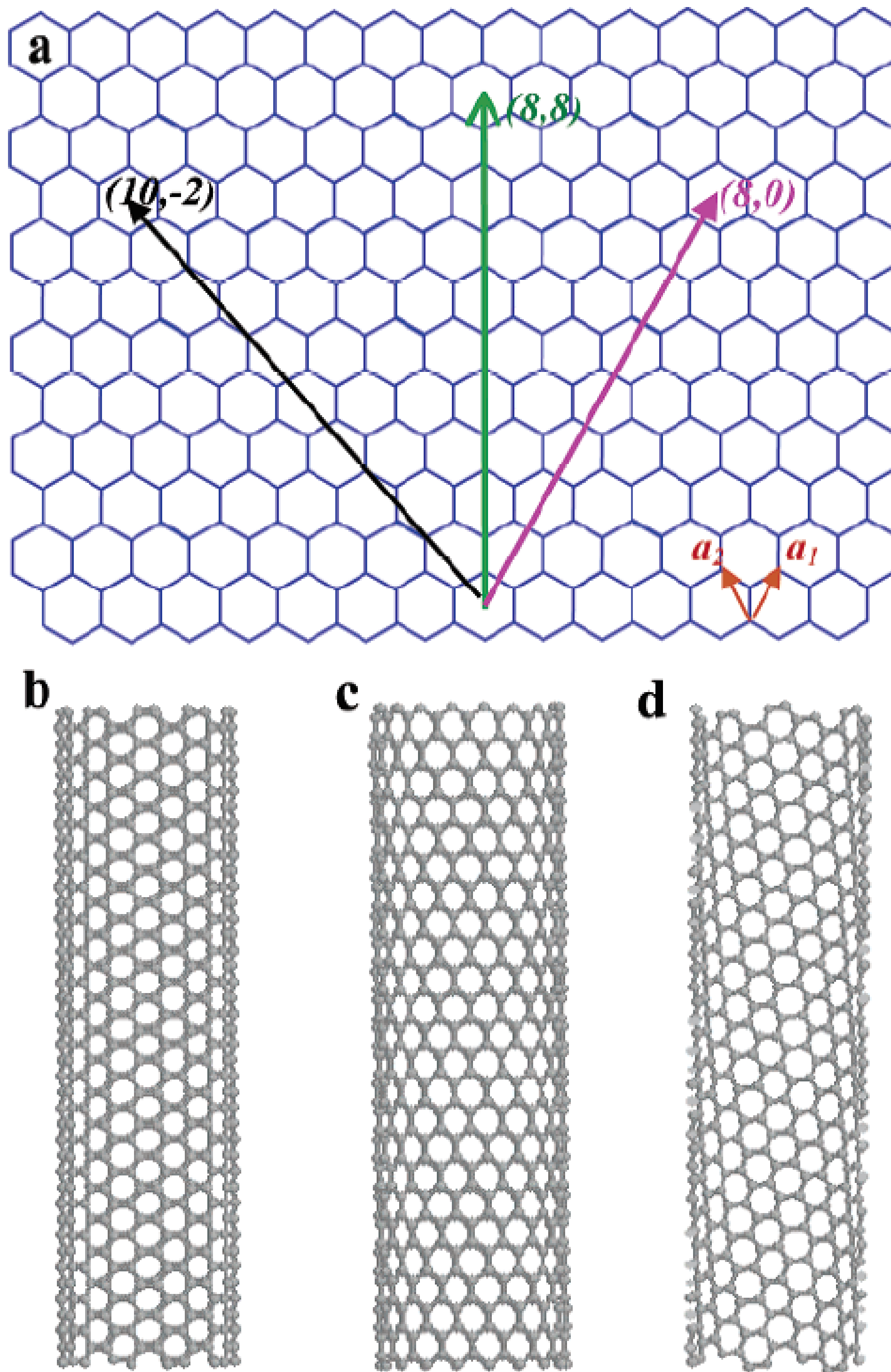

Figure 1.2: (a) Schematic of the honeycombed structure of a graphene sheet. SWNTs are formed by rolling this graphene sheet along lattice vectors (a_1, a_2). Folding along lattice vectors (8,8), (8,0) and (10,-2) leads to formation of (b) armchair, (c) zigzag and (d) chiral tubes, respectively[2].

1.4. Manufacturing of Carbon Nanotubes

Carbon nanotube manufacturing from beginning to end consists of many steps, with large number of processing parameters and highly coupled processes. The first step in SWNT manufacturing is the growth process. Currently there are four major techniques to grow SWNTs.

1.4.1. Arc Discharge Method

Arc discharge method was the first method used to grow carbon nanotubes. It was used by Ijima[3] in the very first experimental result, where he showed carbon nanotubes can be formed on graphite electrode for fullerene synthesis. This method yields about 30 percent by weight and it produces both single- and multi-walled nanotubes with lengths of up to 50 microns[4]. The method uses two graphite rods (anode and cathode) as electrodes to create plasma in an inert atmosphere. When the rods are brought close in an atmosphere containing He or Ar gas at 3500 ºC, a discharge occurs resulting in the formation of plasma. The anode is consumed by plasma and ionized carbon atoms are attracted to the graphite cathode. Rod like deposits is formed on the cathode containing MWNTs, fullerenes, amorphous carbon and polyhedron carbon species. Synthesized MWNTs are usually very straight and have lengths on the order of microns and diameters in the range of 5 to 30 nm and they usually exist in bundles.

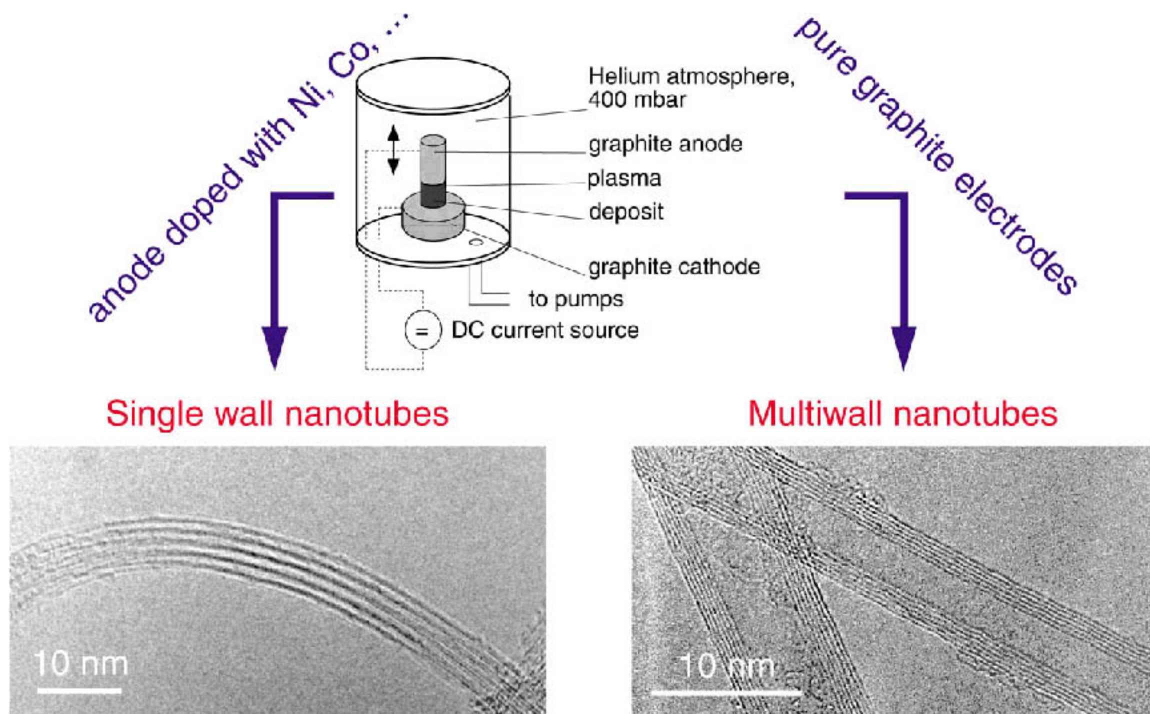

Figure 1.3: Schematics of an arc-discharge apparatus, along with electron microscopy pictures of the products obtained with doped and pure anodes.

Unlike MWNTs, SWNTs require metal catalysts and dense carbon vapor[5, 6]. A hole is drilled in the anode and packed with the mixture of the metal catalysts (Ni and Y) and graphite powder in the specific ratios. Rapid growth of SWNTs occurs as soon as plasma is formed. The SWNTs form web like networks inside the reaction chamber. This technique has been the mostly widely used technique for synthesis of SWNTs and MWNTs.

1.4.2. Laser Ablation Method

Compared to the Arc discharge method, laser ablation method produces large amount of nanotubes, gram scale can be obtained[7]. The method involves heating of a carbon target containing about 0.5% Ni and Co in a tube furnace. Intense laser pulses are used to ablate the target under inert conditions. The nanotube is collected onto a water cooled target using inert gas flow. Ropes consisting of tens of individual SWNTs are produced by this method. The

yield from this method is around 70% and produces primarily single-walled carbon nanotubes. The diameter is determined by the reaction temperature. However, it is more expensive than either arc discharge or chemical vapor deposition[4].

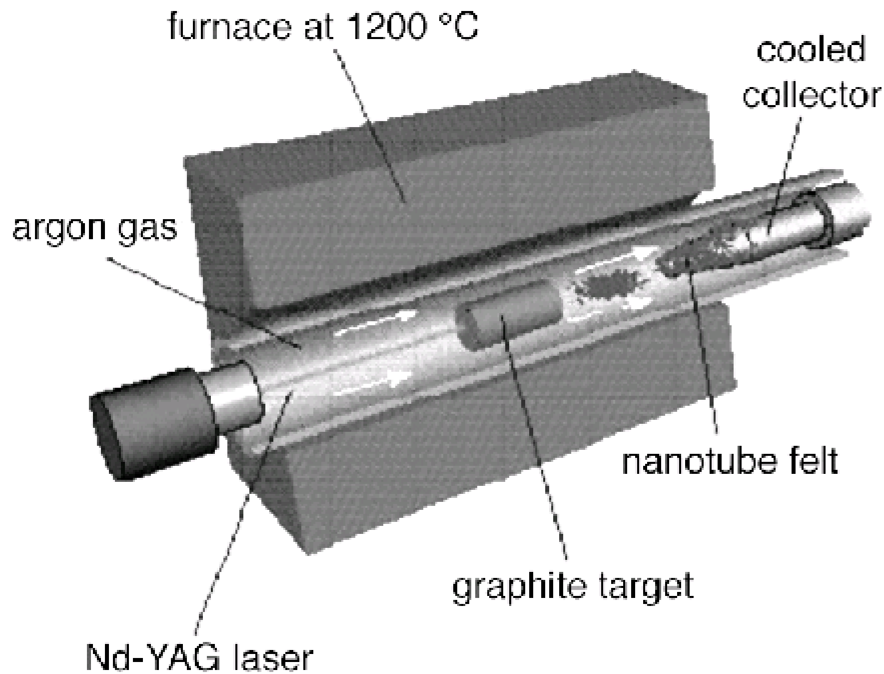

Figure 1.4 Schematics of a laser ablation set-up[8].

1.4.3. Chemical Vapor Deposition

CVD growth process is becoming a strong candidate for the large scale production of CNTs due to their ability to overcome limitations like high temperature requirements and low yield. CVD growth involves heating catalyst materials to temperatures between 500 ºC and 1200 ºC in a tube furnace while flowing hydrocarbon gases for a certain period of time[9,10]. MWNT growth involves the catalytic decomposition of hydrocarbon gases such as acetylene, ethylene, xylene, or benzene by catalytic nanoparticles (such as Ni, Co and Fe) at temperatures between 500 ºC and 800 ºC[11,12] This result's in high density of vertically aligned MWNT growth. The SWNT growth requires higher growth temperature and

smaller catalytic particle size compared to MWNT growth. The length scale of SWNTs is generally in the range of a few microns to centimeters and can be controlled by the growth time and synthesis method.

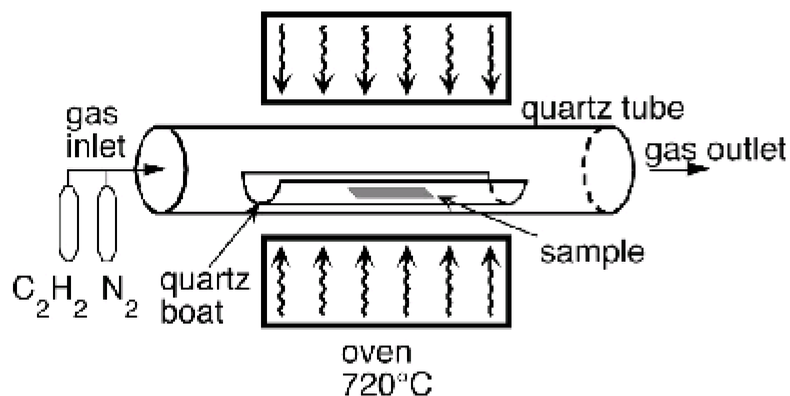

Figure 1.5: Schematics of a CVD deposition oven.

1.4.4. Ball Milling

Ball milling is a simple method for the production of CNTs. It is usually accompanied with an annealing step. The method involves placing of graphite powder into a stainless steel container along with four hardened steel balls. The milling takes place in an argon environment at room temperature for upto 150 hours. Following which the powder is annealed under an inert gas flow at 1400 °C for six hours. This mechanical attrition leads to the formation of fully nano porous microstructures. Eventhough the mechanism is not fully understood, it is believed that the ball milling process forms nanotube nuclei and the annealing process activates the nanotube growth. This method produces more MWNTs and very few SWNTs[13].

1.5. Carbon Nanotube Purification and Functionalization

As grown CNTs have to be synthesized for proper dispersability and removal of metallic contaminants. Although there has been interesting work reported on carbon nanotube chemistry, the research on the chemical modification of carbon nanotubes is still in its infancy. Carbon nanotube walls are rather unreactive due to the seamless arrangement of hexagon rings without any dangling bonds. Like C_{60} fullerene, the nanotubes are known to be more reactive at their tips than at their cylindrical walls[14]. Following growth an oxidation step is used to open the hemispherical end-cap. Early work used gas-phase reactions with air, O_2, CO_2, N_2O, NO, NO_2, O_3 and ClO_2[15]. Unfortunately amorphous carbon impurities were found to be more susceptible to gas phase reaction. Solution-state chemical oxidation was found to be more efficient for purification and/or modification of CNTs. Various oxidants including HNO_3[16,17, 18, 19], HNO_3 + H_2SO_4[20], $HClO_4$[21] , H_2SO_4 + $K_2Cr_2O_7$[22] and H_2SO_4 + $KMnO_4$[23] have been shown to react with carbon nanotubes. These oxidation reactions often generate various functional groups (e.g. –COOH, -OH, - C=O) at the opened end or defect sites of the CNT structure. Since SWNTs tend to exist in bundles, the oxidation reactions take place at the nanotube end-tips and the outer layer of the bundle. Use of mechanochemical reactions can generate highly reactive centers by mechanical energy (ultrasonication or ball milling). Use of ultrasonics has been used to create many defect sites on the SWNT sidewalls to facilitate the oxidation reaction as well as cleave them into shorter segments[24]. The use of ultrasonics also results in the formation of coils with very narrow distribution of radii (300-400nm)[25].

The oxidized sites have been exploited for binding polymers onto nanotubes, better dispersion of the nanotubes into polymer composites, and site selective assembly and

alignment of SWNTs. We are particularly interested in the oxidation sites, due to the fact that these –COOH sites provide a negative charge to the basically uncharged SWNTs. Hence they can be driven under an influence of an electric field.

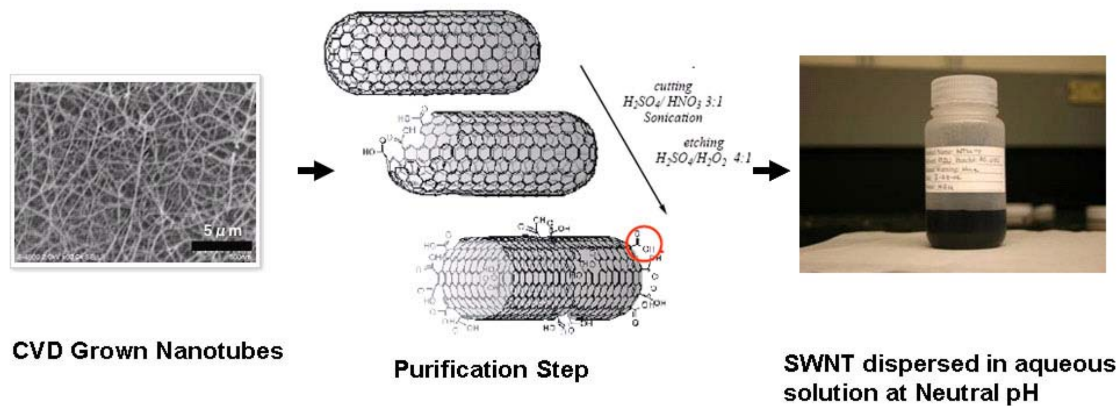

Figure 1.6: Purification and dispersion of SWNT

1.6. Nanotube Electronics

SWNTs exist as either semiconductors or metals, and their electrical properties are far better than the best metals or semiconductors[26]. They exhibit what is called ballistic properties (the electrons are not impeded or scattered by obstacles). Also SWNTs are far thinner than metal interconnects. The electrical properties of metallic nanotubes were first studied by Tans et. al.[27] and Bockrath et. al.[28], while semiconducting tubes were studied later by Tans et. al.[29]

Researchers have demonstrated a plethora of device applications exploiting the extraordinary properties of SWNTs. SWNTs due to their unique electrical and physical properties are emerging as a viable electronic material for future electronic devices. Infact the ITRS roadmap proposes the use of SWNTs for future interconnects. Intel, IBM and other major electronic manufacturers are eyeing carbon nanotubes for future chip designs. Some of the proposed SWNTs based devices include logic elements, field emitters, interconnects,

memory switches etc. SWNTs have excellent field emission capabilities due to their high electrical conductivities and incredible sharpness of their tips, thus making them ideal candidates for field emitters in flat panel displays, cold-cathode lighting sources, lightning arrestors and electron microscope sources. Semiconducting SWNTs are excellent candidates for making field effect transistors. The nanotube can be switched from a conductive to an insulating state by applying appropriate gate voltage[30]. Thus they can be used as logical switches to make basic components of computers. Researchers have also demonstrated single electron transistors[31], and have doped the SWNTs to create n-type transistors[32], p-n junctions[33] and p-n-p devices[34]. Combining SWNTs mechanical properties with their electrical properties would lead to SWNT based electromechanical actuators for artificial muscles and other NEMS applications. Nantero Inc. is trying to commercialize memory devices based on electronmechanical actuation of SWNTs. SWNTs are being explored as filler materials to make conductive plastics due to their high aspect ratio and their tendency to form ropes providing very long conductive pathways even at ultra-low loading. This finds applications in EMI/RFI shielding composites, electrostatic dissipation, antistatic materials, transparent conductive coatings, and radar absorbing materials for stealth applications. Finally SWNTs are being explored for a variety of sensor applications.

1.7. Top – Down and Bottom-Up Nanomanufacturing

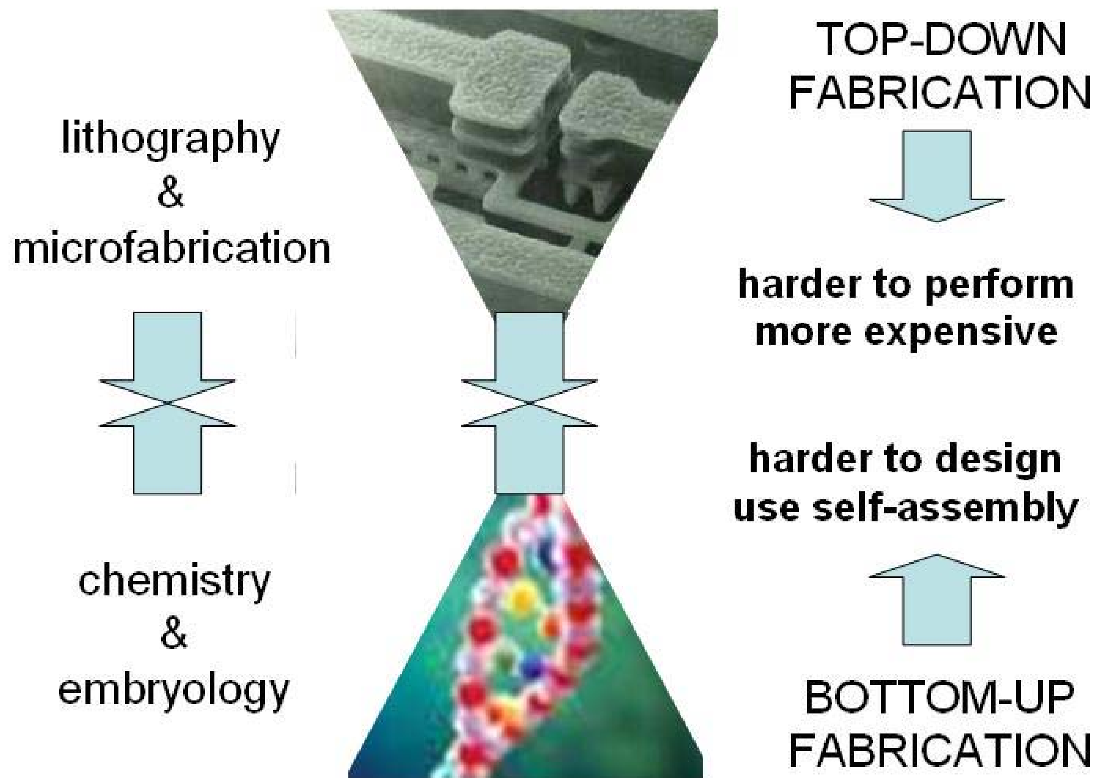

Figure 1.7: Montage.Nanofabrication can push the limits of microlithography as one tries to push procedures to smaller and smaller scales. Alternatively, you can start small, at the molecular level, and work up[35]. (Two basic approaches to nanomaterials fabrication: from left to the right) and bottom-up (from right to the left).[36])

There are two general ways available to produce nanomaterials, as shown in the figure 1.7. The first approach starts with a bulk material and then breaking it into smaller pieces using mechanical, chemical or other form of energy (top-down). An alternative approach involves synthesising the material from atomic or molecular species via chemical reactions, allowing for the precursor particles to grow in size (bottom-up).

Bottom-up approach involves specifying the individual base elements in great detail. A large sub system is formed by linking together these elements. Which is then linked together sometimes in many levels, until a complete top-level system is formed. Bottom up

approach can be thought of as building a car engine up from individual components rather than machining a system from a large block of material. Bottom-up approach or self assembly uses chemical or physical forces operating at the nanoscale to assemble basic units into larger structures. In recent years, a number of bottom-up approaches have been developed for synthesis of nanoparticles and nanotubes. Directed assembly techniques such as patterning, templating and surface functionalization have been used to assemble nanotubes and nanoparticles.

1.8. Top-Down Methods:

1.8.1. Photo-lithography

Photo-lithography technique is the mostly widely used fabrication technique for making integrated circuits in the IC industry. It involves a variety of physical and chemical processes. A lithographic system comprises of an exposure tool, a mask or reticle, resist, and all of the processing steps to accomplish pattern transfer from a mask to a resist and then to devices. The word photo-lithography is derived from photography and conventional lithography technique used in printing due to its similarity to these techniques. It uses visible or ultraviolet light to transfer a geometric pattern from a photomask onto a light sensitive chemical called photoresist. The photomask or reticle is usually composed of glass and chromium. The photoresist are classified into two types, positive photoresist and negative resist. When positive resist is exposed to light, it becomes soluble to the photoresist developer leaving the part of the photoresist that is unexposed on the substrate. Whereas a negative photoresist when exposed to light becomes relatively insoluble to the photoresist developer and the unexposed parts are dissolved by the photoresist developer. Positive

resists are preferred over negative resist, as in negative resists the developed areas swell while undeveloped area is being dissolved resulting in distortion in patterned features.

Conventional exposure system or printing can be of two types, direct contact called contact aligner or with a small gap called proximity aligner. The resolution is approximately the squre-root of the product of the wavelength and the gap distance. Hence direct contact method gives a higher resolution that proximity aligner. Current approach for photolithography uses a technique called projection lithography. A scanner or stepper is used to project the desired pattern from the photomask onto the wafer. The technique uses a system of complex lenses to focus light from a mercury arc lamp or excimer laser onto a mask from where it is projected onto the wafer through a reduction lens system.

Optical lithography is suited for its low cost, high throughput and control over the shape and size of the objects it creates areas as large as 300 mm. A complex integrated circuit fabrication such as CMOS involves atleast 50 cycles of the photographic steps.

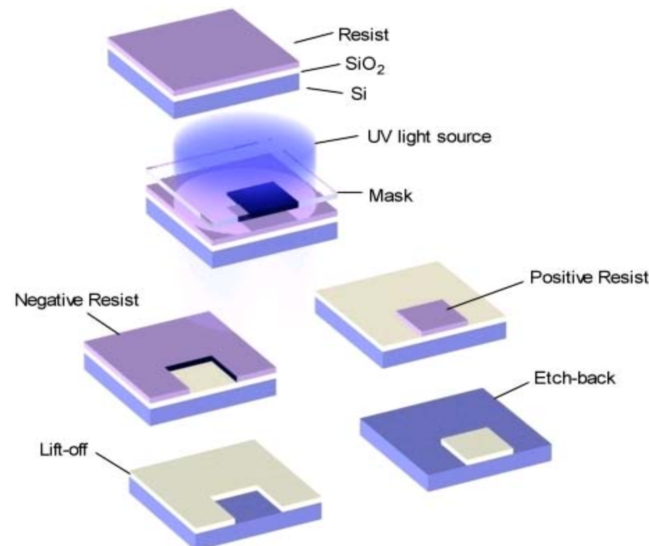

Figure 1.8: Basic Optical lithography process

Unfortunately optical lithography is limited in the minimum feature size that it can produce by the wavelength of the light used. Hence it cannot be used to create nanoscale features. Recent developments to increase the numerical aperture by using fluid as the transmission medium called immersion lithography and using extreme ultra violet and x-ray systems have helped in reducing the minimum feature size to 30 nm.

1.8.2. Electron Beam Lithography

Electron beam lithography on the other hand can be used to overcome the diffraction limit of light to make features in the nanometer regime as it uses a beam of electrons to generate patterns on the surface. This lithography technique uses something known as an electron beam resist. Similar to the optical resists, there are positive and negative electron beam resist. The electron beam scans over the surface exposing the desired areas on the resist. When a positive resist is used, the exposed areas get dissolved on exposure, while the exposed area stays when using a negative resist. The pattern generation is serial and hence very slow making this process unsuitable for high volume process. Hence the EBL process is limited to usage in mask-making (for optical lithography), low volume production of semiconductor components and research and development.

A typical EBL system consists of an electron gun that supplies the electrons, an electron column that shapes and focuses the electron beam, a mechanical stage to position the wafer under the electron beam, a wafer handling system to automatically load and unload the wafer and a computer system to control the equipment. Most commercial applications use dedicated systems, while in research applications it is very common to a scanning electron microscope into a EBL system with accessories.

Electron beam widths down to a few nanometers can be routinely obtained with todays optics. However the practical resolution is limited by forward scattering in the photoresist and secondary electron travel in the photoresist and not by the beam size. Higher energy electrons or thinner photoresist can be used to reduce the forward scattering, but the secondary electron generation is inevitable. In addition back scattered electrons, primary electrons that have sufficient energy to penetrate the photoresist and scattered over large distances from the underlying films and/or substrate, leads to exposure of areas at a significant distance from the desired exposure location.

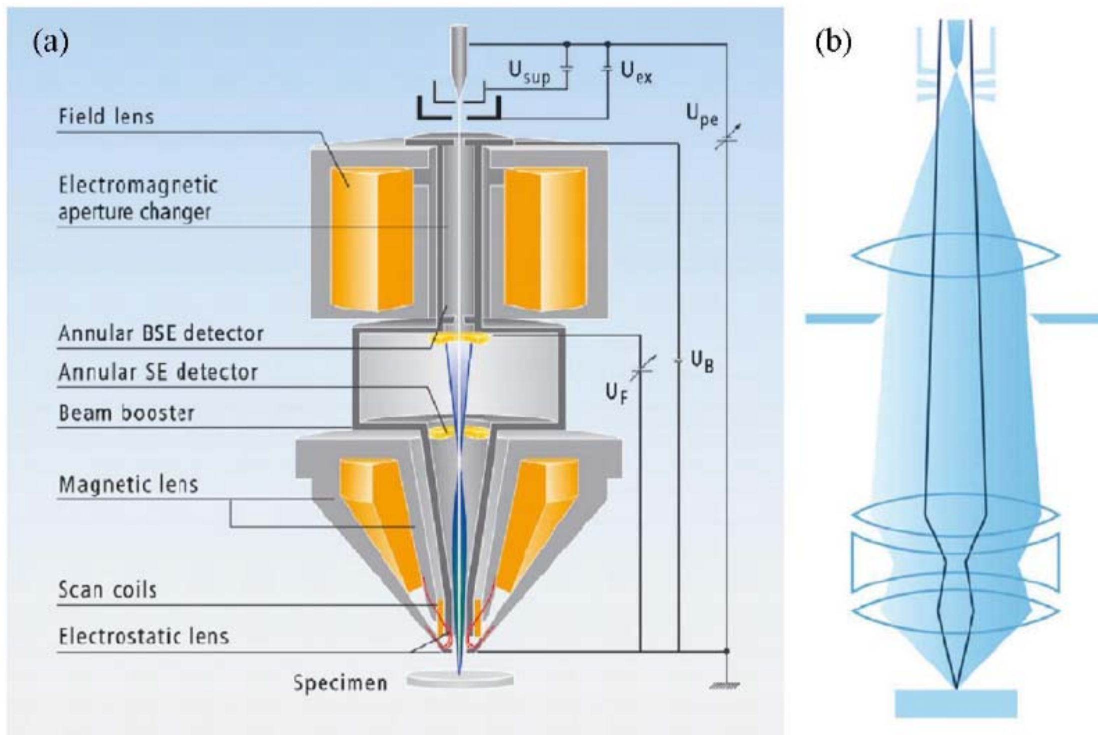

Figure 1.9: A basic Ebeam System

1.8.3. Nano-Imprint Lithography

Nanoimprint a novel process that uses physical contact and mechanical deformation of the resist to create patterns. It is a low cost, high throughput method to make nano-scaled features. Similar to non contact methods, the NIL resist is a monomer or a polymer formulation that is cured by heat or UV light during imprinting. For proper release of the mold from the substrate it is important to control the adhesion between the resist and the mold. This can be achieved by the use of proper anti-stiction coatings. The mold used is generally Si or Ni with the mirror image of the pattern to be fabricated etched on it.

Currently there exists many different types of NILs, among them thermoplastic NIL (T-NIL) and step and flash Imprint lithography (S-FIL) are the most widely used ones. T-NIL is the earliest and most mature nano-imprint lithography process. It was developed by Prof Chou's group. It uses a mold with predefined topography that is brought in contact with a substrate that has been spin coated with a thin layer of resist. Under certain conditions of pressure and temperature, the pattern gets pressed into the melted polymer film. The pattern transfer process is complete once the system is let to cool and mold is removed. The S-FIL uses a UV curable resist and thus needs a mold made of transparent material like fused silica, quartz etc. After the mold and substrate are brought in contact, the resist is cured in UV light and becomes solid. The mold is separated to complete the pattern transfer process. This technique can be performed similar to the step and repeat process in optical lithography. The imprint die is moved across the wafer to complete the pattern from the die onto the entire wafer.

Nanoimprint lithography doesn't make use of complex optics or high energy radiation sources. Also it doesn't require any tailored photoresists designed for both sensitivity and

resolution at a given wavelength. Thus making this process simple and cost effective. Hence the ITRS roadmap now includes NIL to be employed for 35 nm node. NIL is finding applications in fabrication of devices for electrical, optical, photonics and biological applications.

Though NIL seems to be a promising technology, there are some concerns in overlay, defects and template patterning that need to be addressed. The direct contact involved, magnifies the potential for errors in overlay and defects. One way to overcome this is to use cleaning strategies between imprinting steps. Other concerns are residual resist left behind after imprinting and stiction of the resist to the mold after imprinting.

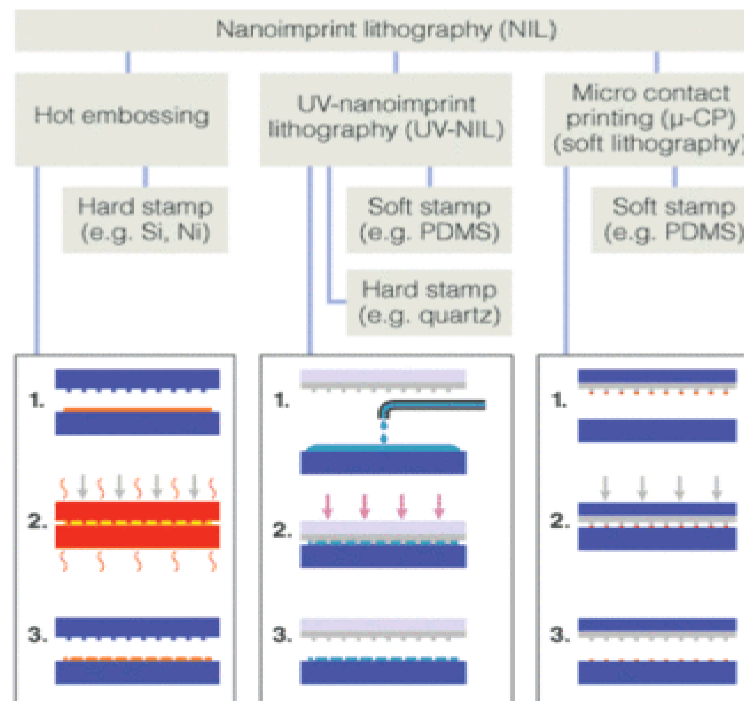

Figure 1.10: Standard Nanoimprint lithography process flow

1.9. The Necessity of Assembling CNTs

Nanoscale electronics based on carbon nanotubes (CNT) are smaller and more versatile than conventional complementary metal oxide semiconductor (CMOS) electronics. The

remarkable electronic and physical properties of CNTs make them a promising building block for future nanoscale devices, which may help in overcoming fundamental physical and economical limitations of conventional Si-based VLSI (very large scale integration) fabrication techniques. Various CNT based devices including scanning probes[37], field emitters[38], field effect transistors[39], biological sensors[40], chemical sensors[41] and memory devices[42] have been fabricated and studied. It would seem reasonable that with demonstration of all these exciting electronic applications, SWNT should find immediate commercial applications. Unfortunately despite demonstration of these single device prototypes, the challenge for successful commercialization of SWNT based nanoelectronics lies in the issue of device manufacturability. To be used as active components (such as transistors or sensing elements) or other device components (such as interconnects) CNTs needed to be assembled in hierarchical arrays. All the technological demonstrations for SWNT devices lack a technique that enables the fabrication of complex architectures for system level integration. At nanoscale placing of nanotubes at desired locations with targeted shapes, directions and densities for fabricating functional devices still remains a challenge.

In addition to this major hurdle, other issues that need to be addressed but is beyond the scope of this work are:

Tube Synthesis: Although tremendous work has been done in tube synthesis and diameter control of carbon nantubes, the chirality of SWNTs cannot be controlled. A major issue with current nanotube synthesis is 2/3rd of the SWNTs grown tend to be semiconducting[43] while the remaining are metallic. There has been some modest progress in separating metallic from semiconducting nanotubes using electric field and chemistry.

Nanotube Contamination: Nanotube growth is a very dirty process. A typical nanotube involves catalytic decomposition of carbon containing reaction gases like acetylene and methane, with catalysts such as iron, cobalt and nickel. Further they exist in a complex entangled mesh and have to be separated into individual SWNTs. Thus SWNTs have to go through a series of chemical cleans. This makes them an expensive commodity and might also degrade their electrical properties.

1.10. Assembly Techniques for Carbon Nanotubes

1. Direct Synthesis of CNT
2. Post- Synthesis assembly of CNTs

1.10.1. Direct Synthesis of CNT

Synthetic assembly has been the most widely used technique to make perpendicularly aligned CNTs. CVD growth of CNTs produces perpendicularly aligned CNTs. Dai et. al.[44] has done extensive work on the growth of CNTs using CVD. Recently Ago et. al.[45] prepared highly aligned MWNTs by CVD of acetylene using cobalt nanoparticles casted on a silicon substrate. Maruyama's group published a series of papers related to perpendicularly aligned SWNTs using alcohol based CVD technique[46,47,48,49]. Rao et. al.[50] successfully prepared aligned CNTs on quartz by the pyrolysis of ferrocene. Precise placement of CNTs for further device integration can be achieved by either patterning the catalyst particles or the CNTs themselves. Strategies have been developed to synthesis CNTs on catalytically patterned substrates. Techniques for patterning of the catalyst include patterned photoresists, shadow masks, self assembly, inkjet printing and micro-molding in capillaries. Li et. al.[51] managed to grow perpendicularly aligned and patterned CNTs by CVD on the top and bottom of three

dimensional Poly dimethyl siloxane (PDMS) structures. Legagneux et. al.[52] recently reported a self alignment process for the preparation of individual CNT arrays for making integrated gate nano-cathode. Dai's group[53] used micro contact printing and solvent assisted micro molding techniques to pattern iron phtlocyanide catalysts, and used a novel pyrolysis technique to produce aligned CNTs. Ajayan's group reported an ingeneous method to produce highly site selective growth of CNTs using ferrocene and xylene mixture on lithographically patterned Si/SiO_2 substrates[54].

Synthetic approach for making parallel arrays of CNTs is relatively difficult and has received little attention in contrast to perpendicular synthesis of CNTs. Kroto et. al. generated horizontally aligned CNTs by the pyrolysis of 2 amino, 4,6 dichloro-s-triazine over a thin film of cobalt catalyst patterned on a silica substrate. Han et. al.[55] used a patterned nickel catalyst on Si/SiO_2 substrate for CVD of acetylene. Similar patterning techniques as the perpendicular CNTs can be used for the parallel CNTs too. O Brien et. al.[56] contact printed Fe containing silica precursor solution onto a Si wafer using a micro patterned PDMS. Use of electric fields or magnetic fields in a CVD system can significantly promote the parallel growth of CNTs on substrates. The electric field induced dipole moments originating from the highly anistropic polarizability of a long SWNT results in aligned torques and forces on the nanotubes, thereby preventing randomization of nanotube orientation due to thermal fluctuations and gas flow. Permanent magnets can be used to adhere and align catalyst particles resulting in aligned growth of nanotubes. In addition controlling the direction of gas flow in a CVD system can produce horizontally aligned CNTs.

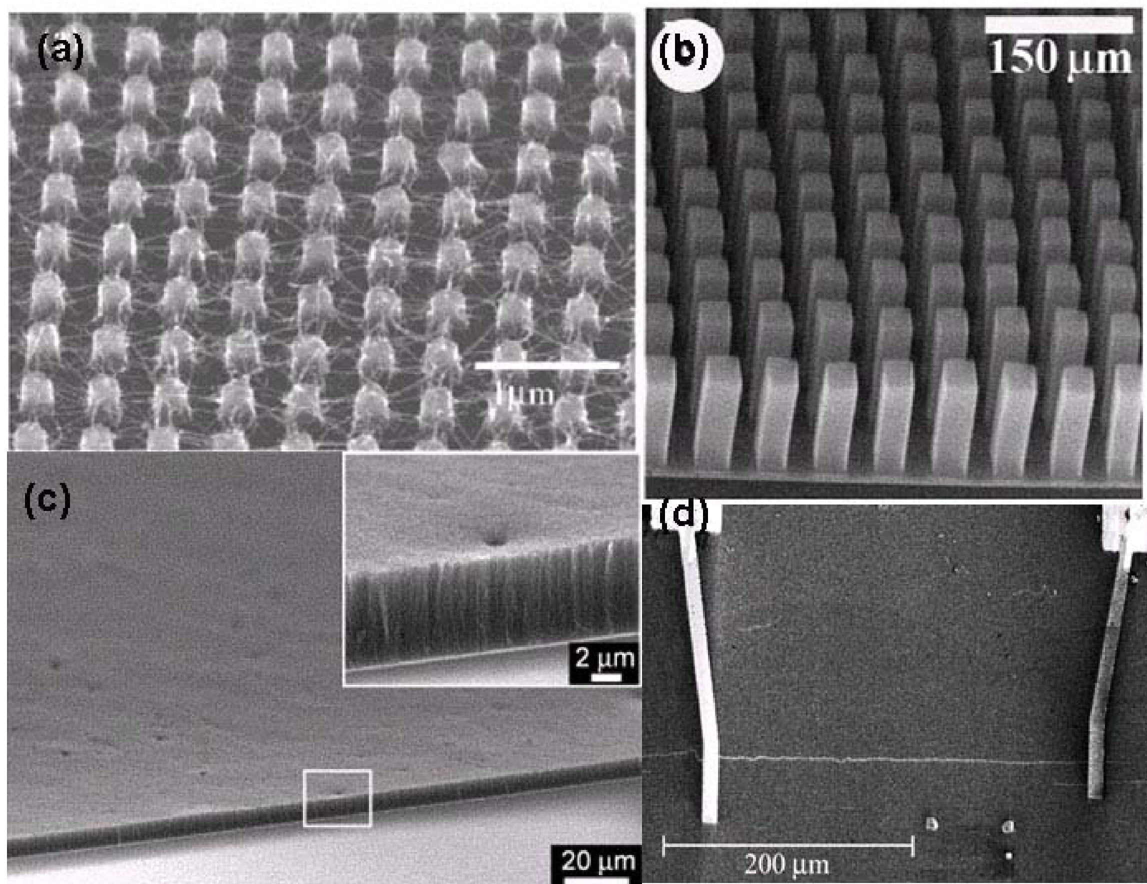

Figure 1.11: SEM images of (a) Nanotubes suspended on pillars[57] (b) Nanotube blocks synthesized on 250µm by 250µm catalyst patterns[9] (c) Nanotube forest (d) Aligned horizontal growth of CNT on iron nanoparticles[58].

1.10.2. Post- Synthesis Assembly of CNTs

Even though post synthesis methods are preferred over synthetic approaches due to their benign temperature requirements, the literature is much smaller due to the difficulty in manipulating the CNTs. Post synthesis involves release of as grown nanotubes by chemical methods and dispersing the CNTs in particular solvents. Hence most post synthesis methods are liquid based. Assembly has been achieved by techniques such as self-assembly of nanotubes on chemically modified surfaces, electric field assisted assembly of nanotubes on nanostructures, and flow induced methods. Chemically modified substrates have been used for both assembling SWNTs parallel and perpendicular to the substrate. Lee et. al. reported a

method in which the surface of a flexible Au/Ti-metalized poly(ethylene terephthalate) (PET) film was modified by a self-assembled monolayer (SAM) of 11-mercaptoundecanoic acid. This was followed by dipping into a solution of $ZNSO_4$ for the ionization of 11-mercaptoundecanoic acid. Immersion of the substrate into a basic shortened nanotube solution resulted in the perpendicular attachment of SWNTs onto the patterned gold surface through a Zn- carboxyl linkage. The strong interaction of NH_2 groups with COOH groups has been exploited to assemble and align SWNTs. Colbert et. al.[59] exploited this NH_2 – COOH interaction to precisely place SWNTs in nanolithographic patterns. Rao et. al.[60] created two distinct surface regions coated polar chemical groups (such as amino (-NH_2/NH_3^+) or carboxyl (-COOH/-COO^-)) and non-polar chemical groups (such as methyl (-CH_3)) by either dip-pin lithography or micro-contact printing. The SWNTs preferentially assembled on the patterned polar regions and directionality originated from the electrostatic interactions. Similarly Tsukruk [61] and co-workers made alternate hydrophilic and hydrophobic stripes by micro contact printing of amine-terminated SAMs and methyl-terminated SAMs to obtain large quantities of straight nanotubes over millimeter scale surface areas. Bughard et. al.[62] used a chemically modified Au/Pd electrode arrays on Si/SiO_2 substrate for controlled adsorption of MWNTs. Liquid flow methods such as Langmuir-Blodgett technique has also been applied to align SWNTs. The nanotubes are spread on the water surface of a Langmuir trough and LB films were deposited on the substrate by either horizontal lifting method or vertical dipping method. Zhou et. al.[63] aligned SWNTs on a hydrophilic substrate (such as glass slides) by vertically immersing the substrate into an aqueous solution of acid-oxidized short SWNTs.

The use of electric field or fluidic flows can help in further aligning nanotubes on substrates with surface modification. For example, by flowing gas over assembled SWNTs on amine terminated surfaces before rinsing the SDS, results in the orientation of SWNTs along the N_2 stream[64]. Similar gas flow technique has been used by Jiao et. al.[65] to align CNTs on various substrates including Si, SiO_2, Cu-coated Si, and even Si with prepatterned electrode structures. Kim et. al. used an electrophoretic technique to assemble SWNTs perpendicularly on pattered indium tin oxide(ITO) on glass substrate. They used $Mg(NO_3)$ to render the SWNTs positively charged in the aqueous solution. Wakaya et. al. and Kumar et. al.[66] have shown that it is possible to assemble CNTs on micro-fabricated metal electrodes using electrophoretic deposition (EPD). While the former suspended the nanotubes in Iso-propyl alcohol, the latter suspended the nanotubes in dimethylformamide. But both of them showed that the nanotubes move towards the anode and the position and density of the assembled nanotube can be controlled by controlling the magnitude of the electric field. Wakaya et. al.[67] have also shown that the electrode on which CNTs deposit during EPD vary with the type of electrolytic solution used and the source of the CNTs. They reported that this confusing situation could arise from the impurities, defects or other unknown factors. Choi et. al.[68] and Gao et. al.[69] have used EPD to fabricate SWNT based field emitters. Choi et. al. suspended SWNTs in distilled water along with $Mg(NO_3)_2 6H_2O$ and deposited them on patterned microelectrodes under a negative bias of 10 – 50 V dc. Whereas Gao et. al. suspended SWNTs in alcohol and Dimethyl fluoride (DMF) and assembled them on unpatterned stainless steel plates under a positive bias of 20 V/cm. They also showed that the deposition rate depended on several experimental factors including concentration of SWNT, the salt and the DC current However EPD assembly of SWNTs using these techniques yield

only randomly distributed and disoriented nanotubes. Kamat et. al.[70] reported a case in which they prepared nanotube suspesions by ultrasonically mixing with tetraoctylaqmmonium bromide (TOAB) in tetrahydrofuran (THF) to prepare charged SWNTs. The TOAB-capped nanotubes became charged under the influence of the dc field and aligned themselves in the field.

Dielectrophoresis on the other hand has been shown to control the aligned SWNTs and has been widely explored for assembling SWNTs[71,72] and has received a lot of attention due to its practicality and effectiveness. Akita's group first assembled CNTs by dielectrophoresis in 1998[73]. They showed that the nanotubes move towards the electrodes for all frequencies of applied field from 10 Hz to 10 MHz. They also showed that at higher frequencies the degree of orientation of nanotubes in higher and the amount of impurities depositing decreases. By suitable varying the electrode design, this technique can be used to obtain arrays of individual CNTs.

According to Lu et. al.[74] SWNTs would align parallel to an impressed magnetic field due to their anisotropic magnetic susceptibility and the lower energy orientation. The first highly aligned SWNTs by this technique was obtained by Colbert et. al.[75] They imposed a 25 T magnetic field while filtering the nanotube/Triton-X suspension through a nylon membrane. Haddon et. al.[76] dispersed Ni-capped MWNTs and aligned them using a very weak magnetic field. Long and co workers[77] assembled parallel arrays of CNTs by using arrays of micromagnetic traps. By manipulating the CNT concentration, device dimension and magnetic field strength, they have been able to achieve individual CNT bridging structure.

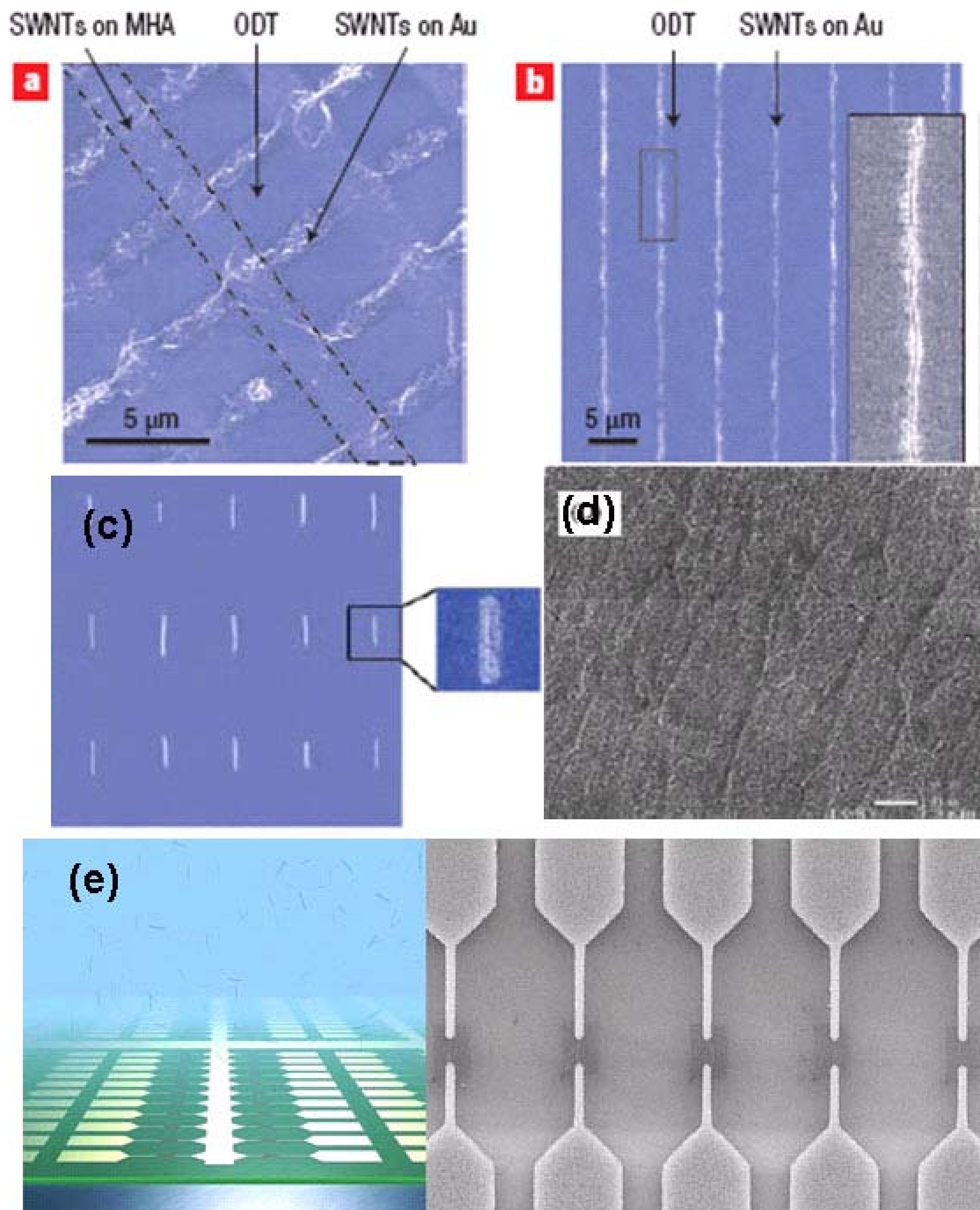

Figure 1.12: (a) & (b) AFM images showing assembly and orientation of SWNTs by a combination of fluidic and chemical methods.[78] (c) AFM image showing large scale assembly of SWNTs on Au surface by chemical functionalization [60](d) SEM image showing electrophoretic assembly of SWNTs[69] (e) Illustration and SEM image showing large scale assembly of single SWNTs by dielectrophoresis[79].

1.11 Motivation and dissertation overview

As noted earlier, there has been plethora of work done in demonstrating single devices using Single Walled Carbon Nanotubes. But the large scale manufacturing of these devices is still hindered by a reliable manufacturing technique that would place these SWNTs at desired locations , orientation and with the required precision at high rate. The goal of this dissertation is to develop a efficient assembly technique that would reliably place SWNTs at desired locations and orientation at a high rate while allowing for fabrication of fully functional SWNT devices. The applications were mainly focused on nanotube electronics, particularly SWNT interconnects and field effective transistors.

The dissertation is organized in 5 chapters. Chapter 2 gives an introductory background on the techniques that are adopted for achieving the desired assembly. Chapter 3 discusses the use of micro/nano interdigitated finger design for assembly of SWNTs. A modified approach using PMMA trenches, which produces exceptional control over the assembly is discussed in chapter 4 along with device demonstration. A novel approach using dielectrophoresis to make room temperature 3D interconnects is presented in chapter 5.

2. Chapter 2: Background

This chapter gives detailed background information on the assembly techniques that were used in the current study to manipulate SWNTs. Before going into the assembly techniques, it is good to understand the forces that are important at Nano scale. Unlike Macroscale the dominant forces are much different at Nanoscale, for example forces like gravity that are important at macroscale are negligible at nanoscale. At nanoscale forces like Van der Waals, electrostatic and surface tension forces become important.

Interaction Distance	Predominant Force
Upto infinite range	Gravity
From a few nm upto 1 mm	Capillary Forces
> 0.3 nm	Coulumb (Electrostatic Force)
0.3 nm <separation distance < 100 nm	Lifshitz – Van der Waals
< 0.3 nm	Molecular Interactions
0.1 – 0.2 nm	Chemical Interactions

Table 2-1: Forces and their interaction distances[80]

2.1 Van der Waals Force

Van der Waals forces are short range forces that arise from temporarily induced dipoles between two neutral particles. A shift in the electron cloud of one molecule induces a shift in the neighboring molecule's electron cloud, leading to an attraction of the dipoles towards each other. The range over which these forces act are usually <10nm and can be described by using a Leonard-Jones Potential involving an attractive energy E_A and a repulsive energy E_R[81].

$$E_z = -E_A (z/z_o)^{-n} + E_R (z/z_o)^{-m} \quad (m > n), \qquad 2\text{-}1$$

$$F_{vdw} = -d\,E_z / dz \qquad 2\text{-}2$$

$$F_{vdw} = -(n\,E_A / z_o)(z/z_o)^{-(n+1)} + (mE_R / z_o)(z/\ z_o)^{-(m+1)} \qquad 2\text{-}3$$

The Van der Waals forces $F_{vdw} = 0$ when E_z is at a minimum (equilibrium) value with a surface gap distance z_o. When the two surfaces are pressed together with $z < z_o$ the force F_{vdw} is repulsive. And when the two forces are at distance $z > z_o$ the Van der Waals force is attractive, reaching a maximum value of $F_n = F_{vdw}$ (max) at which point the surface automatically detaches.

For two flat surfaces[82] at small distances $z < z_o$, the maximum attractive force per unit area is

$$F_{vdw}^{max} \approx A / 6\pi z_o^3 \qquad 2\text{-}4$$

Where A is the Hamaker constant. And at larger distances $z > z_o$ it becomes

$$F_{vdw} = A / 6\pi z^3 \qquad 2\text{-}5$$

For a cylinder with diameter d and length L interacting with a flat surface the Van der Waals forces can be calculated using the following expression[83]

$$F_{vdw} = \frac{A_{132} d^{1/2}}{16 z_0^{5/2}} L \qquad 2\text{-}6$$

Where A_{132} is the Hamaker constant between the particle and substrate in the presence of a medium and is given by

$$A_{132} = (\sqrt{A_{11}} - \sqrt{A_{33}})(\sqrt{A_{22}} - \sqrt{A_{33}}) \qquad 2\text{-}7$$

Where A_{11} is the Hamaker constant of the cylinder (in this case the nanotube), A_{22} is the Hamaker constant of the substrate and A_{33} is the Hamaker constant of the medium (air/water). The values of these constants are listed in table.

Material	Hamaker Constant (J)
Gold (Au)	40×10^{-20}
Carbon Nanotube[84, 85]	$\sim 50 \times 10^{-20}$
Water	4×10^{-20}
Air	~0
PMMA	7.1×10^{-20}

Table 2-2: Hamaker constant of different materials

2.2 Surface Tension Force due to Trapped Liquid

The property of the surface of a liquid to behave as an elastic sheet is called surface tension. It's the phenomenon that keeps things like blades or leaves afloat in liquid. The forces acting between molecules are cohesive forces. When there is a solid present, there is an additional attractive force, adhesive force. When a wetting fluid interacts with a surface it results in Capillary action. When the adhesive force is much stronger the cohesive forces between the water molecules it wets the surface. In case where there is a wetting agent present between the two surfaces. The capillary force can be derived from the Laplace pressure equation

$$\Delta p = \gamma\left(\frac{1}{r_1} + \frac{1}{r_2}\right) \qquad \text{2-8}$$

The force is then

$$F_{lap} = \gamma\left(\frac{1}{r_1} + \frac{1}{r_2}\right)A \qquad \text{2-9}$$

Where r1 and r2 are the curvature of the hyperbolic paraboloid produced by the meniscus about the sphere .In case where r1>> r2 the Laplace pressure equation reduces to

$$\Delta p = \frac{\gamma}{r_1} \qquad 2\text{-}10$$

Filling angle denotes the height of the water around the sphere. When the filling angle is significant (φ), such as in the case of an AFM tip the equation is a little more complicated[86] as the surface tension component of the force need to be included.

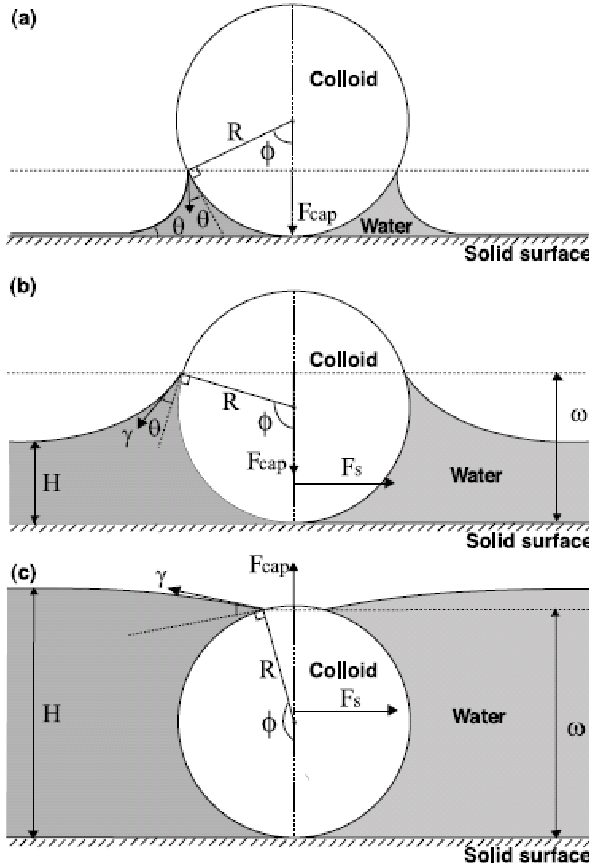

Figure 2.1: Capillary formation around a sphere

$$F_s = 2\pi\gamma R \sin\phi \sin(\theta + \phi) \qquad 2\text{-}11$$

The capillary force is then a combination of the surface tension force and the laplace force.

$$F_{cap} = F_{surf} + F_{lap} \qquad 2\text{-}12$$

$$F_{cap} = 2\pi R\gamma \sin\phi \sin(\theta + \phi) + \Delta p \pi R^2 \sin^2\phi \qquad 2\text{-}13$$

where Δp is the capillary pressure defined as the pressure jump across the air-water interface. Thus the capillary force can be can be approximated fllowing Dekker et. al. as

$$F_{cap} = \pi R\gamma\left[2\sin\phi\sin(\theta+\phi) + \cos\theta(1+\cos\phi)^2 - \sin\phi\right] \qquad 2\text{-}14$$

For the simple case of a sphere on a flat surface with vanishing filling angle, the capillary force can be written in terms of the sphere radius[87]

$$F_{cap} = 2\pi\gamma R(\cos\theta_1 + \cos\theta_2) \qquad 2\text{-}15$$

Where θ_i are the contact angles and R is the radius of the sphere.

For cases of a dewetting liquid on a surface, the filling angle is not important and an approximate equation for hydrophilic surfaces ($\cos\theta \sim 1$) was derived by

$$F = 2\pi\gamma R \qquad 2\text{-}16$$

This approximation doesn't hold for increasingly rough surface. If the distortion of the contact line due to presence of an object (eg. Nanotube) is considered, than the capillary force is given by[88]

$$F_\sigma = \frac{\pi\gamma\theta^2}{\log(L/D)}.x \qquad 2\text{-}17$$

Where,θ is liquid contact angle (in radians) , L is a macroscopic length , D is the width of the trench and x is the deformation of the wetting line.

2.3 Hydrodynamic Drag Force

When a body is place in a moving fluid, or when a body is moving through a fluid it experience a resisting force, called Drag. The drag force is usually divided into two components: frictional and pressure drag. Frictional drag arises from the friction between the fluid and the surface over which it flows. Pressure drag arises from the eddying motion that is setup in the fluid by the moving object. Both type of drags can be associated with the viscosity of the fluid. The difference is in the different flow phenomena. While frictional (viscous) drag is important where there is no separation of the fluid (related to surface area

exposed), pressure drag is important for separated flows (Related to the cross-sectional area of the object).

For typical external flows the most important parameter is the Reynolds number. Reynolds number is a dimensionless quantity that gives the ratio of inertial forces to the viscous forces, hence the importance of these two types of force for a given body condition. Reynolds number is given by

$$Re = \frac{\rho v D}{\mu} = \frac{vD}{\nu} \qquad 2\text{-}18$$

where:

- v is the mean fluid velocity in (SI units: m/s)
- Dis the diameter (m)
- M is the dynamic viscosity of the fluid (Pa·s or N·s/m²)
- ν is the kinematic viscosity ($\nu = \mu / \rho$) (m²/s)
- ρ is the density of the fluid (kg/m³)

The nature of the flow depends strongly on the Reynolds number.

High Reynolds number flow >>1)	Low Reynolds number flow (Re << 1)
Inertial forces dominate	Viscous forces dominate
Flow separation (e.g. vortex shedding)	No flow separation
May be turbulent	Always laminar
Not reversible	Reversible
Non-linear	Linear
Large momentum (vortices in wakes)	Small momentum (no vortices in wakes)
Coasting	No coasting

Table 2-3: Comparison of flow at different Reynolds number

Fluid flow is governed by two sets of equations, namely Navier Stokes and Continuity. The continuity equation in fluid mechanics is given by

$$\frac{\partial \rho}{\partial t} + \nabla.(\rho u) = 0 \qquad 2\text{-}19$$

And the Navier Stokes equation governing a fluid is given by

$$\rho\left(\frac{\partial v}{\partial t} + v.\nabla v\right) = -\nabla p + \nabla .T + f \qquad \text{2-20}$$

For a incompressible flow for Newtonian fluids, the Navier Stokes equation becomes

$$\rho\left(\frac{\partial v}{\partial t} + v.\nabla v\right) = -\nabla p + \mu\nabla^2 v + f \qquad \text{2-21}$$

And the continuity equation becomes

$$\nabla .u = 0 \qquad \text{2-22}$$

Stokes obtained a solution for this equation by completely neglecting the inertial forces on the flow due to a body. This is true for very low Reynolds number Re << 1.

Hence the continuity and the Navier Strokes becomes

$$\begin{aligned} \nabla\left(\frac{p - p_o}{\mu}\right) &= \nabla^2 u = -\nabla \times \omega, \\ \nabla .u &= 0, \end{aligned} \qquad \text{2-23}$$

Where p_o is the uniform pressure far from the body. Whose boundary conditions are given by

$u = U$ at the body surface

$u \to 0$ and $p - p_o \to 0$ as $|x| \to \infty$

The Stokes equation is valid only for very low Reynolds number and cant be extended to higher Reynolds numbers. The Stokes approximation is valid only at very close regions to the sphere, and at any point away from the sphere it is invalid. Hence Oseen modified the equation by including the inertial term. Oseens equation is given by

$$\begin{aligned} -\rho U.\nabla u &= -\nabla p + \mu\nabla^2 u \\ \nabla .u &= 0, \end{aligned} \qquad \text{2-24}$$

Where,

- u is the disturbance velocity induced by the moving object, *i.e.* the total flow velocity in the frame of reference moving with the object is –U+u,
- p is the pressure,
- ρ is the density of the fluid,
- μ is the dynamic viscosity,
- ∇ is the gradient operator, and
- ∇^2 is the Laplace operator.

The boundary conditions for Oseen flow around a rigid object is

u=U at the object surface,

$u \longrightarrow 0$ and $p \longrightarrow p_\infty$ for $r \longrightarrow \infty$

For flow over a cylinder, Lamb[89] obtained an approximate solution for the Oseen Equation.

$$D_L = 4\pi\mu U\varepsilon \qquad \text{2-25}$$

Where D_L is the Lamb drag per unit area, and

$$\varepsilon = \left[\frac{1}{2} - \gamma - \ln(\mathrm{Re}/\ \ 8)\right]^{-1} \qquad \text{2-26}$$

Where γ=0.577216.is Euler's constant and Re is the Reynolds number based on the cylinder diameter.

When we consider the case of fluid flow over a flat plate, the flow creates a thin boundary layer near the surface due to no-slip condition on the surface. The Navier Stokes equation can be directly solved to obtain the boundary layer equations. Since Re << 1, the flow is completely laminar. The governing equation for a laminar boundary layer is

$$\frac{\partial u}{\partial x}+\frac{\partial v}{\partial y}=0$$
$$u\frac{\partial u}{\partial x}+v\frac{\partial u}{\partial y}=\nu\frac{\partial^2 u}{\partial y^2} \qquad \text{2-27}$$

There is no known analytical solution for this problem, hence the solution has to obtained numerically (Blasius Solution). For a flat plate of length L and width W, the Blasius solution yields a coefficient of drag of ' $C_d = \frac{1.328}{\sqrt{R_e}}$

From which the drag force can be calculated using the following relation

$$F_d = C_d KA = C_d \times \frac{1}{2}\rho U_\infty^2 \times LW \qquad \text{2-28}$$

2.4 Electric Field Assisted Assembly

As mentioned earlier electric field at nanoscale is significant and can be used as a driving force to manipulate nanoscaled objects. Hence electric field assisted assembly has been quite widely used for assembly of nanoparticles and recently for assembling SWNTs as well. Electric field assisted assembly can be categorized into two main categories:

- Electrophoresis
- Dielectrophoresis

2.4.1 Electrophoresis

Electrophoresis[90] is a process in which charged particles or elements dispersed in a suspension migrate towards oppositely charged electrode under the influence of a uniform electric field. These particles coagulate on the surface of the electrode to form a dense mass. This combined process of migration and deposition under the influence of an external electric

field is termed electrophoretic deposition. EPD has been widely used for coating of conducting surfaces with micro or nanoscale components.

When an element is placed in an aqueous medium, it acquires a surface charge by ionization and/or by the adsorption of ions. A layer of counter ions called the stern layer is formed to balance the surface charge. An outer region called the diffuse electrical double layer where the ions are in constant thermal motion spans a distance on the order of the debye length. In the absence of any thermal motion, sufficient ions could be attracted to the surface of the particle neutralizing its charge. Under the influence of an electric field the ions and particles should move in opposite direction, but the electrical double layer moves along with the particles. This is because the potential at the surface of shear called the zeta-potential determines the electrode towards which the particles move and not the charge of the particle itself. In principle a particle with a negative surface charge can show a positive zeta potential.

The electrostatic force that drives this particles is a function of the electric field (E) and the charge (q) carried by the particle.

$$F_{elec} = Eq \qquad 2\text{-}29$$

The particle experiences an opposing force due to the viscous resistance of the medium and is a function of the velocity of the particle (v) and the coefficient of friction (f)

$$F_{fric} = v.f \qquad 2\text{-}30$$

In a constant and homogeneous electric field, the electric field is balanced by the frictional force.

Hence, $v = {qE}/{f}$ 2-31

For a spherical particle, the frictional coefficient is given by Stoke's law

$f = 6\pi\mu R$ *2-32*

R – Radius of the particle

μ - viscosity of the medium

Hence the velocity of the particle through the medium under an applied electric field can be calculated using the following relationship.

$v = qE/6\pi\mu R$ *2-33*

Although EPD is an old process, the mechanism is not completely understood.

2.4.1.1 Zeta Potential

All particles in a suspension exhibit a zeta potential or surface charge. Knowledge of a particle's zeta potential is important for the optimization of sample processing and is a simple method of quality control. As zeta potential can predict the stability of a formulation. If all the particles in the solution have a large negative or positive zeta potential then they will tend to repel each other and there is no tendency to flocculate. But if the particles have low zeta potential then there is no force to prevent the particles from coming together and flocculating.

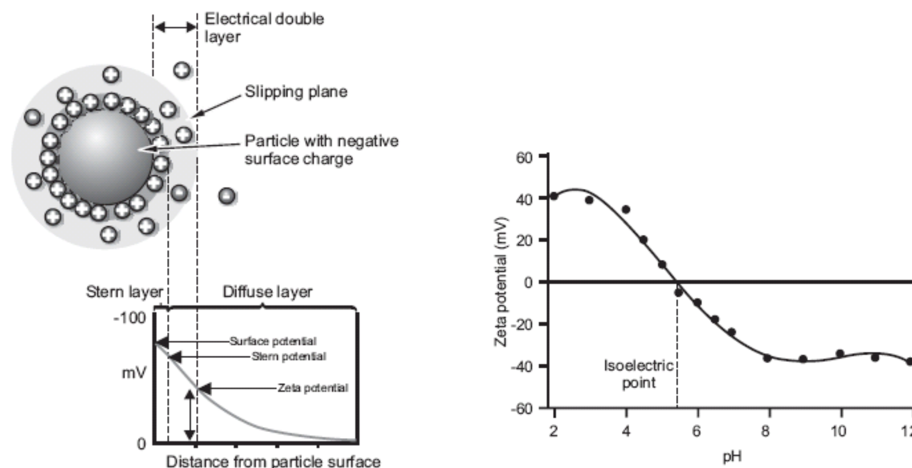

Figure 2.2: (left) Electrical double layer surrounding a particle (right)A typical zeta potential vs. pH curve.

Electric double layer is formed when the net charge developed at the particle surface affects the distribution of ions in the surrounding interfacial region, resulting in an increased concentration of counter ions. The liquid layer surrounding the particle consists of an inner region called the stern layer where the ions are strongly bounded and an outer, diffuse, region where they are less firmly attached. Within the diffuse there is a notional boundary inside which the ions and particles form a stable entity. When a particle moves, ions within the boundary move with it, but any ions beyond the boundary donot travel with the particle. This boundary is called the surface of hydrodynamic shear or slipping plane. And the potential that exists at this boundary is known as the zeta potential. Zeta potential in itself doesnt have any meaning. It has to be quoted with pH for the value to make sense. Say if a particle in the suspension has a negative zeta potential. Addition of alkali or acid would either increase or decrease the charge. Hence a zeta potential versus pH curve would give a more meaningful information. In cases where the zeta potential changes from being positive to negative or vice versa, the plot passes through a point called isoelectric point where the potential is zero.

2.4.1.2. Electrophoretic Deposition

EPD is a combination of two processes: electrophoresis and deposition. Electrophoresis pertains to the movement of charged particles in the solution under the influence of an electric field, whereas deposition is the coagulation of objects to a dense mass. During EPD, though the potential between the electrodes are maintained constant, a steeper potential gradient than that needed for electrophoresis is required for deposition[91]. As the particles assembled increases there is an increase in the electrical resistance. This decreases

the potential inducing electrophoresis and hence the motion of the objects. The amount of particles assembled for a constant voltage is given by the following relation[92].

$$\int dw = f \iint dS \mu_e E(t) C(t) dt \qquad 2\text{-}34$$

Where dS is an infinitesimal area of the depositing electrode where dw weight of particles that are deposited at in time dt from C(t) concentration of the particles in the suspension. E(t) is the voltage drop/ unit length of suspension normal to the depositing electrode and μ_e is the electrophoretic mobility of the particles in the suspension. f is an efficiency factor ($f \leq 1$, f = 1 when all the particles reaching the electrode take part in forming a deposit).

2.4.1.3. Electrophoresis of SWNTs

Since SWNTs used in this study are negatively charged due to the carboxylic acid groups present on their ends and to a smaller extent along the length of the tubes where defects may occur, a directional force (external electric field) can be utilized to drive the suspended SWNTs towards an electrode. EPD has been successfully used to assemble nanoparticles[93, 94,95] and recently SWNTs[96, 97,98] on conductive electrodes. Despite these drawbacks, the EPD process has the advantage of simplicity, scalability and short deposition time making it suitable for mass production.

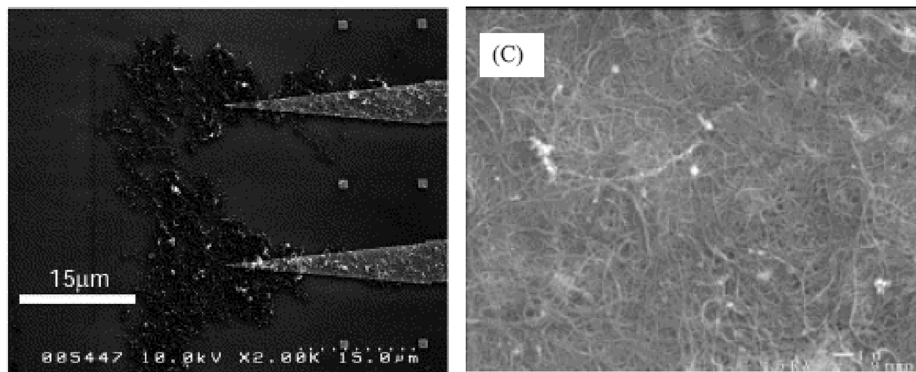

Figure 2.3: Electrophoretic assembly of SWNTs (A) on microstructured electrodes (B) on stainless steel sheets.

2.4.2 Dielectrophoresis

The dielectrophoretic phenomenon was first reported by Herbert Pohl in 1950[99, 100]. It is basically a phenomenon in which the motion of dielectric objects is induced by the polarization in a non homogeneous electric field. All particles charged or uncharged exhibit dielectrophoretic activity. As opposed to the electrophoresis where the direction of motion is dependant on the sign of the field, in dielectrophoresis the motion is dependant on the field strength. In a non-uniform field a neutral particle acquires, in effect, a negative charge on the side facing the positive electrode, and a positive charge on the side facing the negative electrode. Ideally the charge lying on each side should be equal, and the particle should be stationary. But depending upon the electrical properties of the medium and object, the object size and shape as well as the frequency of the electric field, the field strength varies causing the object to move in one direction or the other. When the permittivity of the object exceeds that of the suspension medium, the objects are attracted to regions of stronger electric field and are termed as positive DEP. And negative DEP if the objects are attracted to lesser electric field because of the permittivity of the medium being greater than that of the object.

The total electric force acting on a particle of net charge in a non-uniform field E is

$$F = qE + \delta E(r_+) - \delta E(r_-) = qE + (m\nabla)E \qquad \text{2-35}$$

Where V is the del vector operator, q is the charge on the particle of mass m and E is the applied electric field. For an uncharged particle (q = 0) and/or for frequency above 1 KHz, the electrophoretic effects are negligible, hence the term on the right-hand side of the equation will dominate.

Thus the time average DEP force for a spherical particle is

$$F_{DEP} = 2\pi\varepsilon_m R^3 \operatorname{Re}[K(\omega)]\nabla E_{rms}^2 \quad \text{2-36}$$

Where R is the radius of the particle, ε_m is the dielectric constant of the medium, ∇E_{rms}^2 is the gradient of the square of the RMS electric field, and $K(\omega)$ is the Clausius-Mossoti factor, the effective polarizability of the particle, which is related to the particle dielectric constant ε_p and medium dielectric medium ε_m by

$$K(\omega) = \frac{\varepsilon_p^* - \varepsilon_m^*}{\varepsilon_p^* + 2\varepsilon_m^*} \quad \text{2-37}$$

The Asterix here denotes that the dielectric constant is a complex quantity related to the conductivity σ and the angular frequency ω by

$$\varepsilon^* = \varepsilon - i\frac{\sigma}{\omega} \quad \text{2-38}$$

In the case of anisotropic objects such as nanotubes, the object would experience a torque tending to align the nanotubes along the electric field. Dielectrophoretic forces are particularly significant for nanotubes as they have been shown to control the alignment of SWNTs and have been widely explored for assembling SWNTs[101,102] on planar surfaces. The dielectrophoretic force acting on the nanotube strongly depends on the configuration of the electrode and can be calculated using the following expression.[103,104]

$$F_{dep} = \frac{\pi}{6} r^2 l \varepsilon_m \operatorname{Re}\{K(\omega)\}\nabla E_{rms}^2 \quad \text{2-39}$$

Where $K(\omega) = \left(\frac{\varepsilon_p^* - \varepsilon_m^*}{\varepsilon_m^*}\right)$, ε_p^* and ε_m^* are the complex permittivity of the rod-like particle and the suspending medium, respectively. Here $\varepsilon^* = \varepsilon - i(\sigma/\omega)$, where $i = \sqrt{-1}$, ε is the real permittivity and σ is the conductivity of the material. ε is a material property and can be

written as a product of the relative permittivity of the material and permittivity of free space ε_0. [19]:

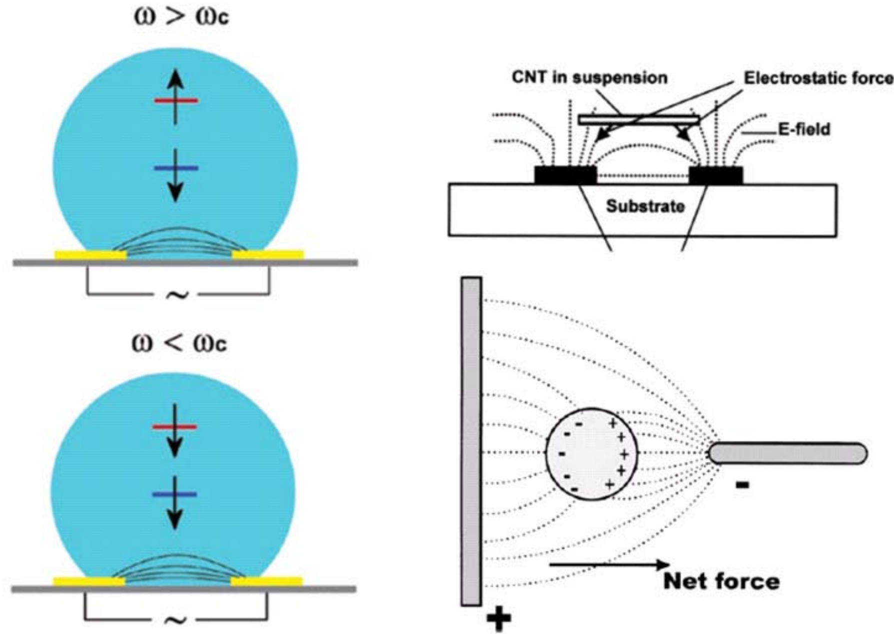

Figure 2.4: Mechanism of dielectrophresis

where ε_p and ε_m are the dielectric constants of the particles and the solvent medium, respectively and E_{rms} is the root mean square field strength. Controlled assembly of SWNTs by AC field was first demonstrated by Yamamoto et. al.[105]. They showed that the nanotubes move towards the electrodes for all frequencies of applied field from 10 Hz to 10 MHz. They also showed that at higher frequencies the degree of orientation of nanotubes in higher and the amount of impurities depositing decreases. Krupke et. al.[106] and Mureau et. al.[107] recently demonstrated that it is possible to selectively assemble m-SWNTs from a solution containing m-SWNTs and semiconducting single walled carbon nanotubes (s-SWNTs) using dielectrophoresis. Their method exploits the relative difference in dielectric constant between the two types of SWNTs with respect to the solvent. Utilizing a higher frequency

results in the movement of m-SWNTs and s-SWNTs in opposite directions along the electric field gradient, thereby selectively assembling only m-SWNTs on microelectrode arrays.

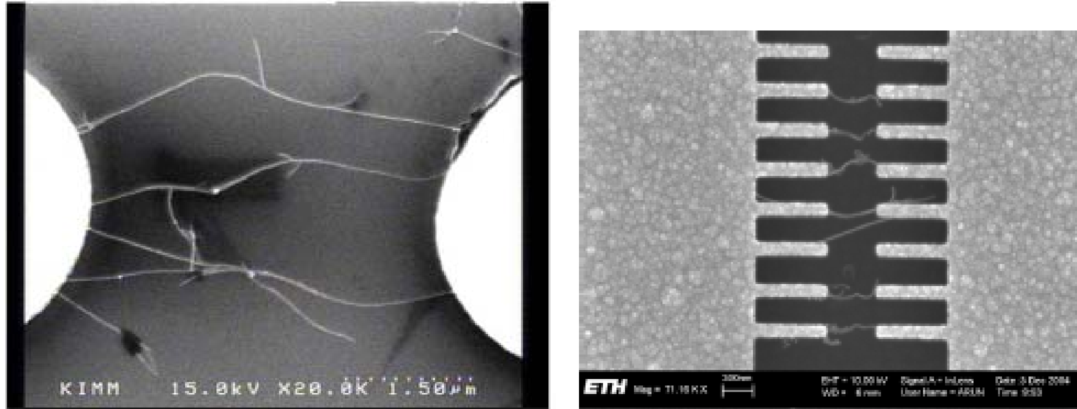

Figure 2.5: Dielectrophoretic assembly of SWNTs between electrodes[108].

2.2 Dip Coating

Dip coating has been the most widely used and oldest form of making thin films for a diverse range of applications including protective coatings, passivation layers, ferroelectrics, sensors and membranes. Dip coating involves withdrawal of the substrate vertically from the coating bath at a constant speed U_o. As the substrate moves, it entrains the liquid in a viscous boundary layer that splits in two at the free surface. Because of the constant evaporation and draining of the solvent, the entrained film aquires an approximate wedge shape that terminates in a well-defined drying line. The film acquires a steady shape and profile, when the upward moving flux is balanced by that due to evaporation. The particles inside the film are concentrated by evaporation, leading to aggregation and final drying to form a coating. At low withdrawal speeds the liquid viscosity h are low and according to a relationship derived by Landau and Levich the entrained thickness h_o balances the viscous drag ($\alpha\ \eta U_o/h$), gravitational force (ρgh), and liquid-vapor surface tension γ_{LV}.

$$h_o = \frac{0.94(\eta U_o)^{2/3}}{\gamma_{LV}^{1/6}(\rho g)^{1/2}} \qquad 2\text{-}40$$

Where, η is the viscosity of the fluid, U_o is the withdrawal velocity, ρ the density of the fluid and g is the acceleration due to gravity.

The particle assembly is stabilized by the surface charges, and follows the stern's potential consideration. The assembly can be explained according to the Stern's theory by the approaching of the charged particles to distances below the repulsion potential. Once the particle comes to distances below the repulsion potential, it changes to an attraction potential leading to assembly.

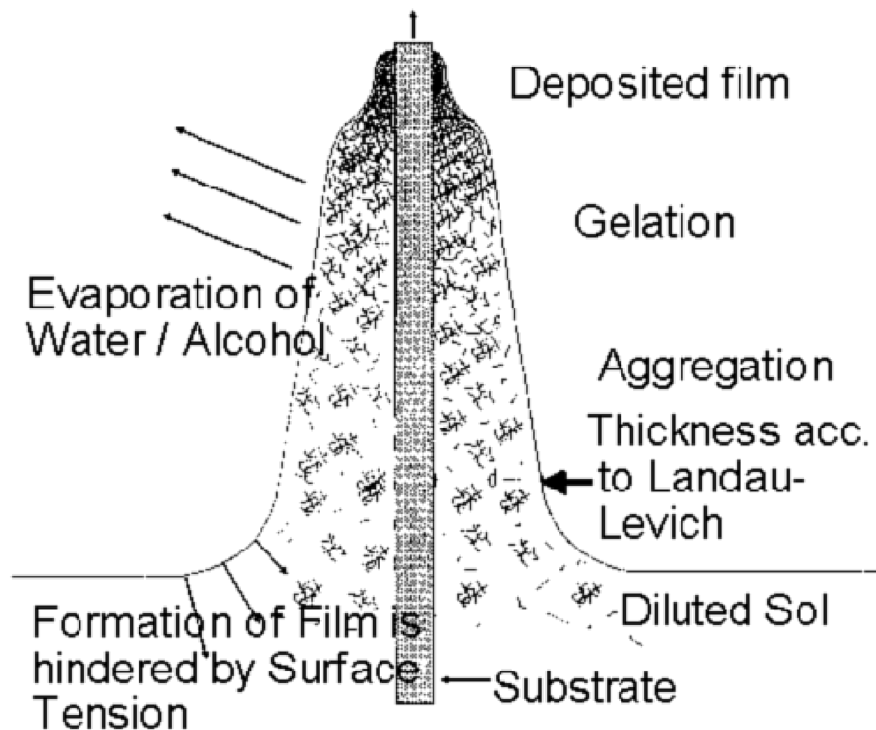

Figure 2.6: Schematic of the Sol-Gel dipcoating process[109] .

2.5 Fluidic Assembly

Fluidic alignment is a simple and elegant way of providing directionality to nanowires and nanotubes. This technique has recently drawn the attention of quite a few researchers. Liebers group was the first to report and use this technique to orient nanowires and make functional networks. Huang et. al.[110] combined fluidic alignment with surface patterning techniques to assemble nanowires into parallel arrays with controlled separation. Jin et. al.[111] exploited the fact that the separation between nanowires assembled by Langmuir- Blodgett technique has a defined average value to make large scale and parallel interconnection. The nanowires assemble onto the substrate are aligned at the air-water interface. Photolithography is then carried out to define the contact pads. Oh et. al.[112] and Ko et. al.[113] showed that by using alternate hydrophilic and hydrophobic surfaces it is possible to confine the drying of the liquid into microstructured patterns and hence the assembled nanotubes. While Ko et. al. placed the substrate at an angle and let the solution evaporate, Oh et. al. pulled the substrate out of the liquid at a constant rate. This technique is similar to dip coating, a widely used industrial applications for thin-film deposition on planar and cylindrical surfaces due its simplicity and high throughput. Dip coating method involves immersion of a wettable substrate into a solution containing the material to be coated, followed by a gradual withdrawal of the substrate from the solution at constant velocity. The wetting properties of the surface can be tailored with submicron resolution by using techniques like photolithography or micro-contact printing. Majority of work on dip-coating has been done on chemically homogeneous surfaces. Lately there has been interest for selectively coating micro- nano structures using this technique. Biebuyck et. al.[114] used this technique to fabricate microlens on chemically patterned substrates. Qin et. al.[115] used this method to

coat metallic micro-crystals from aqueous solution. Because of capillary and surface tension forces at the air-water interface, dip coating when used for two dimension structures like nanowires[116], nanotubes[117] and DNA[118] orients the long axis of these structures in the direction of the withdrawal of the substrate.

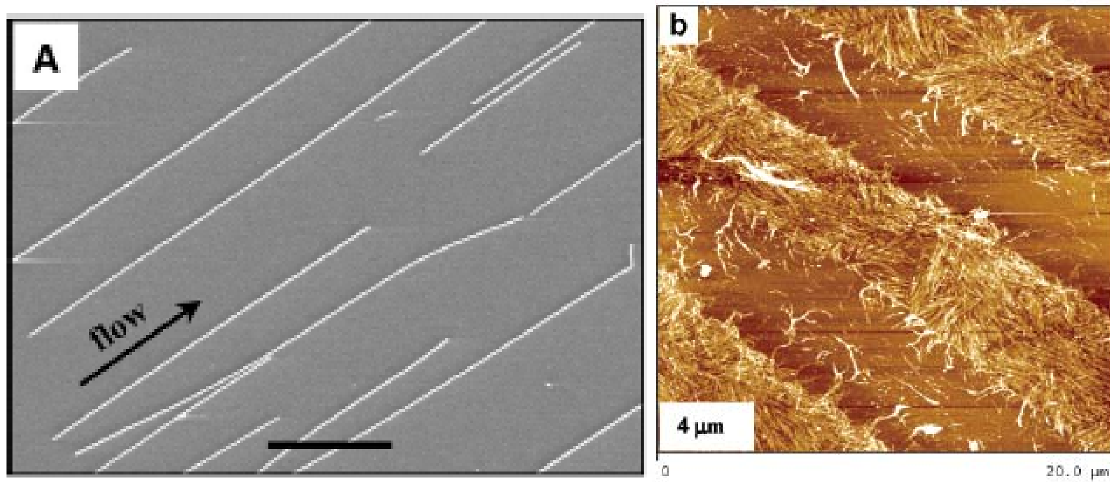

Figure 2.7: (A) Parallel array of NW assembly (B) SWNT assembly by Dip Coating.

3 Chapter 3: Assembly on Interdigitated Finger Electrodes

3.4 Introduction

The micro-electrode configuration is the most simple and straight forward approach to assemble micro/nano scale elements. It has been successfully adopted for the DC assembly of both micro and nano particles[119,120,121] and SWNTs. With a lack of proper techniques to measure the charge on these SWNTs, an interdigitated electrode configuration would aid in studying the behavior of SWNTs in the solution. Xiong[122] did an indepth study on the assembly of micro and nano particles on the interdigitated electrode configuration. Wakaya et. al.[123] and Kumar et. al.[1240] were the first to show that it is possible to assemble CNTs on micro-fabricated metal electrodes using EPD. The importance of using an interdigitated electrode configuration was demonstrated by Wakaya et. al.[125] when they used it to show that the electrodes on which CNTs deposit during EPD vary with the type of electrolytic solution used and the source of the CNTs. But none of these assemblies reported any directional control on the assembled SWNTs.

In this section we discuss the fabrication of micro and nanoscale electrodes for the assembly of SWNTs. The electrodes are fabricated using gold on SiO_2 substrates by standard lithographic techniques. DC electrophoresis is used to assemble the SWNTs. Parameters such as voltage and time are optimized to obtain good coverage of SWNTs. We study the behavior of the SWNTs at different pHs for a given voltage. Nanoscale electrodes are fabricated in order to obtain directional control on the SWNTs. Scanning electron microscopy images are used to discuss the experimental results. Problems with the assembly of SWNTs on

nanoscaled electrodes are discussed with the aid of both electrical measurements and simulation results in addition to actual experimental data.

3.5 Experimental Procedure

3.5.1 Fabrication of Microelectrodes

Interdigitated microelectrodes were fabricated using standard photolithography technique.

- A 500 nm thick SiO_2 was grown thermally on top of a Si substrate.
- Cr/Au (5nm/250nm) was then sputter deposited on top of the SiO_2 using Material Research Corporation's DC magnetron sputter deposition system. The Cr layer was used as an adhesion layer between Au and SiO_2.
- A thick photoresist PR 1818 was spun on top of the wafer on the brewer 100 CB photoresist baker and spinner at 4000 rpm for 60 seconds. Followed by a soft bake at 115 C for 60 seconds.
- The photoresist was patterned using a Quintel 4000-6 mask aligner.
- The PR was then developed using Microchem corporation MF 319 developer for 60 seconds.
- Dry etching of the Au/Cr layer was carried out through the exposed PR using Vecco Microetch Ion Mill for 11 minutes at 0° angle.
- The remaining photoresist was stripped using Microchem corporation's 1165 at 100 ºC for ½ hour. Followed by DI water rinse for 5 minutes.

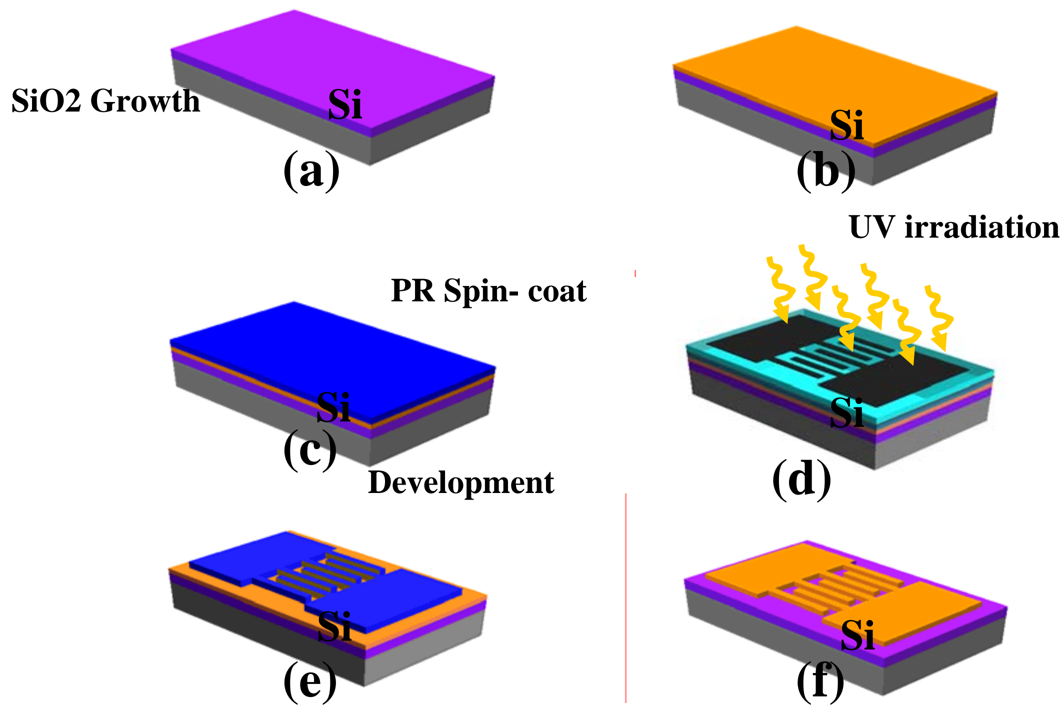

Figure 3.1: Fabrication Process flow for making interdigitated microelectodes

3.5.2 Fabrication of Nanoelectrodes

Interdigitated microelectrodes and nanoelectrodes were fabricated using a combination of standard photolithography technique and electron beam lithography respectively.

- Au/Cr microelectrodes were fabricated on thermally grown SiO_2 as mentioned in earlier section.
- Spin 150 nm thick electron beam resist (1:1 Nano 950 PMMA: Anisole) over the microfabricated Au electrode. Followed by soft baking at 180 ºC for 90 seconds.
- Expose the PMMA using FESEM.
- Develop the exposed PMMA first using 1:3 MIBK:IPA for 70 seconds and then in IPA for 20 seconds. Followed by DI water rinse for 5 minutes.

- Deposit Cr/Au (3 nm /50 nm) using Material Research Corporation's DC magnetron sputter deposition system.
- Carry out a liftoff process by placing the chip in acetone for 24- 48 hours.
- Rinse in DI water for 5 minutes to get rid off all residual acetone.

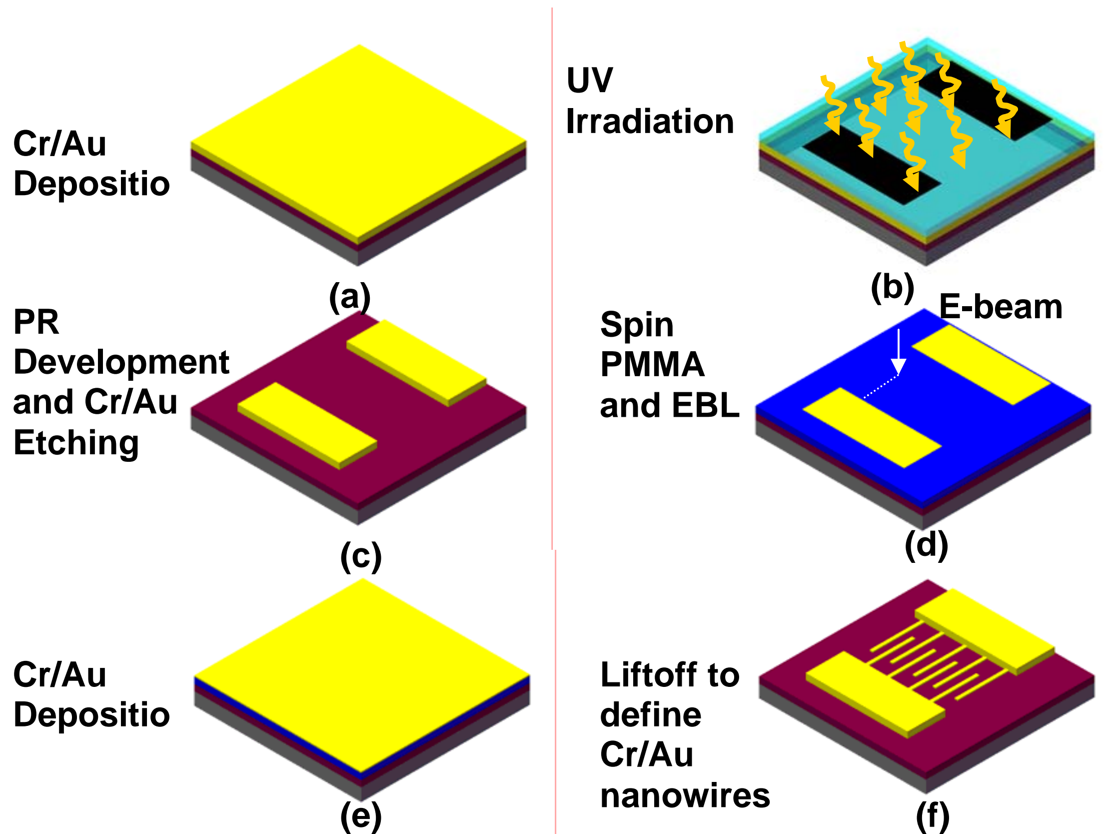

Figure 3.2: Fabrication Process flow for making interdigitated nanoelectrodes

3.5.3 Preparation of CNT suspension

Carbon nanotubes used in this experiment are mostly SWNT synthesized by high pressure carbon monoxide (HiPco). The SWNTs obtained were purified and dispersed in neutral water based solution at Nantero. The actual process of dispersion is protected by Nantero's IP[126].

The dispersed nantero solution was further diluted in DI water and either ammonia or sulphuric acid was added to adjust the pH. The addition of the base or acid was also to induce

ions in the solution. The concentration of the solution was then varied to obtain the desired results.

3.5.4 Procedure

The experiments were carried out using two different approaches. The first setup consisted of mounting a 15 x 15 mm chip with the micro/nano electrodes on a probe station. This setup is shown in figure 3.3. Initial experiments involved placing a probe on each of the pads and biasing them oppositely. A droplet of nanotubes was placed on the electrodes and a bias was applied across the electrodes. This resulted in assembly of nanotubes only on the positive electrode. Further experiments and modeling revealed that having an additional electrode at a distance in the solution help the nanotubes to move towards the microelectrodes. So the setup was modified to have an additional probe placed on the top edge of the droplet. This modification increased the density and coverage of nanotubes. Eventhough this technique provides a good coverage of SWNTs on the electrodes; it is very sensitive to the type of drying method used. Some of the drying methods adopted included blow drying with N_2 at different psi, air dry and suction using a syringe. It was found that a low pressure N_2 dry was the best option. While the suction method removed all the assembled SWNTs, the air dry method tends to pull the nanotubes towards the air –water interface leaving a coffee stain appearance[127]. The N_2 blow dry method was the most reliable of the three methods adopted but still remained highly dependant on the direction and the pressure.

Hence an alternative configuration was used wherein the pads of the microelectrodes were connected to the positive terminal and immersed in a solution of SWNTs along with a

negative counter electrode. Following assembly the chip was removed from the solution by hand with the voltage still on. This configuration gave a much better and repeatable assembly.

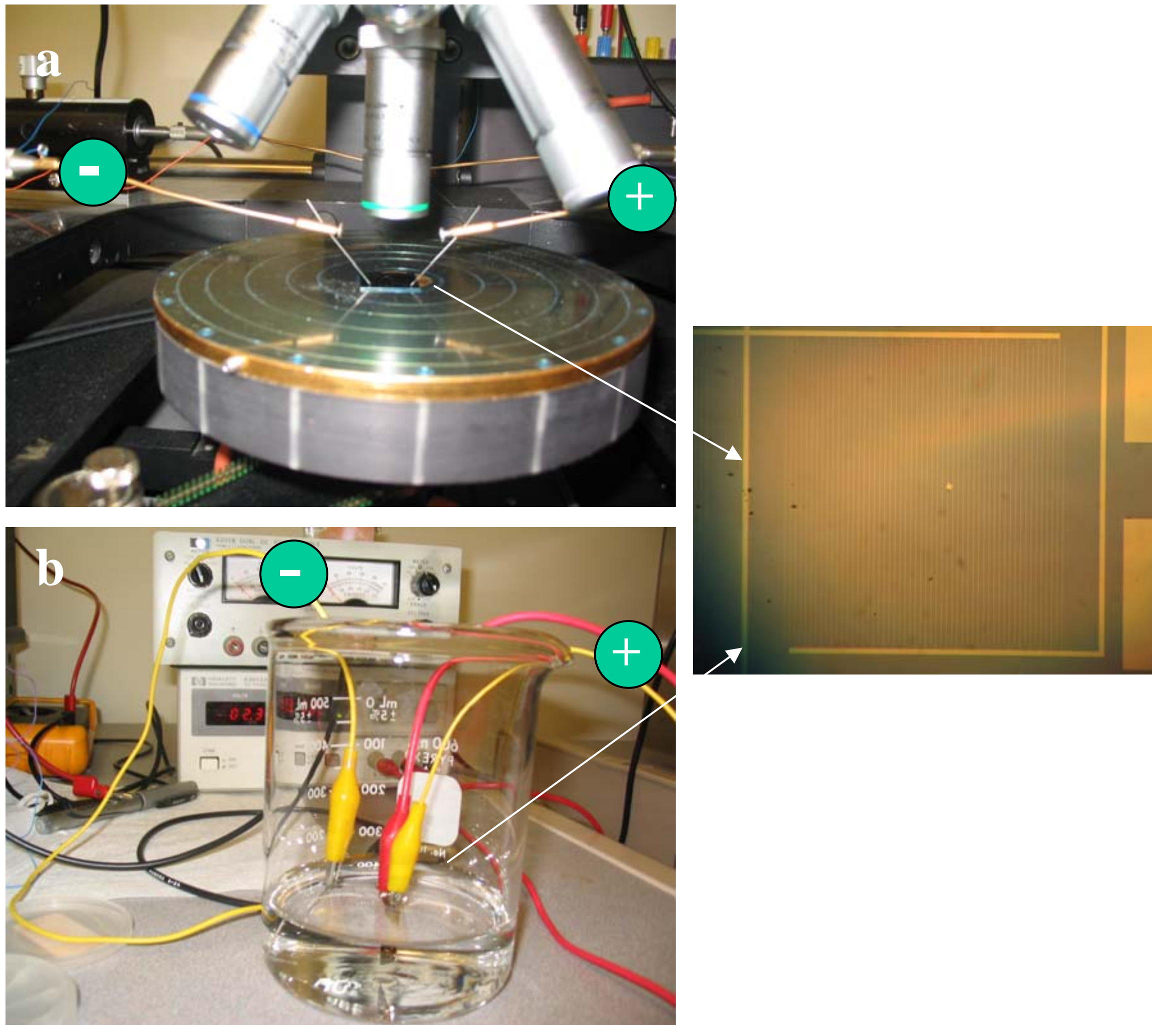

Figure 3.3: Two different approaches to assemble SWNTs on microelectrodes (a) Using a probe station (b) Using Aligator clips and a third electrode to drive the SWNTs in the solution towards the electrode

3.6 Results and Discussion

3.6.1 Microelectrode

Under bias most of the SWNTs were deposited on the positive electrodes. This assembly behavior was consistent over the entire pH range from 4 to 12. When diluted in

alcohol solution instead of DI water, they show similar behavior and assemble on the positive electrode. This is due to the fact that the charge on the nanotubes is due to the presence of carboxylic acid groups, and when they are dispersed in water or solvent becomes COO^- giving a negative charge to the SWNTs. This technique also allows us to evaluate the behavior of the SWNT deposition at different pH's. As direct measurement of the zeta potential is hampered due to the reasons explained in appendix. Since SWNTs assemble on the positive electrode for all values of pH, it can be deduced that the nanotubes posses a negative zeta potential through the entire range of pH from 4 to 12, consistent with the measurements made by Dai et. al.

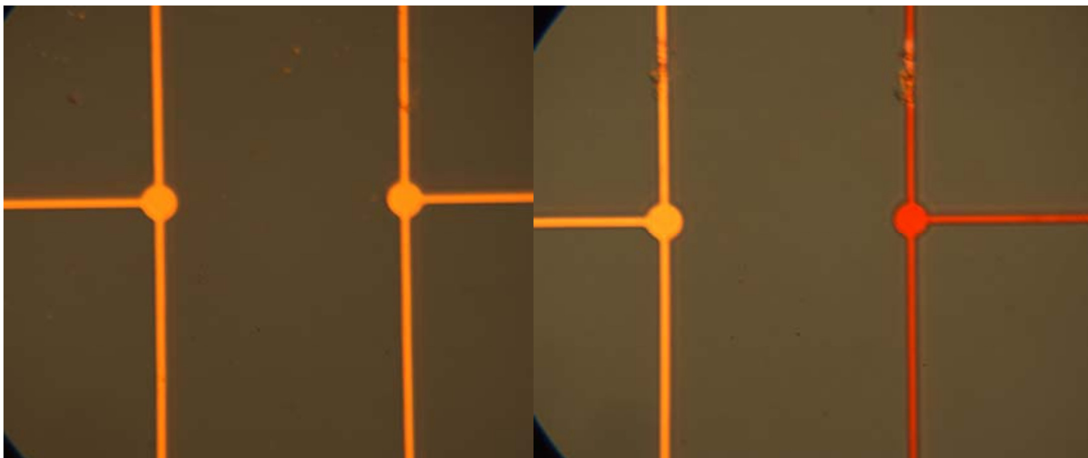

Figure 3.4: Optical Image showing microelectrodes (left) before assembly (right) after assembly.

The assembly was first characterized by optical microscope. Figure 3.4 shows optical image of the microelectrodes before and after assembly. It can be seen that the positive electrodes become darker due to the deposition of SWNTs. At pH close to neutral the nanotube assembly seems to be more stable as opposed to the assembly at higher or lower pHs. At pH values above 10 the SWNT seemed to collapse and form bundles. Moreover when using higher pH's a film was deposited along with the nanotubes on the gold electrode.

SWNT deposition from alcohol suspension was not very selective and some SWNTs can be found on the SiO_2 surface. It was also seen that the SWNTs tend to agglomerate more in IPA suspension. At higher voltages the Au electrodes were pitted due to electrochemical reactions. At neutral pH, there was no assembly of SWNTs. This indicates that the ions in the solution help in mobilizing the SWNTs when an electric field is applied. When a salt (Sodium di bromine fluoride) was used the SWNT assembly was inconsistent along the length of the electrode with some of the nanotubes assembling on the SiO_2 substrate. The density of the assembled SWNTs increased with increase in voltage and concentration as expected.

Eventhough the SWNTs can be accurately assembled on only positive electrodes; there is no control over the orientation of these nanotubes. By making the electrodes at nanoscale, much smaller than the total length of the tube, it was expected that these nanotubes would align along the direction of the nanofinger.

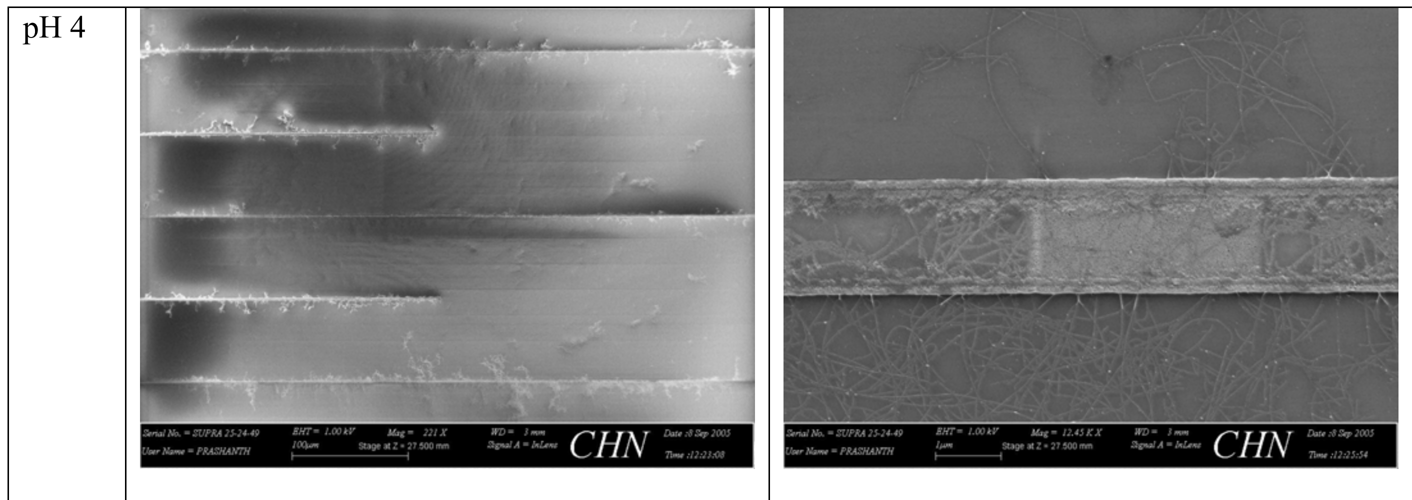

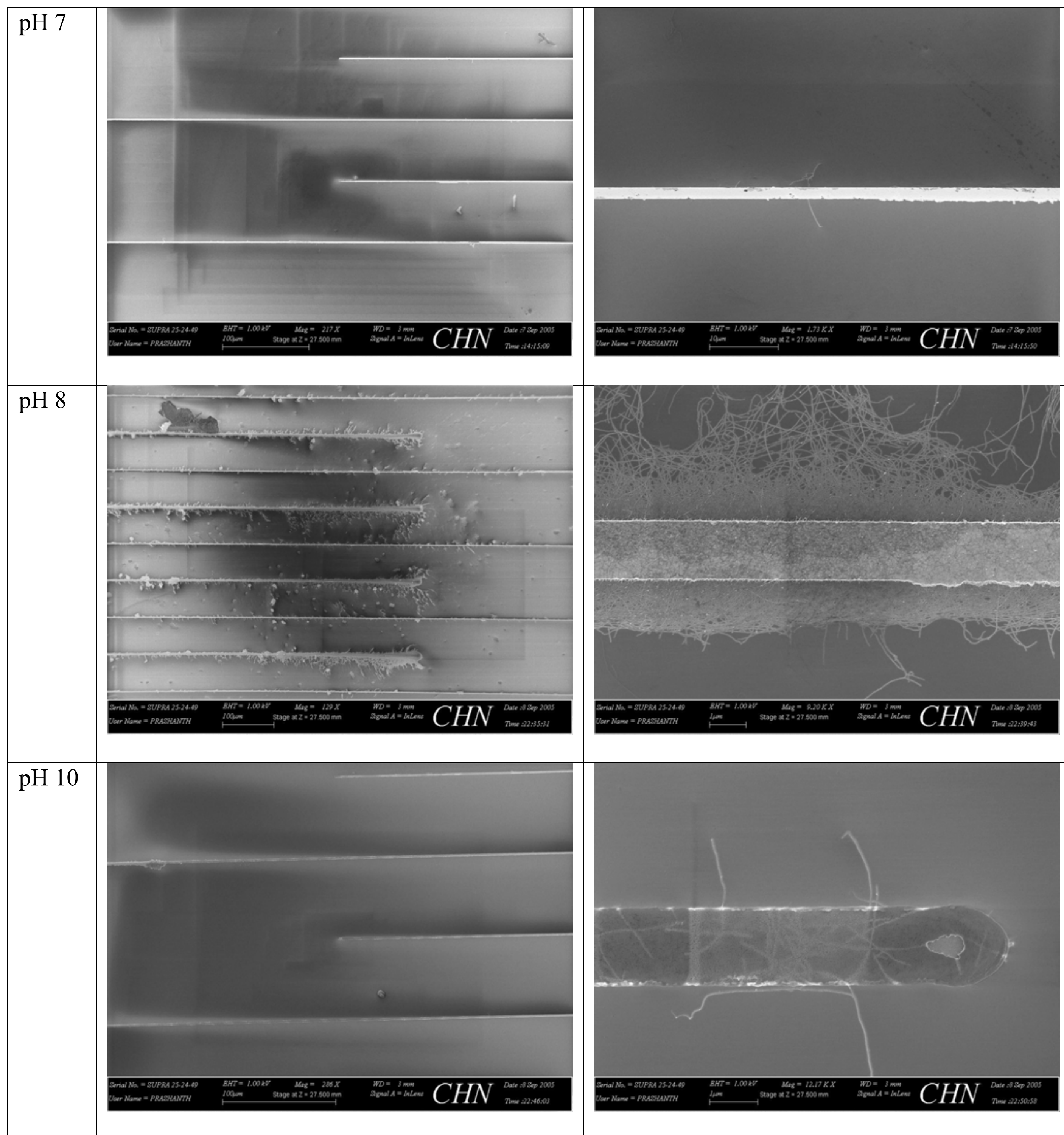

Figure 3.5: Table showing the Assembly of SWNTs on microelectrodes at different pH values

3.6.2 Nanoelectrodes

Hence interdigitated nanofingered electrodes were patterned and fabricated using EBL and a liftoff technique as mentioned in section 3.5. The liftoff technique has some drawbacks. During the time of the fabrication of these nanofingers, the facility didn't have an ebeam evaporator. Hence all metal depositions were carried out using the MRC sputtering tool. The sputtering system produces a conformal coating of metal as opposed to the evaporator that provides directed deposition of metal. This affected the liftoff process providing a very low yield. It is usually advisable to leave the sample in the acetone solution for 24 to 48 hours, followed by a gentle ultrasound for 10 seconds to remove the excessive metal. Additionally before leaving in the solution it is a good idea to scratch the metal at strategic points to break the film. These techniques helped in getting a better yield, but still the yield was very low as compared to the microelectrodes.

Under bias as expected the SWNTs still moved to the positive electrodes. But most of the SWNTs assembled on the micron sized electrodes connected to the nanofingers. The nanofinger electrodes had no SWNTs assembled on them except for one or two stray SWNTs. A previous model[128] developed to understand this behavior showed that only nanotubes that are present in a region very close to the nanoelectrodes assemble on them, while the rest assembled on the microelectrodes. The assembly on nanoelectrodes amounts to less than 1% of the total concentration. Hence the microelectrodes have to be placed far away from the nanoelectrodes to have any kind of affect on the assembly.

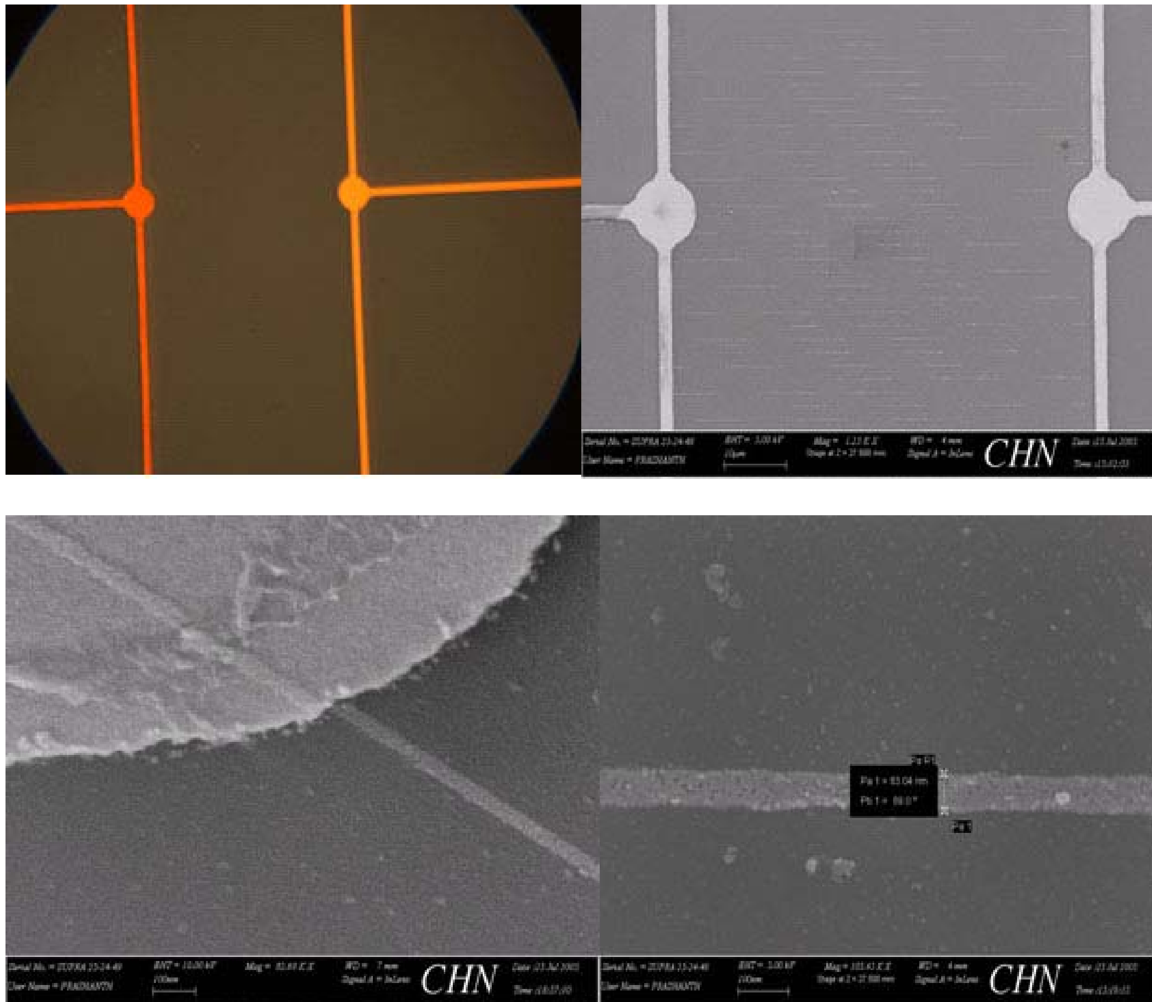

Figure 3.6: (a) Optical Image showing the nanofinger configuration (b) corresponding SEM image of the nanofingers (c) SEM image showing the overlap of the nanofinger over a microelectrode (d) A high resolution image of the nanofinger after liftoff.

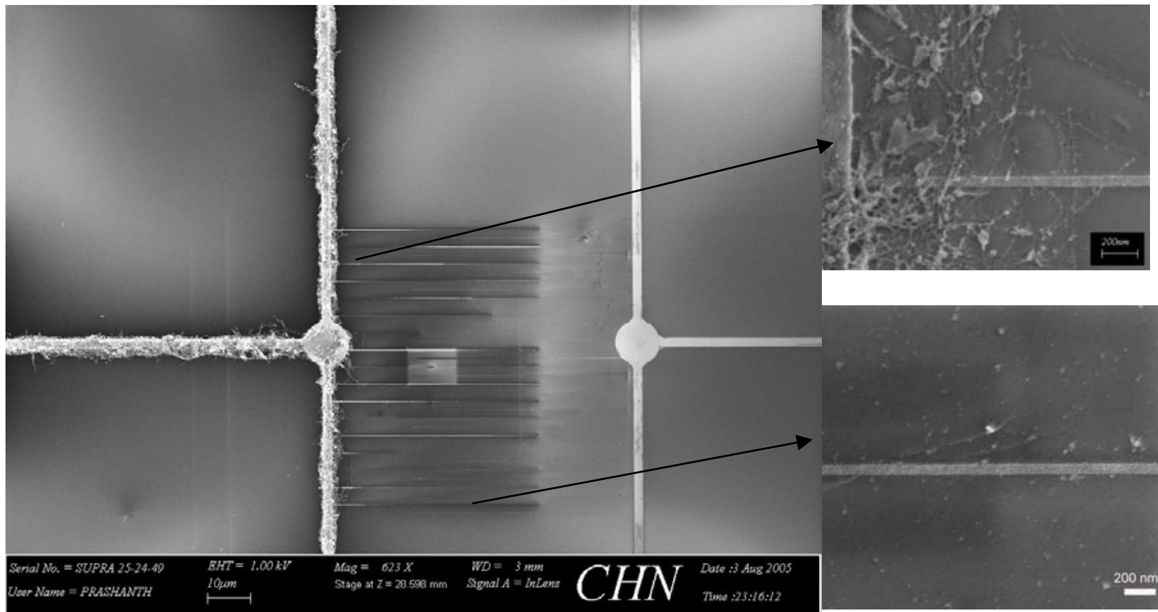

Figure 3.7: (a) SEM image showing the assembly of SWNTs on the positive electrode (b) A close up of the positive electrode in (a) showing that the SWNTs assemble only on the microelectrodes (c) a closeup of the nanofingers showing no assembly of SWNTs.

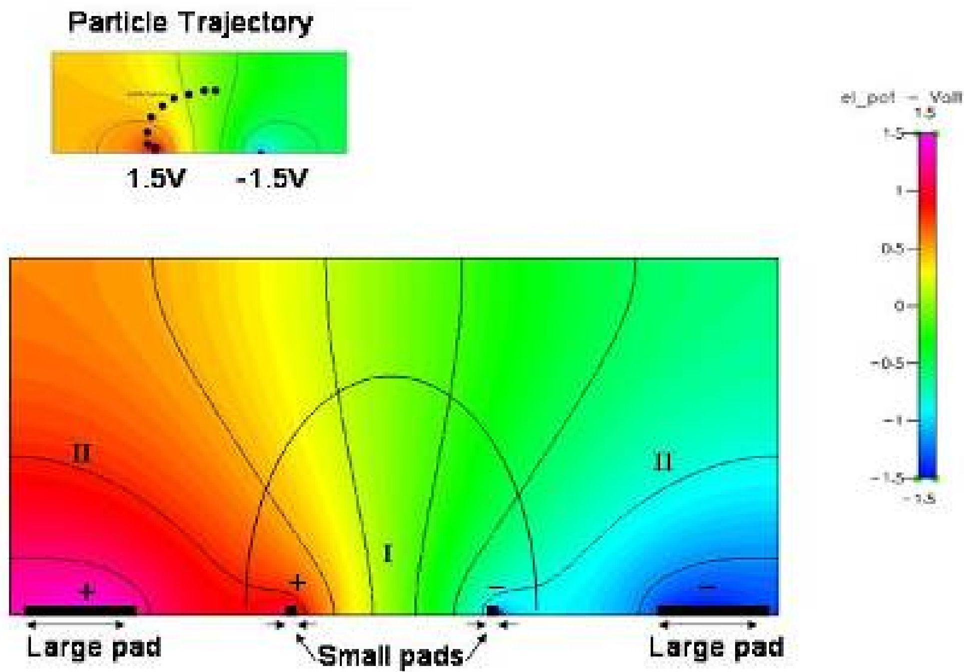

Figure 3.8: Computational fluid dynamics simulation showing the trajectory of the particles in the solution under an applied field.

Unfortunately due to design and fabrication considerations, it is not possible to place the nanoelectrodes away from the microelectrodes. Furthermore resistance measurements carried out on the nanoelectrodes using a Zyvex nanomanipulator revealed that the resistance of the nanoelectrodes is very high compared to the microelectrodes or bulk gold. For the measurement the nanoelectrodes were fabricated in the same manor as mentioned in section 3.5 except for the fact that wires ran from one end of the microelectrodes to the other as shown in figure 3.9. The resistance of 7 nanoelectrodes in parallel was measured to be around 2687.3 Ω. The dimensions of the nanoelectrodes fabricated were 35 μm in length, 180 nm wide and 40 nm tall. This yields a resistance of 18811.1 Ω per nanoelectrode. A resistivity of 386.9712 x 10^{-8} Ω-m which is 2 orders of magnitude higher than the measured value of Cr/Au with a thickness of 40 nm (4.7 x 10^{-8} Ω-m). The bulk resistivity of Au is 2.4 x 10^{-8} Ω-m. Due to this high resistance, the electric field is very low, and hence not sufficient enough to pull the SWNTs towards the wires.

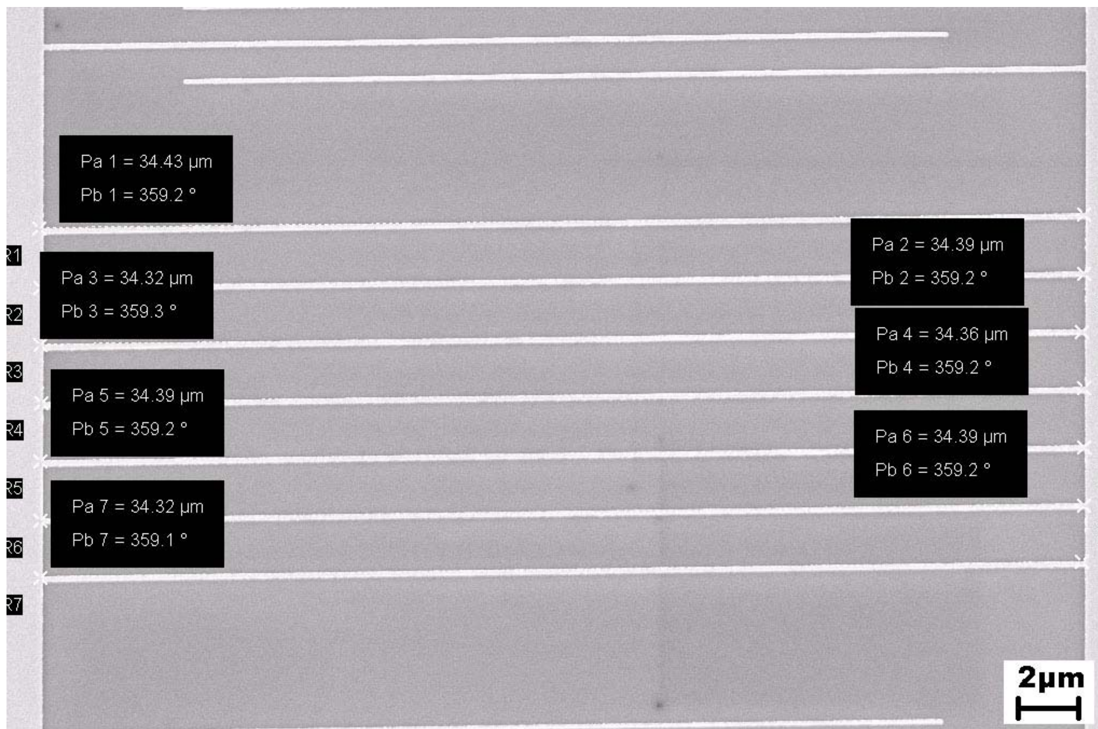

Figure 3.9: SEM micrograph of nanofingers fabricated for resistance measurements

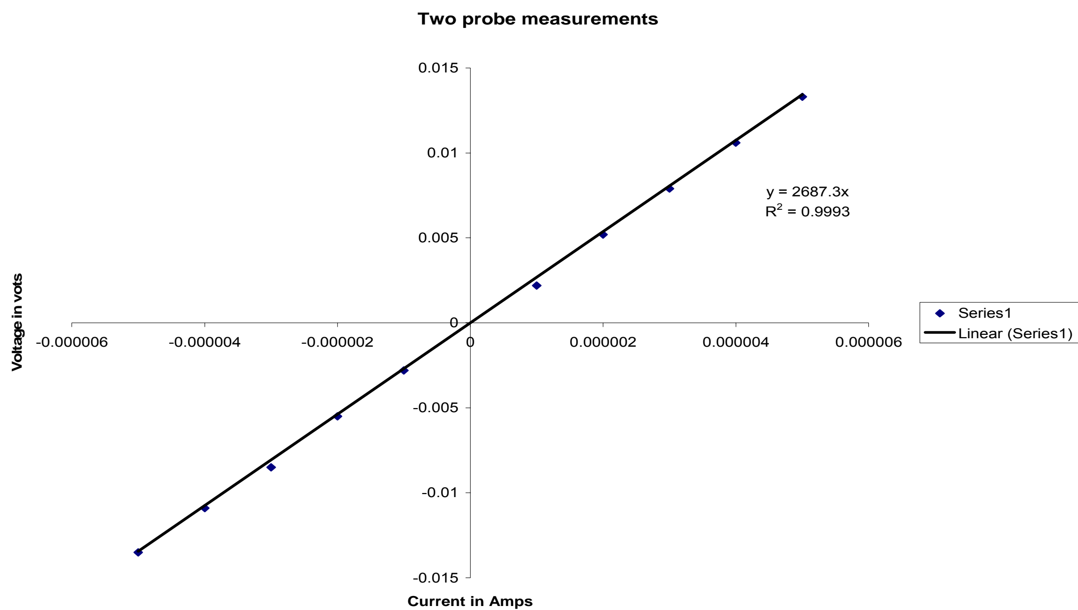

Figure 3.10: V-I characteristics of the fabricated nanofingers

This particular configuration, in addition to its inability to provide proper orientation of nanotubes had issues involving electrochemical degradation of the Au. The exact mechanism of the process of degradation was beyond the scope of the research. But some of the damages caused by electrochemical reaction while using high voltage and/or pH is shown in fig 3.11.

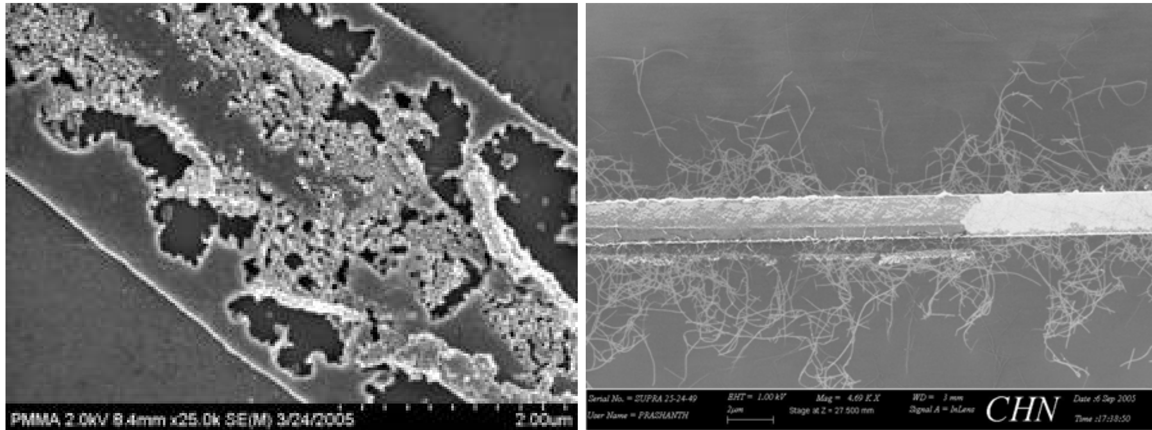

Figure 3.11: SEM micrograph showing damage caused to the gold electrode due to electrochemical reaction

3.7 Summary

Microelectrodes were fabricated using standard lithographic techniques on SiO_2 substrates. Under the influence of a DC electric field the SWNTs assembled on the positive electrodes. This was the case for the all pH's, indicating the SWNTs were negatively charged in aqueous solution. The assembly voltage and time was varied. The optimum condition was found out to be 3V for 1 minute at a solution pH of 8. There was no control over the orientation of the assembled SWNTs on the microelectrodes.

In order to obtain directional control over the assembled SWNTs, nanoscaled electrodes were fabricated using electron beam lithography and a liftoff process. In the first configuration under electric field all the SWNTs assembled on the microelectrodes with no assembly on the nanoelectrodes. A fluid dynamic simulation revealed that the electric field

generated by the large microsized pads was much higher in magnitude than the electric field generated by the nanoelectrodes. Electrical measurements of the nanoelectrodes showed that the resistance of the nanoscaled gold wires was two orders of magnitude higher than that of bulk gold. Hence a very high potential is required to obtain enough field strength to attract the SWNTs.

Expriments using potentials higher than 5 V showed that the micro and nanoelectrodes get damaged by electrochemical reactions due to hydrolysis of water. This major drawback prompted the evaluation of alternate approaches to assemble these SWNTs.

4 Chapter 4: Assembly in PMMA Trench Templates

4.4 Introduction

The assembly technique using micro/nanofinger patterns, although provides good assembly there are some problems associated with it, including no control over the orientation of the nanotubes, no assembly on nanoscaled nanofingers and degradation of the electrode when using higher potential. Hence there is a need for developing a new assembly technique that would overcome these difficulties. In this chapter we introduce a new assembly technique using trenches made in PMMA as the template. The assembly technique makes use of a combination of electrophoresis and fluidic assembly. Even though controlled assembly of SWNT has been achieved previously using a polymer trench template, further chemical modifications of the SWNTs[129] and/or the substrate[130] are necessary for orienting these SWNTs in a predetermined direction. Dip coating, a time consuming process, involves immersion of a substrate into a solution containing the material to be coated, followed by gradual withdrawal of the substrate from the solution. While dip coating method alone has been employed to assemble and orient DNA[131] and carbon nanotubes, patterned chemical functionalization of the substrate[132] is required for controlled assembly of nanotubes and the process is very slow.

The level of control provided by this combination of electrophoretic deposition and dip coating processes enables us to construct highly organized and aligned SWNT architectures down to 80 nm. Therefore produced SWNT networks can be directly used as SWNT based interconnect[133,134], diverse sensing elements[135,136], and other active components[137,138] in nanoelectronic devices. Towards this end, we fabricate SWNT based interconnects and field

effect transistors to demonstrate the viability of using this technique for large scale device fabrication. This approach is compatible with current complementary metal oxide semiconductor (CMOS) process and can be easily tuned towards high rate and high volume process.

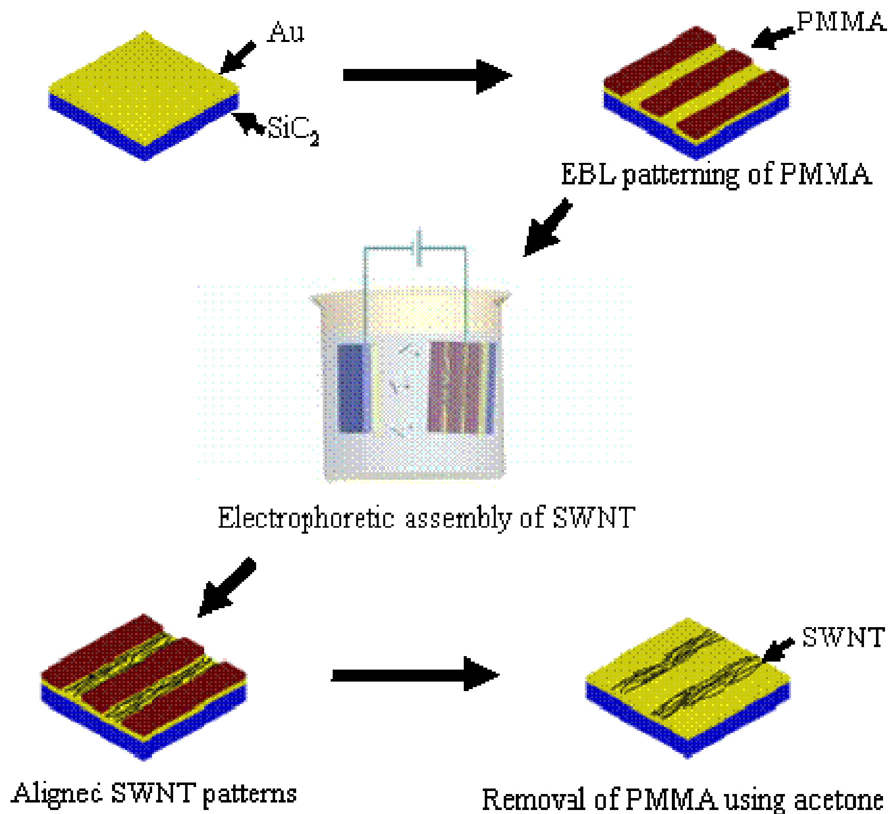

Figure 4.1: SEM image showing assembly of SWNTs on PMMA while using alcohol as the medium

4.1. Experimental Procedure

4.4.1 Preparation of the PMMA Trenches

Interdigitated microelectrodes were fabricated using standard photolithography technique.

- A 500 nm thick SiO_2 was grown thermally on top of a Si substrate.

- Cr/Au (5nm/100nm) was then sputter deposited on top of the SiO_2 using Material Research Corporation's DC magnetron sputter deposition system. The Cr layer was used as an adhesion layer between Au and SiO_2.
- An optical photoresist PR 1805 was spun on top of the wafer on the brewer 100 CB photoresist baker and spinner at 4000 rpm for 60 seconds to protect the chips from contamination during the dicing process. Followed by a soft bake at 115 C for 60 seconds.
- The wafer was diced into 15 mm x 15 mm chips.
- The photoresist was stripped in either 1165 for 10 minutes at 80 ºC or in piranha (1:2 H_2O_2 : H_2SO_4) at 115 ºC. Followed by DI water rinse for 5 minutes.
- 150 nm thick electron beam resist (1:1 Nano 950 PMMA: Anisole)was spun over the microfabricated Au electrode. Followed by soft baking at 180 ºC for 90 seconds.
- The desired areas were exposed on the PMMA using a FESEM.
- The exposed PMMA was first developed using 1:3 MIBK:IPA for 70 seconds and then in IPA for 20 seconds. Followed by DI water rinse for 5 minutes.
- The patterns are ready for electrophoretic assembly experiments.
- After assembly strip the PMMA using acetone for 10 minutes. Followed by 5 minute DI water rinse.

4.4.2 Procedure

A schematic diagram of the assembly technique is depicted in Figure 4.1. Electron beam lithography is employed to write nanoscale patterns directly onto a positive tone Poly-methyl methacrylate (PMMA) resist spun on a gold substrate. After exposure the substrate is developed using 1:3 methyl isobutyl ketone: isopropyl alcohol (IPA) mixture for 70 seconds,

followed an IPA rinse for 20 seconds. This results in the formation of nanoscale patterned trenches in the PMMA film exposing parts of the gold surface. The pre-patterned trench arrays are on a 2.25 cm^2 silicon chip, with each array covering an area of 10000 μm^2. Each array is composed of several parallel trenches of various widths and pitches defined by E-beam lithography. This patterned substrate along with a reference gold electrode is immersed into a solution (pH 8) containing dispersed SWNTs. A constant voltage is then applied for 60 seconds between the substrate and the reference electrode with the substrate being the positive electrode. The substrate is withdrawn from the solution at a rate of 50mm/min, with the potential still applied. After the substrate is drawn out of the solution the PMMA is removed using acetone.

4.5 Results and Discussion

Under bias the negatively charged SWNTs migrate towards the positive gold substrate and assemble only on the exposed gold surface. Following the assembly process the PMMA is dissolved using acetone, leaving the SWNTs assembled on the gold surface. Initial experiments conducted with this technique, involved the withdrawal of the substrates from the liquid by hand. An NTSL-4 water based Nantero solution was used for all experiments. The pH of the solution was adjusted to 8. The concentration used was 1:100 SWNT solution to water. Figure 4.2 shows the assembled SWNTs before and after stripping the PMMA. When dispersed in DI water, the SWNTs assemble and align along the long axis of the trench. This assembly was not consistent and depended on the batches of SWNT solutions used. Alternatively using a dip coater to withdraw the substrate provided better control on the assembly and alignment of the SWNTs. The dip coater ensures the withdrawal of the substrate from the liquid at constant rate in a fixed direction. Figure 4.4 shows SEM images

of SWNTs assembled using the dip coater. Eventhough the dip coater is a more reliable process, the alignment of SWNTs is unidirectional. i.e. the SWNTs align only in the direction of withdrawal. In both cases, it is vital to maintain the hydrophobicity of the

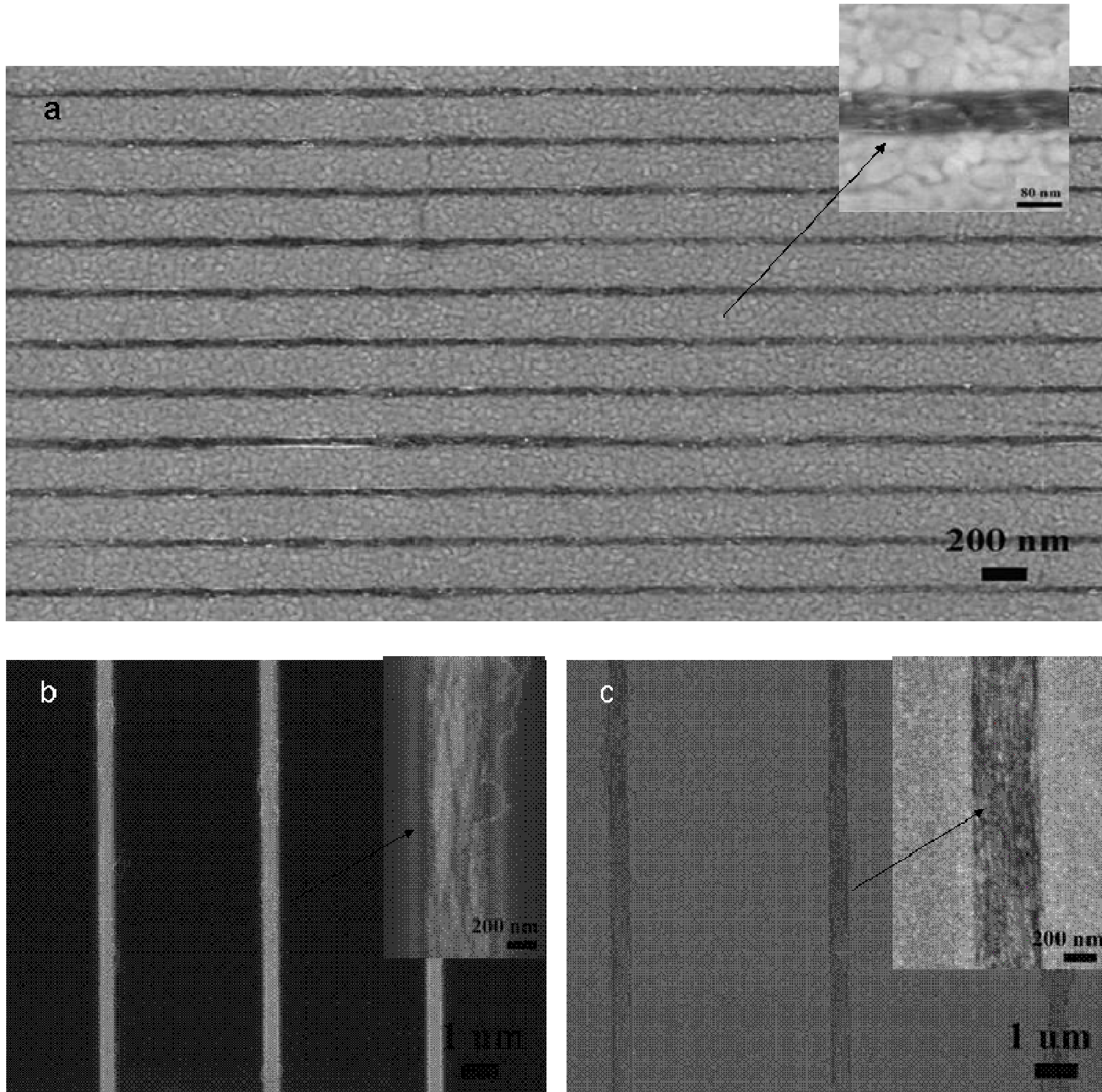

Figure 4.2: (a) SEM image showing large scale assembly of SWNTs (inset: high resolution image of SWNTs with width of 80 nm). (b) SEM image of SWNTs inside the PMMA trenches (c) SEM image of the same substrate after the PMMA has been dissolved.

PMMA. The alternate hydrophobic and hydrophilic surface helps in constraining the wetting of the liquid to the hydrophilic region. When the PMMA was treated with mild oxygen plasma, the surface became hydrophilic due to the incorporation of polar groups onto the

surface[139]. The open –OH bonds on the surface of PMMA changes the surface energy of the PMMA. Since the gold and the PMMA are both hydrophilic the wetting is no longer constrained to the gold surface. Hence SWNTs were also assembled on the PMMA surface.. When dispersed in IPA, the SWNTs assemble near the exposed gold patterns, with no alignment (Figure 4.3). This lack of alignment can be attributed to the lower surface tension of IPA compared to water. These experiments show the importance of surface energy on the assembly of the SWNTs.

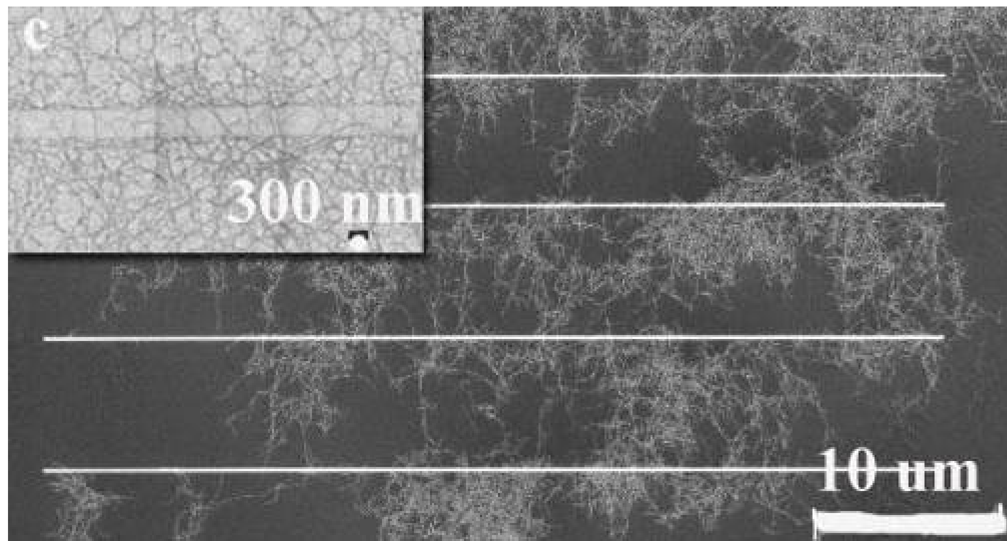

Figure 4.3: SEM image showing assembly of SWNTs on PMMA while using alcohol as the medium

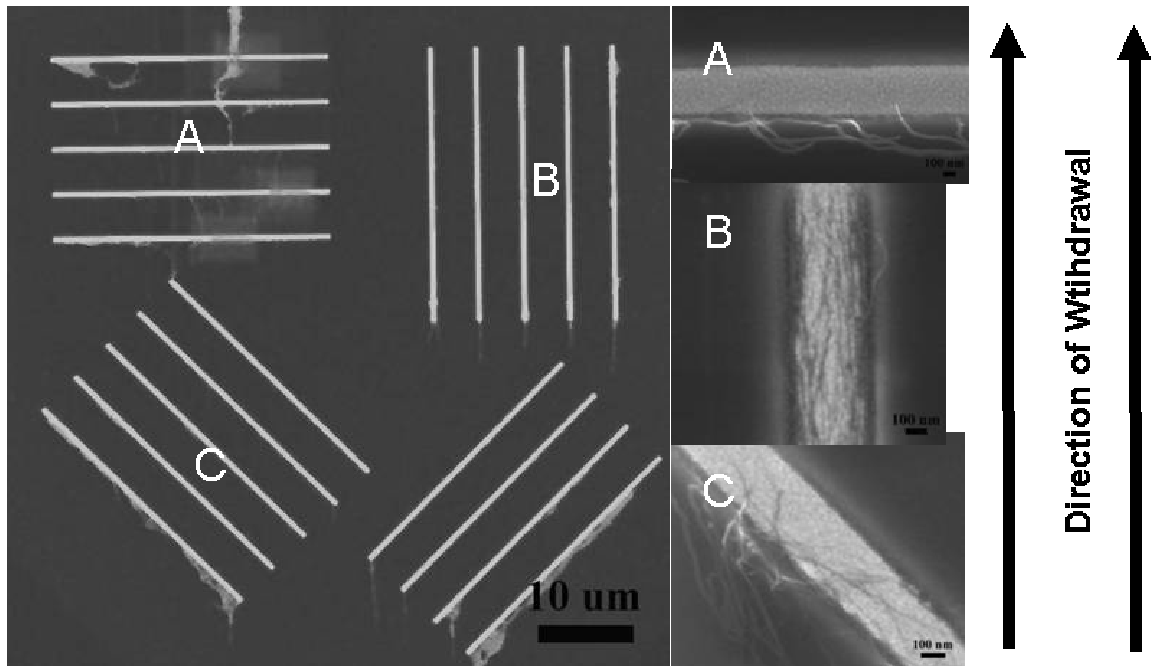

Figure 4.4 The effect of orientation of the SWNTs as a function of the angle between the patterns and the direction of withdrawal is depicted in this figure. The nanopatterns are (a) perpendicular, (b) parallel and (c) 450 degree angle to the direction of substrate withdrawal. It is observed that the orientation by dip coating is effective if and only if the direction of withdrawal is parallel to that of the nanopatterns.

Electric field helps in moving the SWNTs towards the electrodes. When a potential is applied between the electrodes, there is a peak in the current reading. This current drops sharply with time as the SWNTs start depositing on the electrode. The depositing SWNTs increase the electrical resistance. This increase in resistance could be due to either semiconducting nanotubes assembling on the electrode or the contact resistance between the deposited nanotube and the gold. Once the SWNTs completely coat the surface, the current between the electrodes becomes constant.

the density of SWNTs assembled increases with the increase in voltage from 3V to 5V. This can be seen from the experimental observations for the assembly of SWNTs at 3V and 5V as shown in fig 4.5. The amount of SWNTs deposited is also a function of the exposed surface

area of gold. Hence for a constant length and voltage, the decrease in trench width decreases the amount of nanotubes assembled inside the trench.

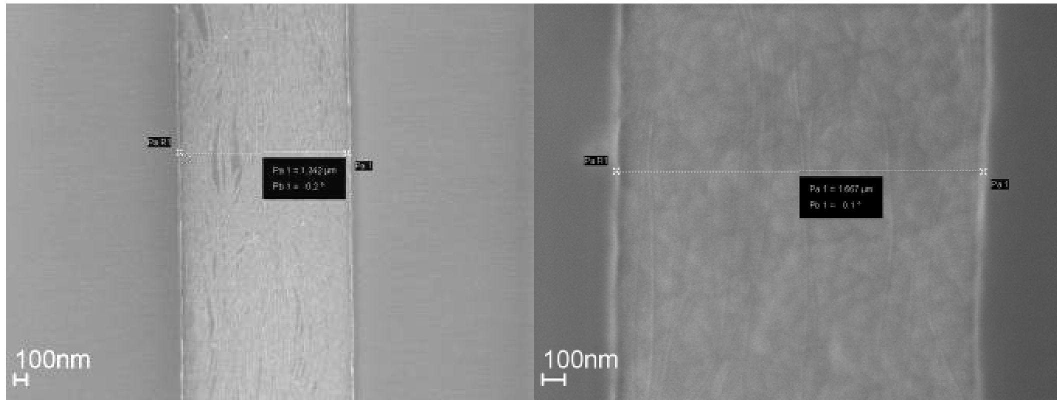

Figure 4.5: (left) Assembly of SWNTs in PMMA trench at 5 V (right) Assembly of SWNTs in PMMA trenches at 3 V for the same concentration of SWNTs

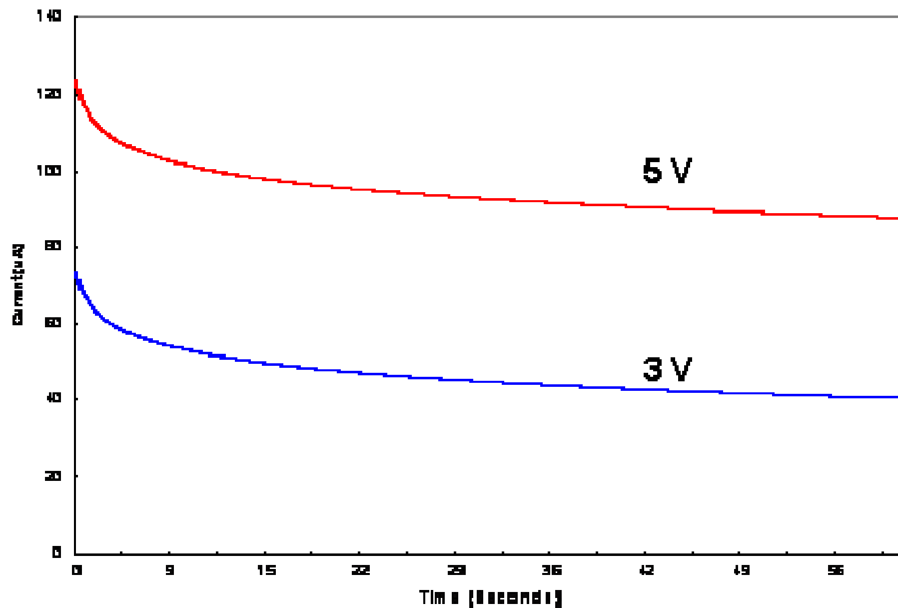

Figure 4.6: Plot of measured current vs time at 3V and 5V during assembly.

4.5.1 Mechanism of nanotube Assembly and Alignment

The assembly mechanism of the SWNTs is rather complicated due to the many variables that control the assembly process.Moreover, due to the small size and high rate it, is almost impossible to directly observe the assembly of the SWNTs. However, in order to control the assembly process, the SWNTs assembly mechanism and all the assembly parameters need to be identified and elucidated. In this chapter, we propose a a model based on experimental observations to explain the assembly mechanism.

Figure 4.7 shows the proposed hypothesis for the assembly mechanism. The SWNTs assemble on the exposed gold electrode anchoring at one or both end depending on the width of the trench during electrophoresis. The ends do not anchor on the PMMA because of its low surface energy and its insulating nature. The width of the PMMA trenches control how the SWNTs gets anchored to the substrate. As the substrate is pulled out of the solution, the dewetting liquid exerts a surface tension force on the SWNTs. The top of the SWNT tethers to the substrate due to higher adhesion force as compared to the surface tension force. As the fluid passes over the lower end of the nanotube, the surface tension forces stretch the SWNT aligning it. Any part of the SWNT that touches the PMMA surface is pulled back into the trench during the withdrawal and subsequent stretching process. The following discussion provides an in depth analysis of the different forces involved and elucidates why this is the most plausible scenario by correlating it with experimental results.

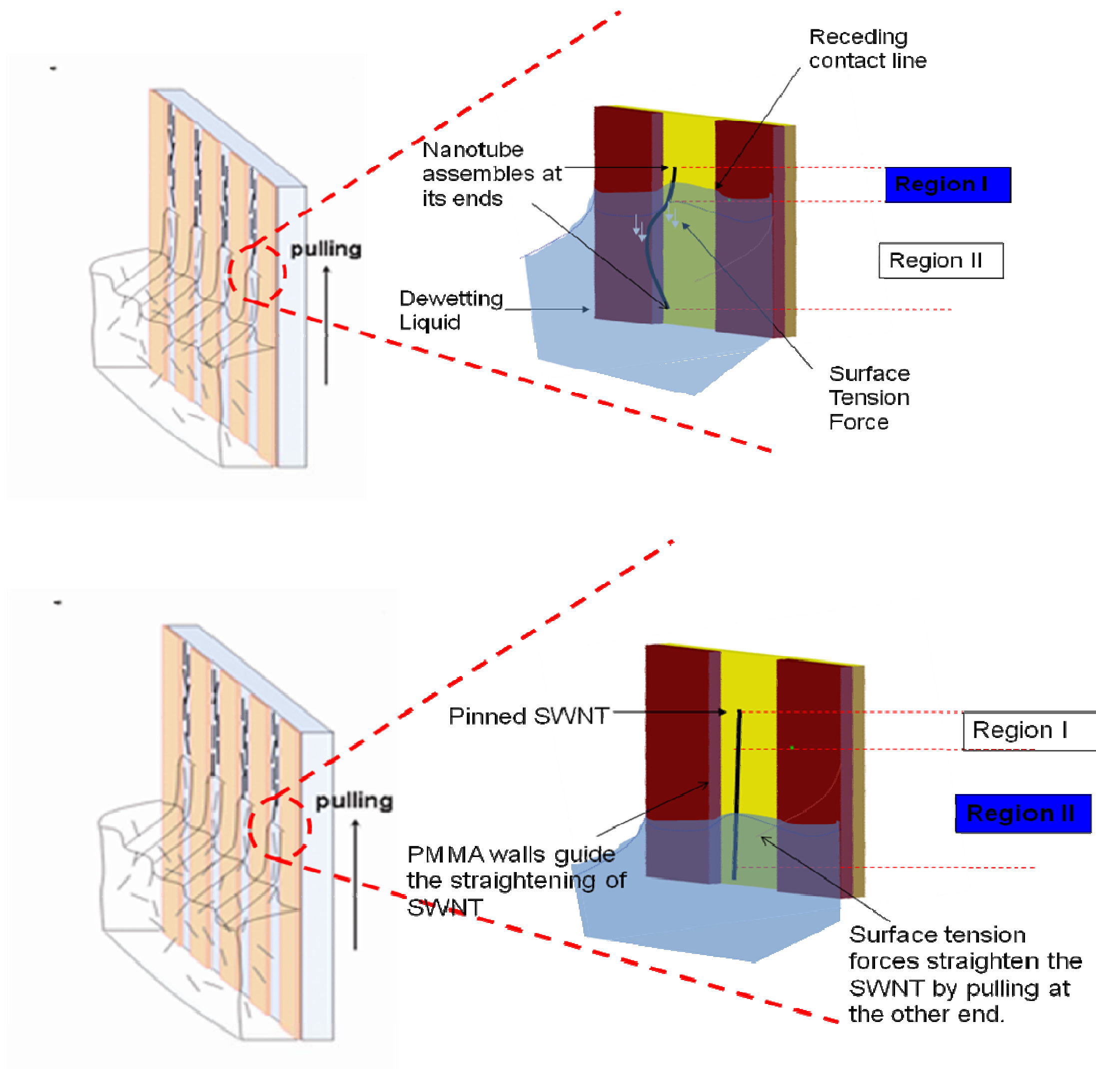

Figure 4.7: Schematic of Possible Assembly Mechanism

4.1.1.1 Assumptions

- The charges on the SWNTs are only at the ends, hence they attach only at their ends.
- Once attached, the ends of the SWNTs are in full contact with the substrate.
- The liquid completely wets the SWNTs.
- Water doesn't enter the tubes when dewetting.
- The capillary takes the shape of figure 4.15 (a) or 4.15 (b) at the leading end of the nanotube.

- The capillary takes the shape of figure 4.15 (c) at the receding end of the nanotube.
- **Forces involved**
    - **Electrostatic force is used to drive the SWNTs towards the substrate.**
    - **Van der Waals force due to the attraction between the SWNT and the gold surface.**
    - **The receding liquid applies a capillary and a hydrodynamic force on the SWNT.**

4.5.1.1 Electrostatic Force

SWNTs are terminated with carboxylic acid groups generated during the acid wash. When the SWNT is placed in water, the carboxylic acid dissociates into carboxylate ions. They inturn adsorb ions such as H^+ and OH^- from the aqueous solution leading to the presence of a net negative charge on the surface of the SWNTs[140].

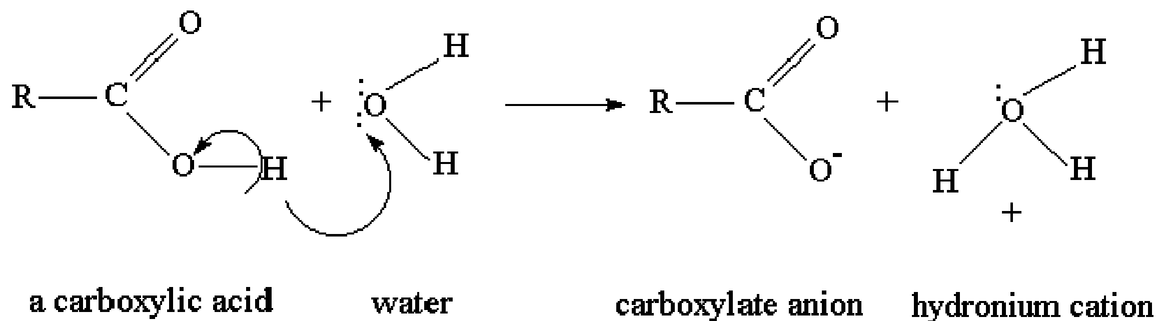

Figure 4.8: Dissociation of Carboxylic acide in water.

When a constant voltage is applied between the two substrates, the SWNTs start migrating towards the positive electrode. For open ended SWNTs the majority of the charges are located at predominantly at its ends. Figure 4.9 shows the zeta potential measurements of SWNTs in aqueous solution. The zeta potential measurement of SWNTs only provide approximate value as all zeta potential measurement techniques are designed for

spherical particles. The problems involved with carrying out zeta potential measurements with SWNTs is further elucidated in appendix C. In a solution having a pH of 8 the SWNTs the zeta potential is approximately -40 mV. Since for an open ended SWNT, the majority of charges are located at the ends, it is safe to assume a SWNT as two particles with equal charges connected to each other by a rod with no-charge. The net charge on each end of the SWNT can then be calculated by assuming a 2nm particle with a zeta potential of -40 mV.

The charge on a particle is $q = 4\pi R^2 \sigma \;=\; 4\pi R \xi \varepsilon_r \varepsilon_o (1 + kR)$ 4-1

where k is the Debye length given by $k^{-1} = 1 \big/ \sqrt{(8\pi\lambda N_b I)}$ 4-2

The Ionic Strength I is obtained from $I = 1/2\, \sigma (C_b Z_b^2)$ 4-3

Using a relative permittivity of 80.1 for water, the permittivity of free space as 8.85e-12 and the constant avagadro number (Nb) as 6.02E-23 we can calculate the charge on the nanotube. For water at room temperature the bjerrum length λ is 7.00E-10. The electric field is calculated using measured experimental data. For an exposed area of 15 x 10^{-10} m^2 (3 100nm x 100 μm trenches with 400 nm spacing) and applied voltage of 3V the measured current is 33μA. Hence the current density is 66000 V/m^2 (J = I/A). The conductivity of a pH 8 solution with NH_4OH and SWNTs was measured as 400 μS (1/ρ). Thus the electric field can be calculated for this particular trench geometry to be 1.65 x 10^8 V/m (E = ρJ). It has to be noted that this electric field is not constant and is influenced by the sharp edges of the trenches. A detailed study can be found in Kaveh et. al. However an approximate electrostatic force that is driving the nanotubes to the surface can be still calculated. From the charge the electrostatic force can be calculated using $F = Eq$ yielding 58.7 nN when assuming that the electric field affects the SWNT anywhere between the two gold plates. This electrostatic force assembles the SWNTs on top of the exposed gold electrodes

anchoring at its ends while the rest of the SWNT is free to float. Experiments have shown that when the substrate is withdrawn from the fluid without the electric potential present, no assembly of SWNTs is observed.

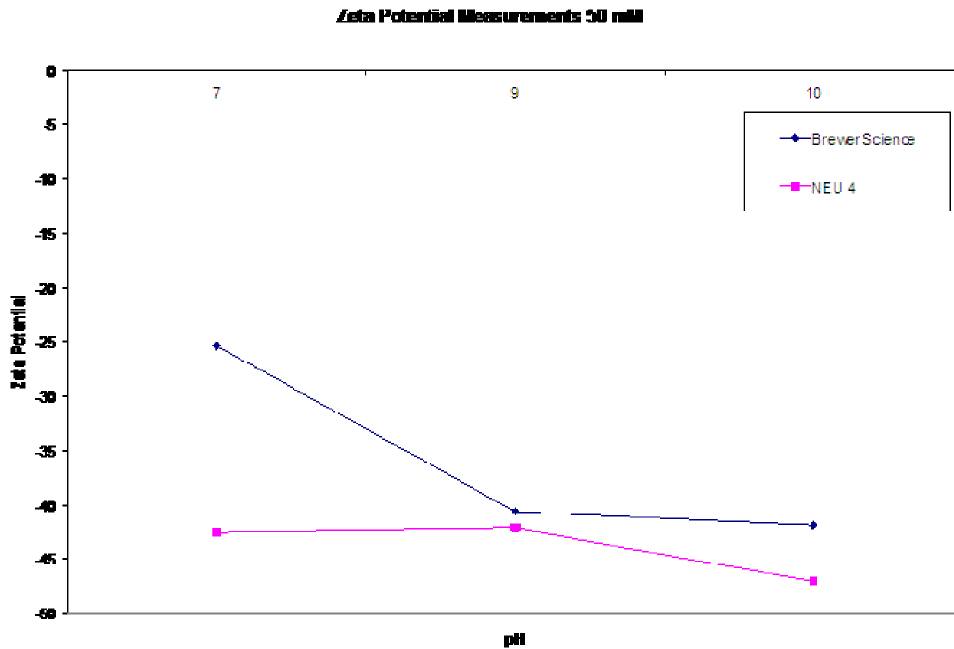

Figure 4.9: Zeta Potential measurement of SWNT in 50 mM KOH

4.5.1.2 Shape of the Meniscus

As the substrate is removed from the solution as in dip coating method, an ultra thin film of the solution is formed[141] due to dewetting. The use of a hydrophobic resist like PMMA confines the wetting of this liquid film to the nano/micropatterned geometries where the gold surface is exposed. In the absence of any external pressure the air-liquid interface of the solution filling the channel, recedes spontaneously with a convex shape. Figure 4.11 shows a computational fluid dynamics simualtion of a the dipping of a template with a 3 µm wide trench. The simulation was done using Flow 3D software considering only the forces imposed by dip-coating without any added external electric field, as the field has little effect

on the shape of the capillary. It has been shown that the shape of this air-liquid interface can be controlled by manipulating the dimensions of the trenches.

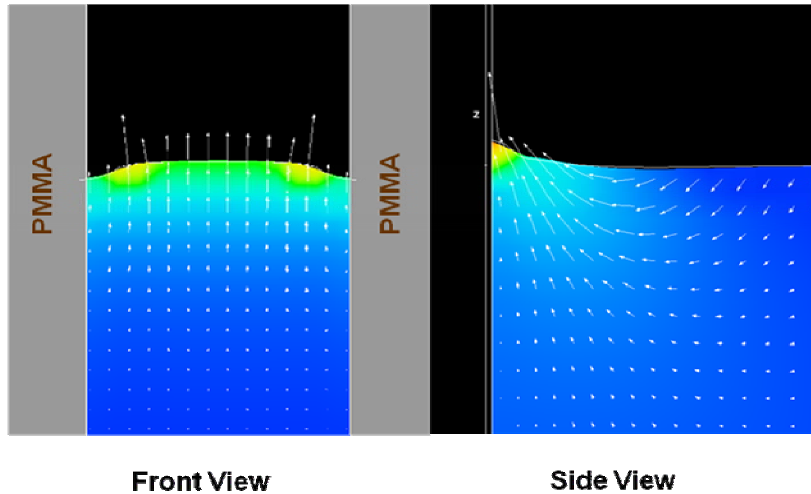

Figure 4.10: Flow 3D simulation of dip coating in 3 um trench

4.5.1.3 Calculation of fluidic forces

When the substrate is slowly pulled out of the solution at a constant velocity, the downwardly dewetting liquid exerts a hydrodynamic drag force[132] on the SWNTs[142]. Two extreme cases are considered, one where the flow is perpendicular to the SWNT, the second case is where the flow is parallel to the SWNT. To calculate the drag force, we need to first calculate the Reynolds number. The Reynolds number $\mathrm{Re}_L = \frac{\rho v L}{\mu}$ calculated for both cases is Re << 1 (Re~1.66e-6 for L=0.2 nm and Re~2.49e-3 for L=3μm). Hence the hydrodynamic force for the former can be calculated using an equation developed by Lamb for creeping flows past cylinders and the latter can be calculated using flow over an infinite cylinder ($C_D \propto Re^{-1}$). The drag force for the two cases is calculated to be $F_{d(lamb)}$=.174 pN and $F_d = 2.63 * 10^{-3}$ pN respectively.

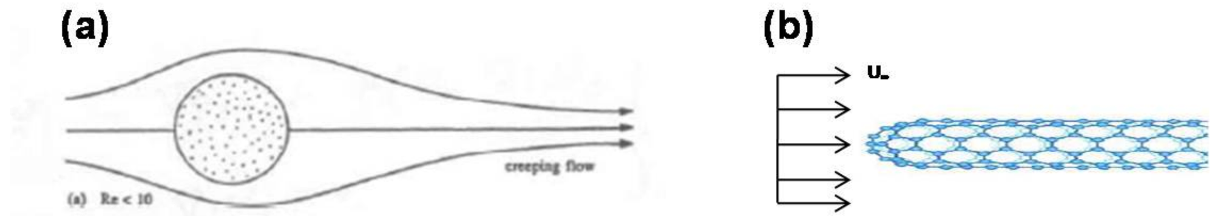

Figure 4.11: Hydrodynamic drag force for (a) flow perpendicular to the nanotube and (b) flow parallel to the nanotube.

In addition to the hydrodynamic force the moving meniscus exerts a surface tension force on the nanotube. For a rod of diameter D perpendicular to the surface of the interface, the surface tension force is given by,

$$F_{\sigma} = \gamma \pi D \qquad \text{4-4}$$

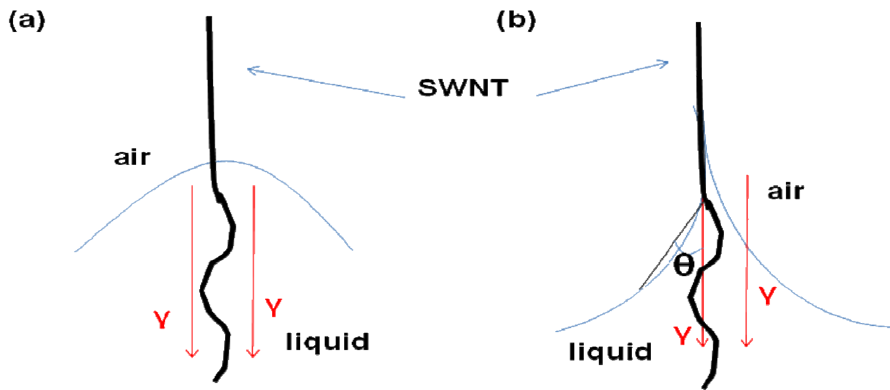

Figure 4.12: Surface tension forces (a) when the nanotube doesn't deform the contact line (b) when the nanotube deforms the contact line.

The surface tension of water (γ) is 72.8 x10^{-2} N/m^{2} and assuming a diameter (D) of 2 nm, the surface tension force acting on a single SWNT is about .45 nN. This equation assumes that the CNTs do not deform the contact line. However in reality, the CNTs deform the contact line, and it is the force due to the elastic deformation of the contact line, which is responsible for the alignment of the tubes. The elastic force of the three phase contact line is given by[143]

$$F_{\sigma} \cong \frac{\pi\gamma\theta_0}{\log L/D}.x \qquad 4\text{-}5$$

The contact angle of carbon nanotube is (θ_0) is 30° at the ends and taking L as the length of the trench (100μm) and assuming the distance through which the contact line is deformed[143] x = 10 nm the elastic force for a trench width (D) of 2 μm is about 0.45 nN. This force is of the same magnitude as the surface force without deformation. Thus it is safe to assume that the liquid completely wets the nanotubes..

If this stretching was due to shear force then all the SWNTs would have been aligned parallel to the substrate, also a simple comparison of the two forces show that the surface tension force is about 3 orders of magnitude higher than that of the drag force as seen in figure 4.14. Hence this stretching of the nanotube in the direction of the fluid flow can be attributed to something called molecular combing[144]. Molecular combing is phenomena that have been commonly observed in stretching and aligning of single DNA molecules, grafted or physiosorbed at one end onto solid surfaces. During a molecular combing process, the contact line (i.e. the edge of the droplet where the liquid, vapor and solid phases meet) exerts a local force on the molecule perpendicular to the liquid front. As the meniscus moves, it stretches the DNA and aligns it perpendicular to the contact line.

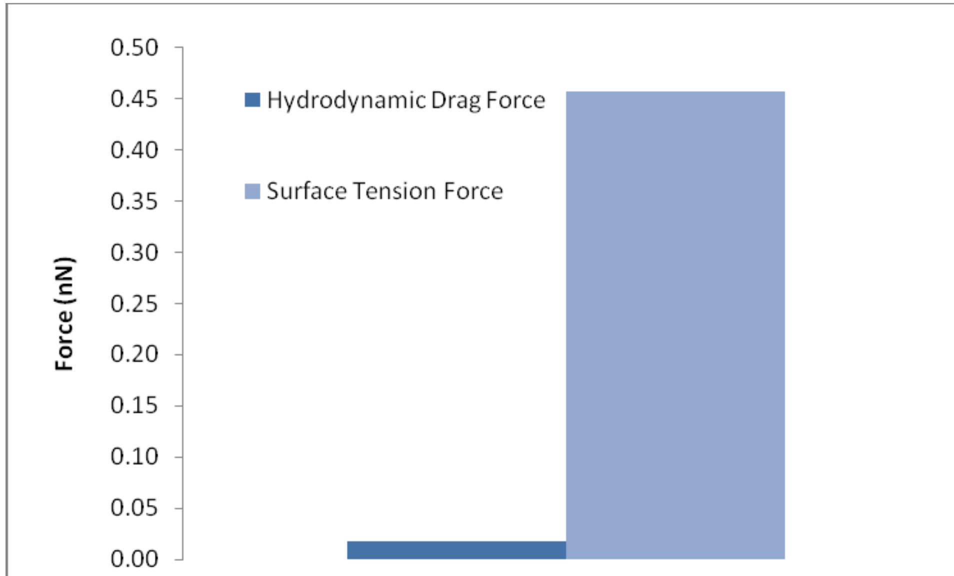

Figure 4.13: Plot comparing the Drag force with the Surface Tension force on the nanotube

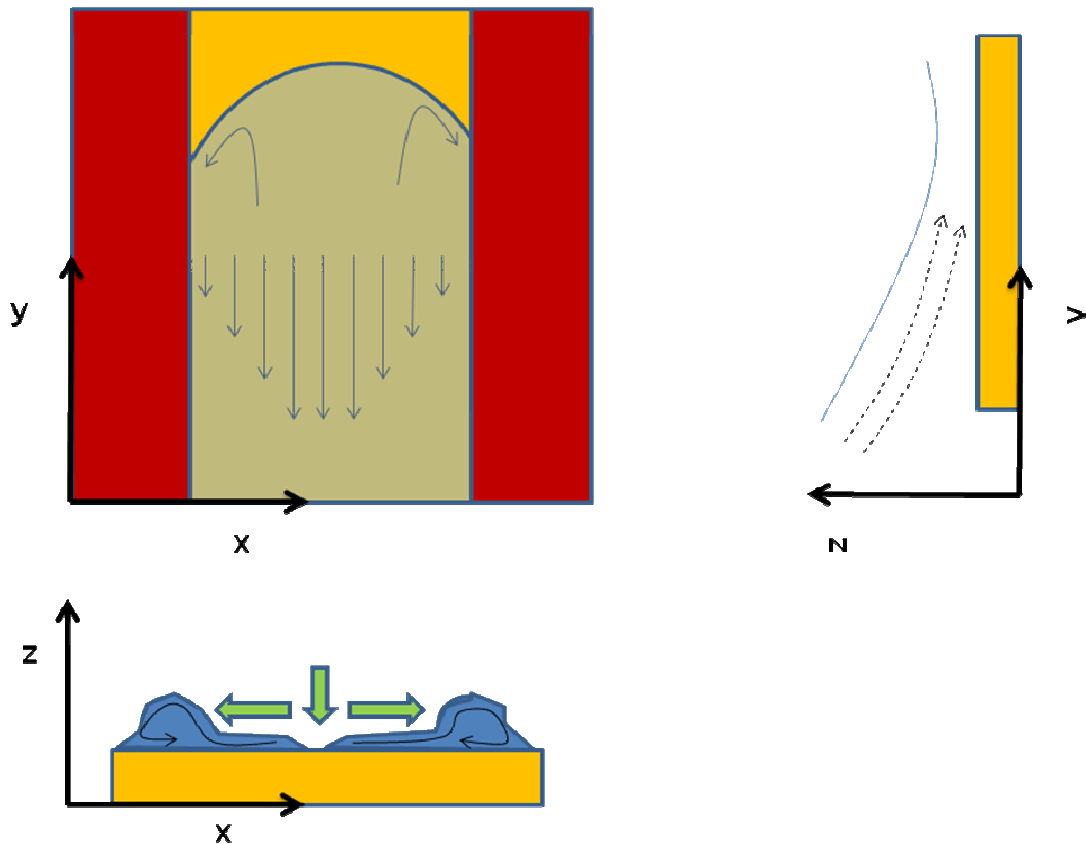

Figure 4.14: Schematics showing drying of the liquid from different axes.

4.5.1.4 Forces on the Assembled SWNTs

The SWNT is held onto the substrate by a combination of Van der Waals force, the electrostatic force and the capillary force. The resisting force to the surface tension force is the frictional force.

As the liquid dries, water gets trapped between the SWNT and the substrate. With the decrease in water content, a water bridge is formed between the substrate and the nanotube. As long as this water bridge is smaller than the diameter of the SWNT, the capillary forces would pin the SWNTs. Once the water level increases beyond a certain level where the air- water curvature changes from concave to convex, the capillary force would pull the SWNTs from the surface. Assuming the SWNTs ends to be spherical we can calculate the capillary force using the equation

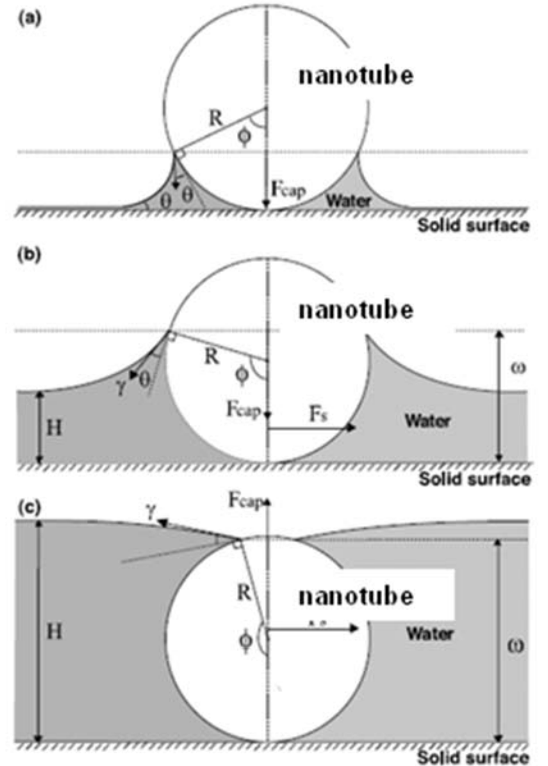

Figure 4.15: Different Scenarios of Capillary formation around SWNT

$$F_{cap} = \pi R \gamma \left[2\sin\phi \sin(\theta+\phi) + \cos\theta(1+\cos\phi)^2 - \sin\phi\right] \qquad 4\text{-}6$$

Where R is the radius of the SWNT, γ is the surface tension of water, φ is the filling or immersion angle between the center of the nanotube and the water-nanotube contact line, θ is the water contact angle on the nanotube. For a cylinder on a plane substrate the capillary force is given by[145]

$$F_{cap} = 2L\gamma\left[\frac{R\cos\theta + \cos(\varphi+\theta)\sin\varphi}{R(1-\cos\varphi)} + \sin(\varphi+\theta)\right] \qquad 4\text{-}7$$

With current instrument limitations it is impossible to measure the contact angle of a SWNT. But the contact angle can be obtained by indirect method. As mentioned above the open ended nanotubes have carboxylic acid all along it is circumference. Carboxylic acid groups are hydrophilic and the contact angle measured on a monolayer of carboxylic acid[146] is about $30^o - 40^o$. Molecular dynamics simulations show that for a bare carbon nanotube the contact angle is about 100°[147], making it hydrophobic. Using contact angles of 30 and 100, the capillary force for a 2nm diameter nanotube with varying filling is calculated and plotted in figure 4.16.

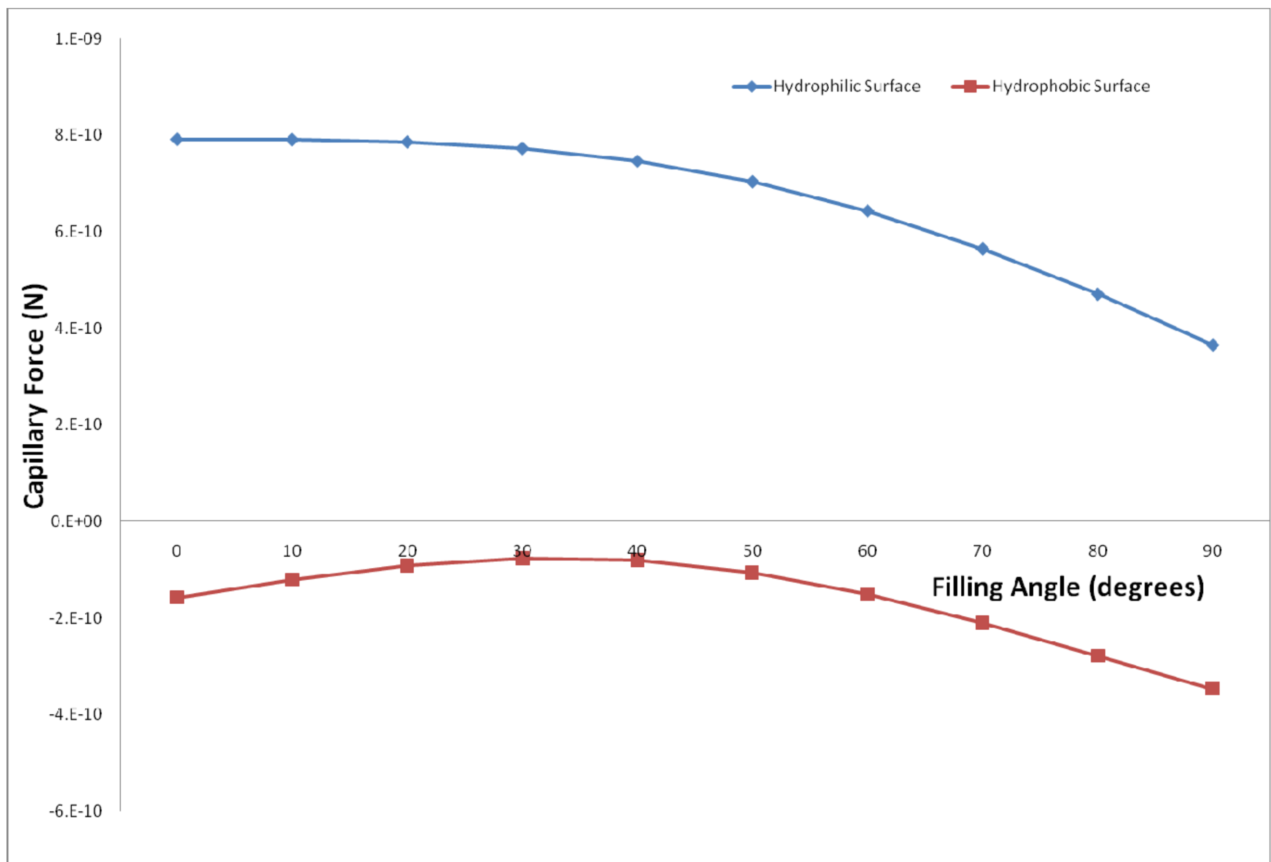

Figure 4.16: Plot of varying filling angle for contact angle of 30° and 100°.

Van der Waals forces produce attractive interactions between bodies, and play a key role in carbon nanotube adhesion. The Van der Waals forces are what keep the nanotubes in place

after the water has receded. For a cylinder interacting with a flat surface the Van der Waals force can be calculated using the following expression[148]

$$F_{vdw} = \frac{A_{132} d^{1/2}}{16 z_0^{5/2}} L \qquad \text{4-8}$$

Where A_{132} is the Hamaker constant between the particle and substrate in the presence of a medium and is given by

$$A_{132} = (\sqrt{A_{11}} - \sqrt{A_{33}})(\sqrt{A_{22}} - \sqrt{A_{33}}) \qquad \text{4-9}$$

Where A_{11} is the Hamaker constant of the cylinder (in this case the nanotube), A_{22} is the Hamaker constant of the substrate and A_{33} is the Hamaker constant of the medium (air/water). The values of these constants are listed in table.

Material	**Hamaker Constant (J)**
Gold (Au)	40×10^{-20}
Carbon Nanotube[149, 150]	$\sim 50 \times 10^{-20}$
Water	4×10^{-20}
Air	~0
PMMA	7.1×10^{-20}

Table 4-1: Hamaker constant of different materials.

Figure 4.17 shows the variation of the adhesion force due to Van der Waals attraction between the substrate and the nanotube with respect to the diameter of the nanotube both in air and water for a nanotube of length 1 nm and a distance of separation of .4 nm.

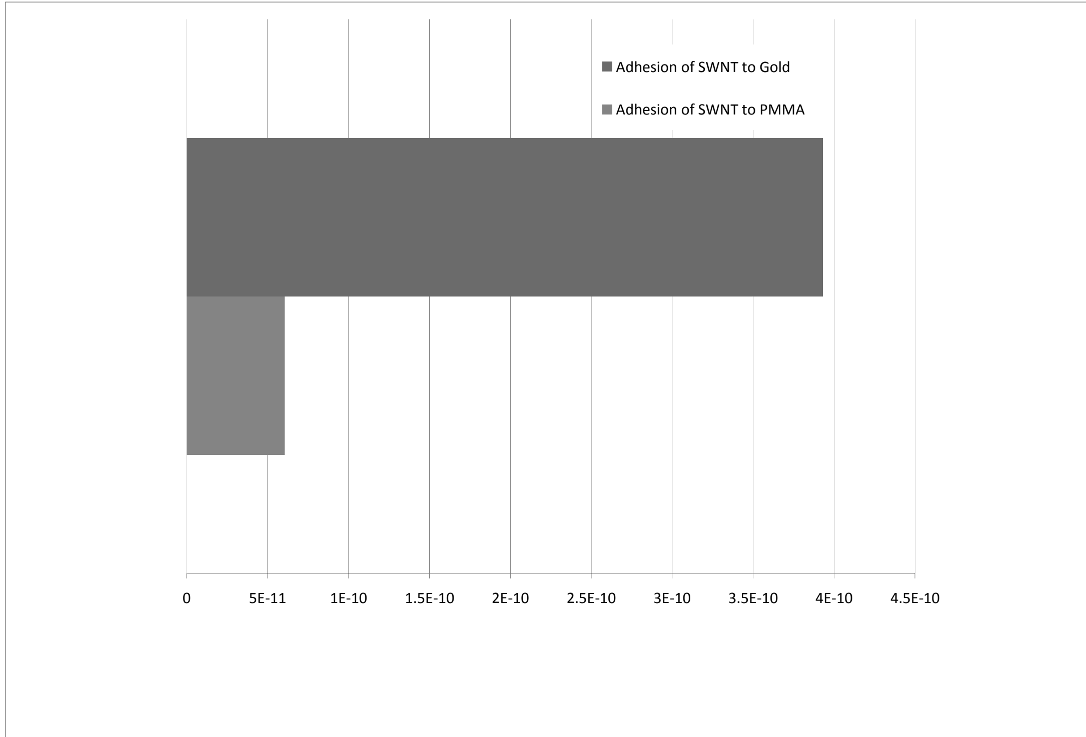

Figure 4.17: Comparison of adhesion forces and electrostatic force on SWNTs

As the liquid moves past the SWNT, the counteracting force for an absorbed SWNT is the frictional force that resists the movement of the nanotubes. The frictional force can be calculated from the total normal force that is holding the SWNTs in place is F_{cap} +F_{vdw}+ F_{elec} using the following relation

$$F_{fric} = \mu(F_{cap} + F_{vdw} + F_{elec}) \qquad 4\text{-}10$$

The coefficient of friction for nanotubes have been measured experimentally by various groups to be between 0.1 to 1.0, and is noted not to change with humidity. Hu et. al.[151] measured vertical nanotubes on 440C stainless steel to be about 0.2 in both air and nitrogen. Whereas Tu et. al.[152] found that the coefficient of friction for MWNT on AAO (anodized alumina) to be between .075-.117. Dickrell[153,154] carried out studies of MWNTs on Au substrate and found the coefficient of friction between nanotube and Au is between 0.6 -0.8

when they are vertical and 0.09 for nanotubes dispersed on flat rigid substrate. As expected the carbon nanotubes exhibit excellent self lubricity, previously observed in carbon materials like graphite and glassy carbon.

4.5.1.5 Mechanism of the SWNT Assembly

In order to explain theproposed mechanism, we divide the whole process into two regions (figure 4.4). In region I, the leading edge of the SWNT gets pinned onto the substrate due to the adhesion force provided by the Van der Waals and the liquid capillary. At the top end the capillary should take the shape as denoted in either figure 4.15a or 4.15b and not figure 4.15c. If the capillary takes the shape of 4.15c, then the nanotubes would not stay in its place when the substrate is withdrawn from the solution. The experimental observations show that this is not the case. Once the leading end is pinned onto the substrate, the surface tension would have to overcome the frictional force in order for the leading edge of the SWNT to come off. Assuming complete contact of the SWNT with the substrate, the frictional force can be calculated using a coefficient of friction 0.09. Since F_{fric} (5.337 nN) > (0.45 nN), the leading end of the SWNT cannot be removed or realigned.

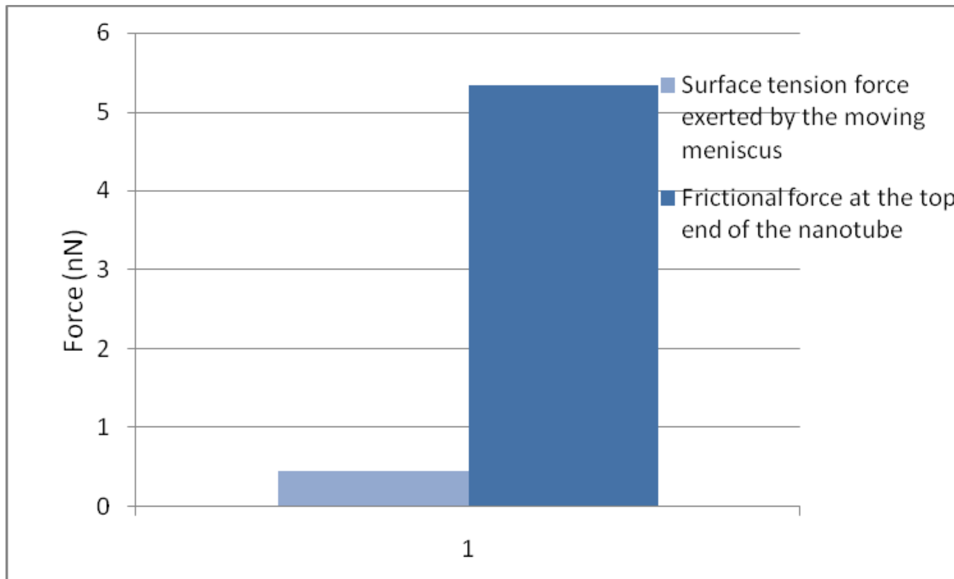

Figure 4.18: Comparison between frictional force and surface tension force acting on the leading edge of the SWNT.

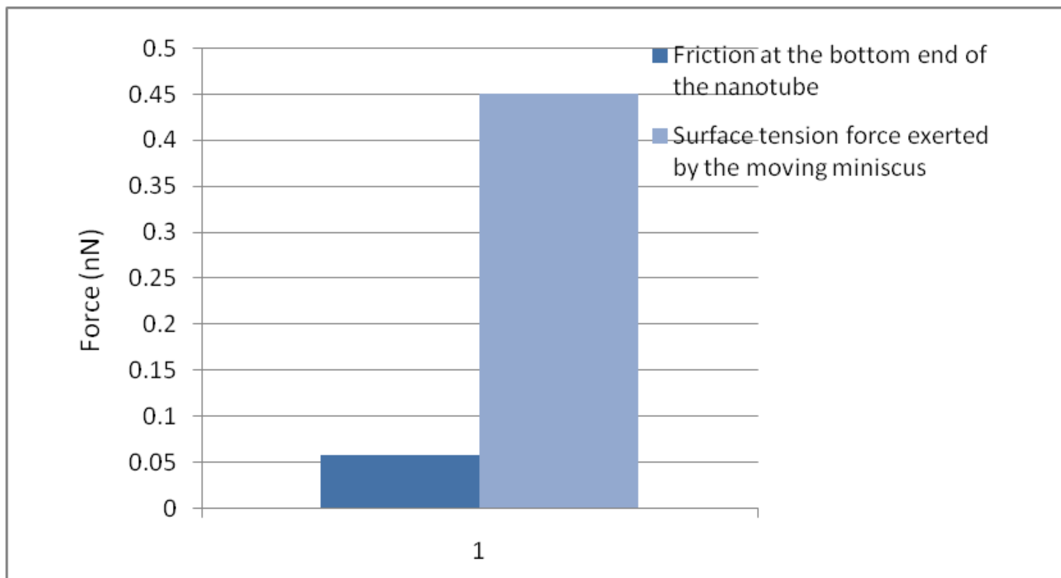

Figure 4.19: Comparison of Frictional force and Surface tension force acting at the bottom end of the SWNT.

As the liquid dewetts, the surface tension force needs to overcome the frictional force at the bottom of the nanotube in order to rearrange it.At the receding end the SWNT is completely immersed in water and hence the capillary takes the shape as shown in figure 4.15 (c). Moreover the liquid trapped between the nanotube and substrate also acts as a lubricant

giving a a friction coefficient of 0.001[155]. The frictional force is calculated as before and is found to be .059 nN. Since this force is less than the surface tension force (0.45 nN), the meniscus can rearrange the receding end of the SWNT, thereby stretching it.

4.5.1.6 Effect of trench width

We can apply the proposed hypothesis to some of the experimental results obtained. Figure 4.20 shows the assembly of SWNTs in different sized trenches.

The control over the directionality of the SWNT is achieved by the trench width. For trenches that are wider than the length of the SWNT, the directionality cannot be accurately predicted. This is because the orientation relies on the initial assembly of the SWNT, which is completely random. By using a trench with width smaller than the length of the nanotube, the assembly of SWNTs can be constrained, and walls of the PMMA guides the alignment of the SWNT. The assembled SWNTs demonstrate very high alignment parallel to the direction of withdrawal of the substrate.

The degree of alignment of SWNTs is a function of both the trench width and the length of the nanotube. In the absence of an applied potential the concentration of the SWNTs has to be very high and the rate of withdrawal has to be very slow in order to obtain decent assembly. Xiong et. al. [156] have shown that SWNTs can be assembled inside submicron sized trenches on silicon substrate when using a very high concentration and withdrawn at a rate of 0.1 mm/min. But when the substrate was pulled out of the solution without carrying electrophoresis at 50 mm/min, SWNTs were found neither on gold nor on silicon substrates. For successful assembly without electrophoresis, the entrained film should have enough concentration of SWNTs. At higher speeds the film is too thin and need a higher concentration and additional forces for the assembly to take place.

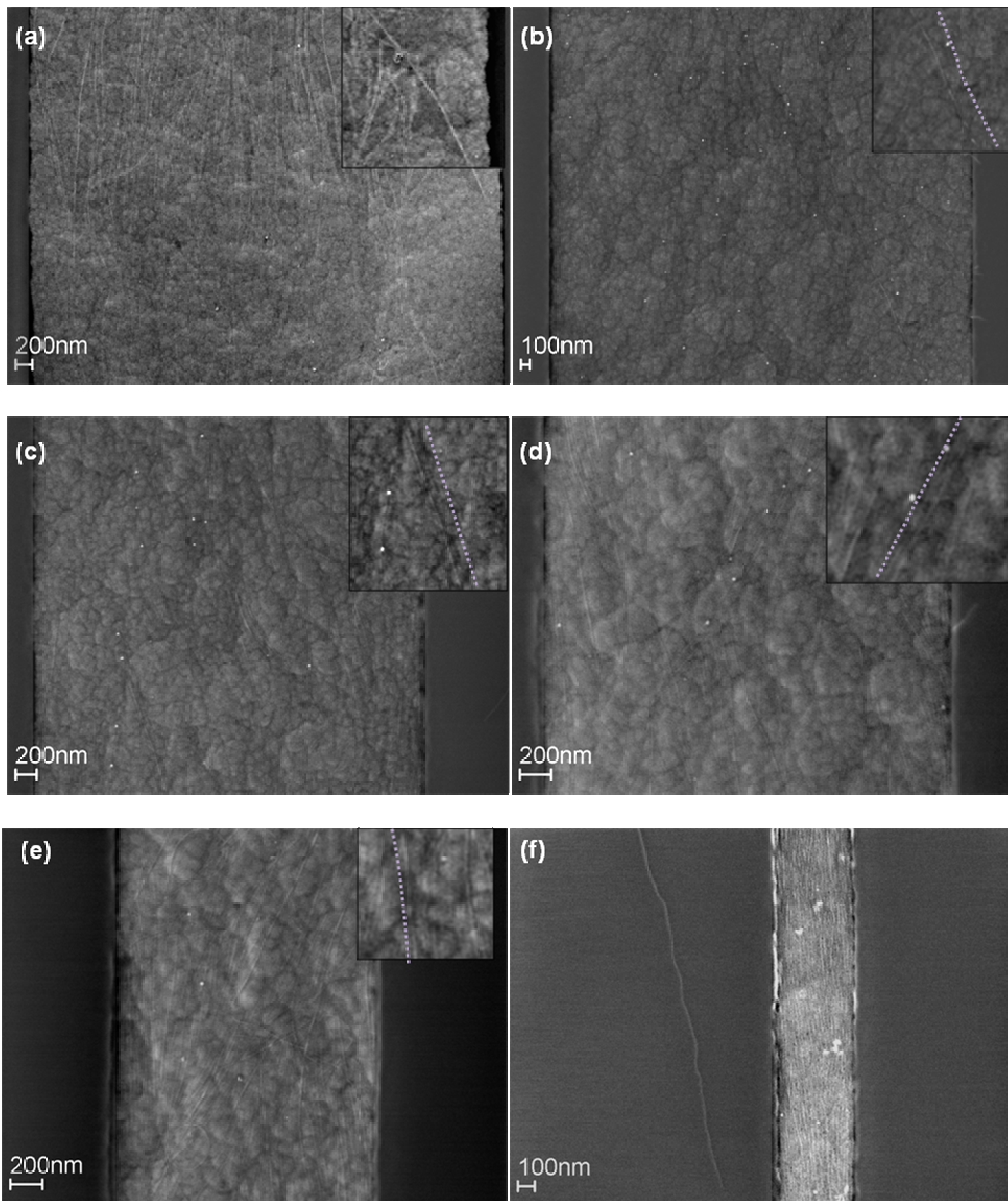

Figure 4.20: SEM micrograph of SWNT assembly in trenches with different widths (a) 5.5 µm (b) 4.5 µm (c) 3.5 µm (d) 2.5 µm (e) 1.5 µm and (f) 500 nm

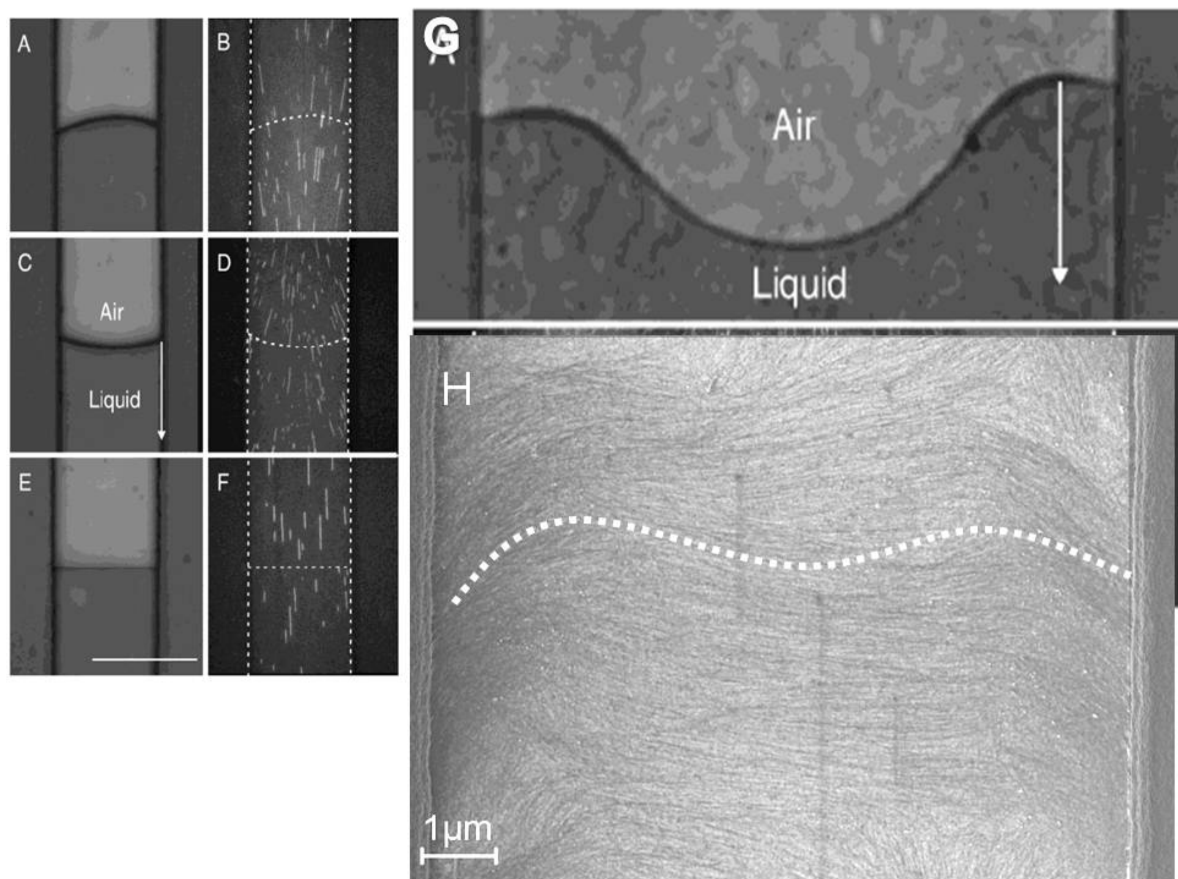

Figure 4.21: Optical images showing the shape of the capillary in 100 µm channel[118] (A) at slow speed (C) in vaccum (E) at a speed to get flat interface and corresponding assembly of the DNA. (G) Combing in 500 µm channel (H) SEM of carbon nanotubes assembled in 9 µm trenches.

As seen in figure 4.21 (H), in larger trenches the SWNTs take a very complex shape. Once the trench is much larger in size than the SWNT, there are high chances of the SWNTs assembling perpendicular to the direction of withdrawal. As shown in figure 4.21 (G), the capillary takes a complex shape as the trench size increases. It has been rationalized that for larger trenches with same depth the wall chemistry loses importance in relation to the velocity of the fluid in the center of the trench.[118] Unfortunately we don't have the capability to visualize the air-water interface for our particular case, especially the small perturbations. By comparing the experimental result 4.21 (G) to the observed result in 4.21 (H), we can reason that the air-water interface is taking a similar shape at the nanoscale. Since the

surface tension acts perpendicular to the air-water interface, this complex air-water interface should stretch the nanotubes and align them in this wavelike formation.

In addition to the alignment we also observe that the SWNTs assembled inside the trenches tend to assembled at the corners more than at the center of the trench. The fact that SWNTs assemble more at the edges than at the center could be attributed to both the effect of the electric field and evaporation of the liquid. A simplified model developed using a computational fluid dynamic software CFD-RC showed that the electric field strength in region I at the edges is twice as strong in magnitude as the electric field in region II resulting in more particle/nanotube assembly at the corners[157].

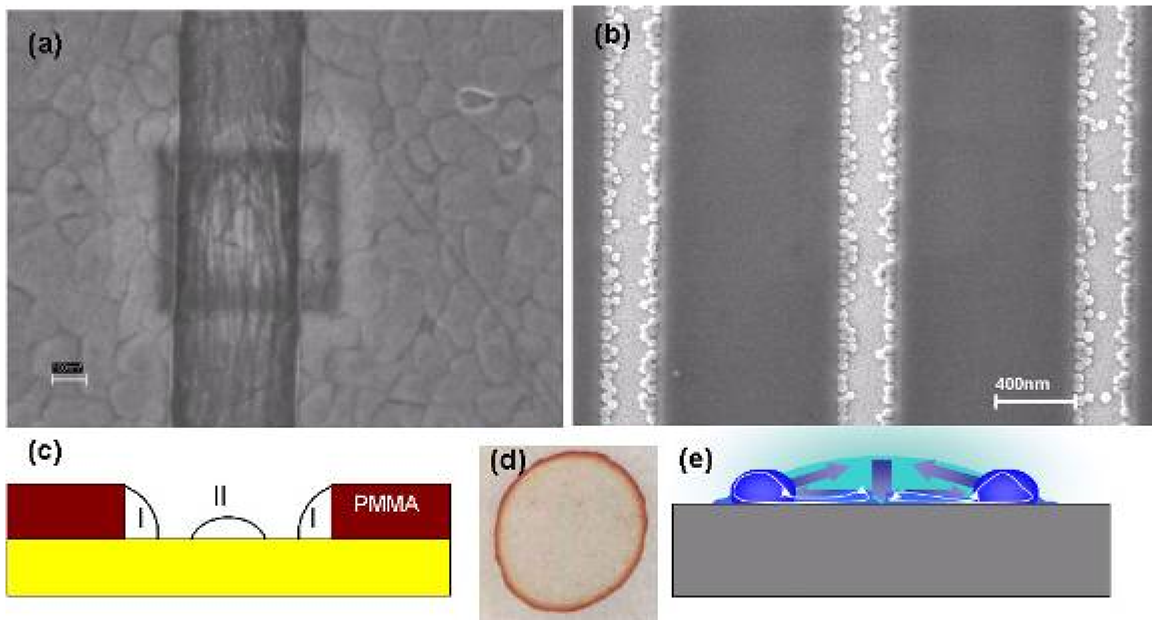

Figure 4.22: (a) SEM image of SWNTs assembled on gold, showing higher density of SWNTs at the edges (b) SEM image of particles assembled on gold, showing similar assembly predominantly on the edges (c) Two different regions of electric field intensity (d) Coffee stain effect when a droplet is left to dry on a surface (e) An evaporation model showing the liquid flow during drying[159,158].

In addition, evaporation causes bubble formation at the outer surface. It has been observed that the residues left by drying drops of suspension, such as coffee, are significantly darker or more concentrated at the perimeters[158, 159]. Young's condition[160] determines the

equilibrium of the three phase contact line of a liquid, which states that when the liquid evaporates from a drop, the drop will maintain a constant shape, by shrinking, as a consequence of equilibrium. In the case, where the contact line gets pinned, due to evaporation, there must be a net flow of liquid to the contact line, carrying any particle that is present in the suspension[161]. The particles that accumulate might exert a sufficient pinning force on the contact line, causing phenomena called self pinning and a greater buildup of particles takes place. This complicated evaporation of the solution also takes place within the trench, with the water moving from the center to the edges causing a buildup of SWNTs at the edges than at the center.

4.6 SWNT Interconnects

The goal of this project is to eventually make devices and interconnects using the assembly technique developed. Due to their excellent electrical properties there has been intense activity exploring the electrical properties of these nanotubes and their potential applications in electronics. Experiments and theory have shown that their electrical properties can rival the best metals or semiconductors known. The first electrical studies on metallic nanotubes were done in 1997[162] and the first on semiconducting tubes in 1998[163]. Metallic SWNTs are predicted to show ballistic transports at room temperature, a phenomenon which is observed only at very low temperatures in case of most metals. A SWNT is identified as metallic when its room temperature electrical conductance is insensitive to gate voltages applied by an electrode separated by a few hundred nanometer dielectric. The gate voltage electrostatcally changes the chemical potential or Fermi energy of the nanotube. But in the case of metallic nanotube, the shift in Fermi energy does not significantly change the density of states at the Fermi level, hence producing no significant change in conductance.

The fundamental resistance of a single SWNT can be calculated using the two terminal Landauer- Buttiker formula. For a system with N 1-D states in parallel the relation is given by $G = (Ne^2/h)T$. In case of a perfect contact the transmission probability (T) for electrons through the channel is 1. SWNTs have either two valence or conduction bands and each can support both spin up and down electrons, thus there are 4 effective channels N =4 [164,165]. Therefore the fundamental resistance of SWNTs that cannot be avoided is 6.45 kohms (conductivity of 155 uS). Compared to Si CMOS, this is quite a large resistance and will be a challenge to implement in integrated circuits. In order to obtain the lowest resistance; SWNTs have to be assembled in parallel. It should be noted that achieving this theoretical limit from a practical point of view is not trivial, and special attention must be paid to the contact between the nanotube and the source/drain electrode.

4.1.1. Fabrication of Nanotube Interconnects

SWNTs were assembled in PMMA trenches as explained in the earlier section. The PMMA is then dissolved using acetone to expose the SWNTs on Au.

- Write down the coordinates of the assembled SWNTs with respect to a cross marked on the Au.
- Spin 150 nm thick electron beam resist (1:1 Nano 950 PMMA: Anisole) over the SWNT and Au surface. Followed by soft baking at 180 ºC for 90 seconds.
- Expose the PMMA using FESEM using the coordinates obtained earlier.
- Develop the exposed PMMA first using 1:3 MIBK:IPA for 70 seconds and then in IPA for 20 seconds. Followed by DI water rinse for 5 minutes.
- Wet etch the Au in the exposed areas using Transcene gold etchant GE-8148. (etch rate 50 A°/sec).

- Rinse in DI water for 5 minutes to get rid off all the gold etchants.
- Wet etch the exposed Cr adhesion layer using Cr mask etchant (800 A°/min).
- Rinse in DI water for 5 minutes.
- This process will make two contact pads and eliminate the device from the bulk gold surface.

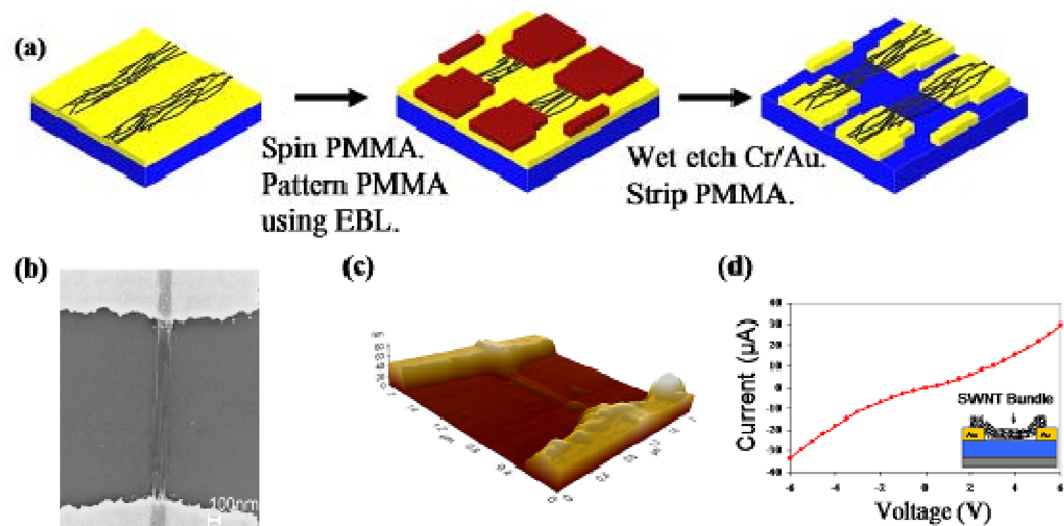

Figure 4.23: (a) Schematic diagram of the test structure obtained as a result of post fabrication processes after assembly. (b) Top down SEM image of the assembled SWNT bundle with electrodes. (c) AFM image of the assembled SWNT bundle. The height of the assembled SWNT is approximately 15nm. (d) Typical I-V curve for one of the assembled SWNT bundles. Inset shows a cross-section of the test structure.

To carryout electrical characterization of the assembled SWNTs, we spun PMMA on top of the SWNT/gold layer and patterned the PMMA using electron beam lithography. The exposed Au/Cr layer was then etched to define the contact pads. Each pair of contact pads consisted of five 120 nm parallel bundles of SWNTs bridging a distance of 800 nm.

Electrical measurements were taken on 5 different samples. The room temperature I-V curves of the SWNT bundles were linear exhibiting an ohmic behavior. Although electrophoresis is believed to be non-selective towards one particular species of SWNT, we still observe a linear behavior. This is because even the presence of a small number of metallic SWNTs would produce a linear behavior due to a very high drive current through metallic SWNTs compared to semiconducting SWNTs. The resistance between the source and the drain was calculated to be 200 kΩ. This yields a resistance of 6 MΩ per bundle. The measured resistance comprises of metal/metal, metal/semiconducting and semiconducting/semiconducting junctions in addition to the resistance of the nanotube itself. This resistance value would decrease as SWNT dispersion techniques mature and SWNT-metal contacts are improved. Nevertheless the measured resistance is well within the range of resistances reported in literature for nanotubes adsorbed on prefabricated electrodes[166,167]. This extra processing step also enables us to demonstrate the concept of large scale electronics using our assembly technique.

4.7 SWNT based Field Effect Transistor

Probably one of the most important applications for SWNTs is in making Field effect transistors. After assembly additional processing steps can be introduced to make fully functional devices, for example an oxide layer can be deposited by chemical vapor depositing and metal gate electrodes added on top of the device to fabricate field effect transistors. Previous research has shown that nanotube FETs have clear advantages over scaling of traditional Si CMOS technology beyond the ITRS roadmap. One of the key advantages of CNT FETs are that they can be switched at very high speeds (upto THz). The use of SWNTs as FETs has been hindered due to the fact that the semiconducting nanotubes cannot be

separated from a mixture containing semiconducting and metallic nanotubes. The semiconducting nanotubes have a bandgap that is approximately 1 eV/d[nm], where d is the diameter. Semiconducting SWNTs can be turned off and on by applying a voltage to the gate electrode, whereas metallic SWNTs cannot be turned on or off. In order for a CNT based FET to be effective, the nanotubes should be all semiconducting. A work by Snow et. al.[168] at the Naval Research Laboratories revealed that low density networks (~ 1 μm^{-2}) of randomly distributed as grown SWNTs on substrates act as p-type semiconducting thin films. An alternative approach is to selectively burn[169] metallic SWNTs using very high current. People have exploited both as grown CVD method as well as post synthesis deposition method to make SWNT FETs. Typical motilities that have been reported for CVD-grown tubes are between 1000 – 10000 cm^2/Vs and sometimes as high as 20000 cm^2/Vs. This is significantly higher than that reported for deposited nanotubes which are around 0.5 cm^2/Vs to 50 cm^2/Vs[170,171,172].

The basic FET consists of two metal electrodes designated as source and drain connected by a semiconductor channel. Conventionally Si is used as channel, however in CNTFETs, the channel is replaced with Semiconducting nanotubes. A third electrode called the gate separated from the channel by a thin insulator film is used to modulate the current through the channel. When no charge is placed on the gate, no charge flows into the channel. In a p-type FET, when a negative charge is placed on the gate and the applied voltage V_{gs} exceeds a certain threshold V_{th}, current flows through the device. Similarly in an n-type FET, when a positive gate voltage is applied, that exceeds a certain threshold voltage , current flow through the device.

4.7.1 Fabrication of Nanotube FET

SWNTs were assembled in PMMA trenches as explained in the earlier section. The PMMA is then dissolved using acetone to expose the SWNTs on Au.

- Carryout a standard RCA clean on a Si wafer.
- Dice the wafer into 15 x 15 chips.
- Place the chip in the SCS parylene deposition system and deposit 10 µm of parylene.
- Sputter 100nm on top of the parylene/Si wafer using Material Research Corporation's DC magnetron sputter deposition system.
- Spin 150 nm thick electron beam resist (1:1 Nano 950 PMMA: Anisole) over the microfabricated Au electrode. Followed by soft baking at 180 ºC for 90 seconds.
- Expose the PMMA using FESEM.
- Develop the exposed PMMA first using 1:3 MIBK:IPA for 70 seconds and then in IPA for 20 seconds. Followed by DI water rinse for 5 minutes.
- Carryout electrophoretic assembly of SWNTs as mentioned in earlier section.
- Dissolve the PMMA using acetone for 10 minutes.
- Write down the coordinates of the assembled SWNTs with respect to a cross marked on the Au.
- Spin 150 nm thick electron beam resist (1:1 Nano 950 PMMA: Anisole) over the SWNT and Au surface. Followed by soft baking at 180 ºC for 90 seconds.
- Expose the PMMA using FESEM using the coordinates obtained earlier.
- Develop the exposed PMMA first using 1:3 MIBK:IPA for 70 seconds and then in IPA for 20 seconds. Followed by DI water rinse for 5 minutes.
- Deposit 100 nm of Titanium using Perkin Elmer 2400.

- With Ti as a mask, wet etch the Au in the exposed areas using Transcene gold etchant GE-8148. (etch rate 50 A°/sec).
- Rinse in DI water for 5 minutes to get rid off all the gold etchants.
- Peel the parylene along with the CNT device from the chip.
- Place it on a gold chip substrate that will act as the back gate. The device is now ready to be tested.

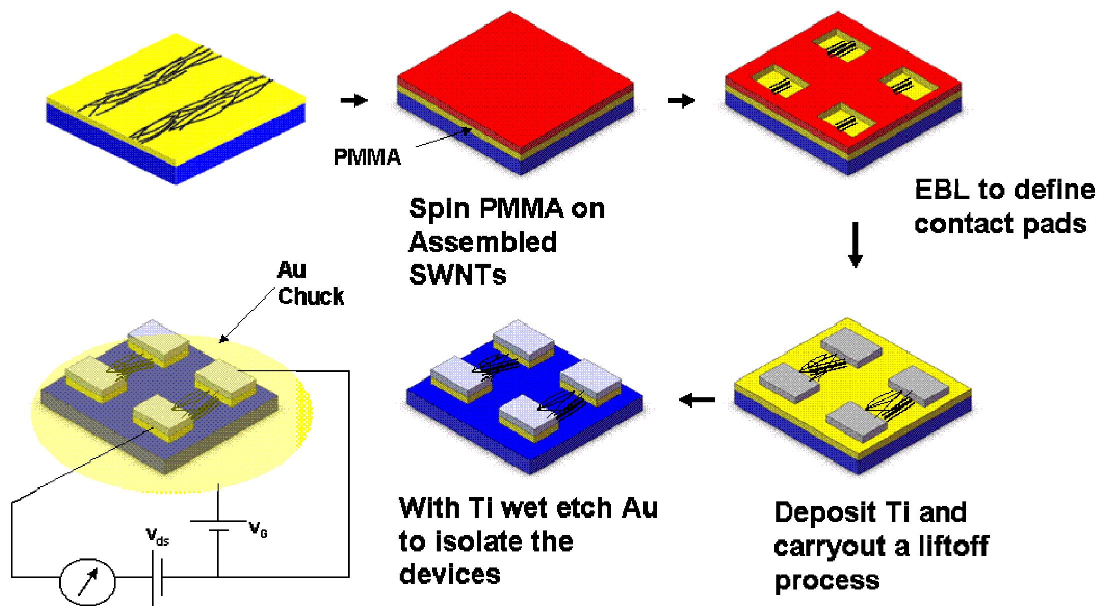

Figure 4.24: Fabrication process flow of SWNT FET

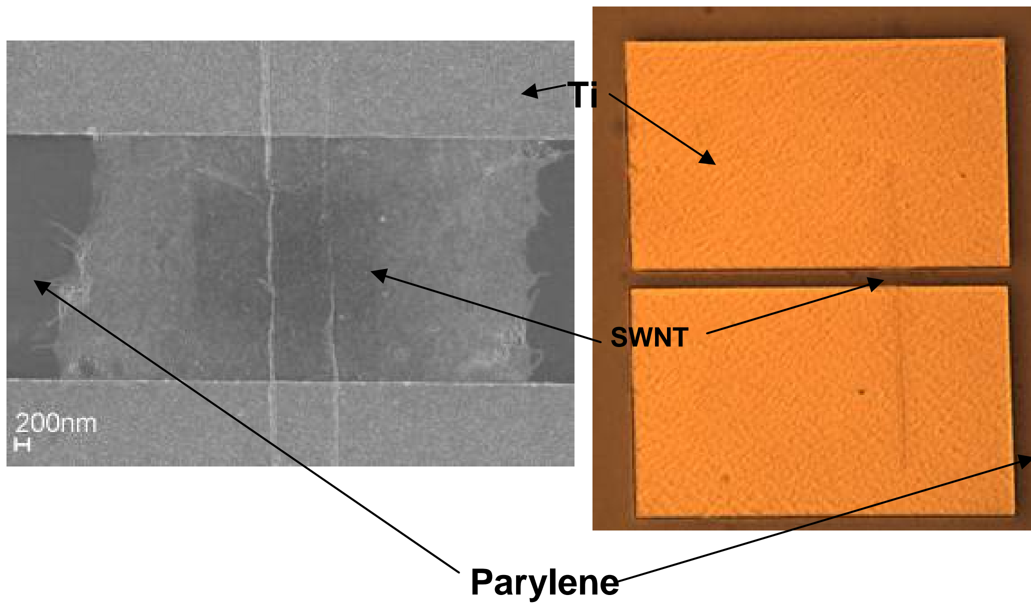

Figure 4.25: SEM and optical Images showing the SWNT device.

The field effect transistor consists of Ti electrodes as the source and drain and the bundle of nanotubes acts as the channel. The gate is made up of a 10 µm parylene layer. The bundle size is controlled by the size of the PMMA trench used during assembly. Gate voltage is passed using a gold chuck mounted on the probe station. Alternatively the parylene layer can be placed on top of a gold wafer or the parylene/Si layer could also be used. A HP semiconductor analyzer was used to apply voltage and measure the response of the nanotubes to change in gate voltage. The source –drain voltage was cycled from -1 V to + 1 V for different gate voltages ranging from -10 V to + 10 V. A single SWNT or a mesh of SWNTs without alteration generally demonstrates a p-type behavior. The SWNT bundle in our case demonstrated an n- type transistor behavior. This n-type behavior of the nanotube could be attributed to the doping of the nanotube during the gold etching process. The gold etchant used consists of potassium iodide, and it has been shown that potassium dopes SWNTs hence resulting in an n-type behavior. The mobility of the SWNTs can be calculated using the following relation

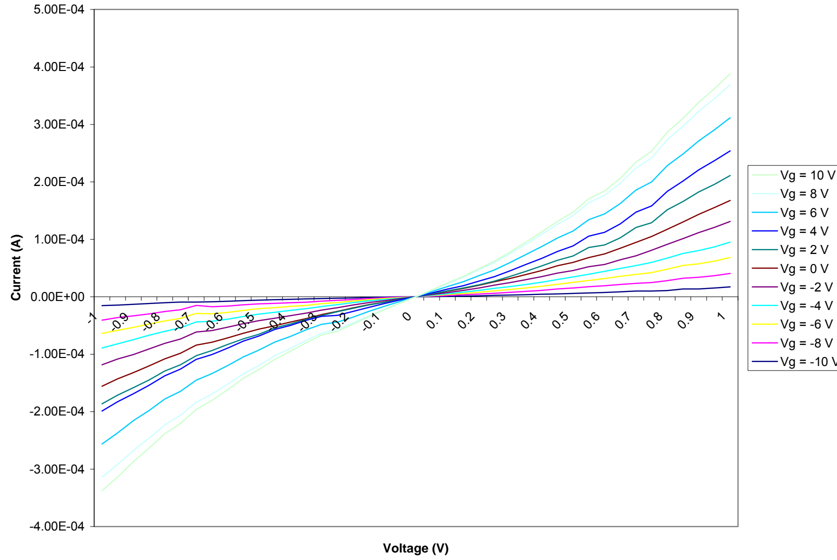

Figure 4.26: Typical I-V curve measured for different gate voltages

$$\mu_{eff} = \frac{(dI/dV_g)L_{ox}L_{SD}}{\varepsilon \omega_{SD} V_{SD}} \quad \text{4-11}$$

Where dI/dV_g *is the slope of the curve,*

L_{ox} *is the thickness of the dielectric*

L_{SD} *is the distance between the source and the drain*

ε *is the dielectric constant*

ω_{SD} *is the width of the channel*

V_{SD} *is the voltage applied between the source and the drain*

The dielectric in our case is parylene (ε of 3.15) and has a thickness of 10 μm. This distance between the source and the drain is 1 μm and the width of the channel is about 1.5 μm. Hence for a constant V_{SD} of 1 V the mobility of the transistor with transconductance dI/dV_g of 8 x 10^{-5} /V is ~ 6.25 cm^2/Vs. This is very close to the reported value for random network of SWNT FET[173] (4 cm^2/Vs).

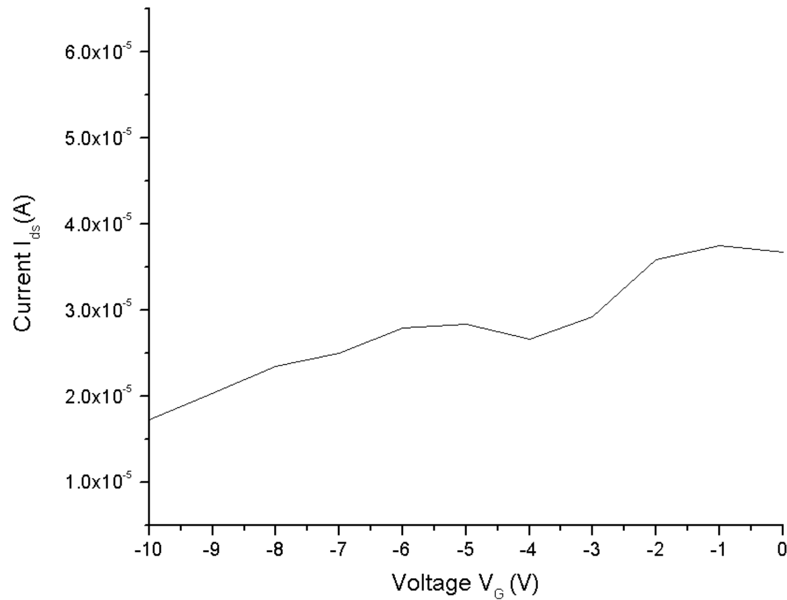

Figure 4.27: A typical I vs V_G (gate voltage) curve at a V_{SD} of 1 V

4.8 Summary

In conclusion we have demonstrated that, by employing both electrophoresis and dip coating, SWNTs suspended in solution can be assembled on pre-fabricated structures with precise alignment and control over large areas within a short period of time. It is also shown that the direction of substrate withdrawal significantly affects the alignment and orientation of directed assembly of SWNT bundles. Calculations show that the capillary force is the dominant force in the alignment of these SWNTs.

We have also successfully fabricated SWNT interconnects and FETs using the assembly technique developed. Both devices show comparable results to the datas published previously for single SWNT devices. The time period for assembly is short and hence scalability of this technique is quite promising. Since our technique involves no chemical

modification of the substrate our process can be easily integrated with the current CMOS fabrication process, resulting in the realization of mass production of SWNTs based devices.

5 Chapter 5: 3D SWNT Architecture Using Dielectrophoresis

5.1 Introduction

Three-dimensional (3D) integrated circuits (ICs), contains multiple layers of active devices, and have the potential to dramatically enhance chip performance, functionality, and device packing density. They may facilitate the integration of heterogeneous materials, devices, and signals. However key technology challenges of 3D ICs need to be addressed, before these advantages can be realized. Especially, the processes required to build circuits with multiple layers of active devices must be compatible with current state-of-the-art silicon processing technology.

Even in the absence of continuous device scaling, 3D integration has the potential of providing advanced performances, as each transistor in a 3D IC can access a greater number of nearest neighbors and each circuit functional block has higher bandwidth. 3D integration of devices offers the following benefits:

- **Power:** 3D integration provides a smaller wire-length distribution. Shorter wires decrease the average load capacitance and resistance thereby decreasing the number of repeaters that is needed for long wires. Hence, the active power is reduced by 10% while wire efficiency is increased by 15% compared to 2d integration[174] ,where interconnecting wires with supporting repeaters consume a significant portion of the total power.

- **Noise:** Shorter wires will have lower wire-to-wire capacitance and the reduced number of repeaters should provide less noise and less jetter, offering better signal integrity.
- **Logical Span:** Since 3D IC provides a lower wiring load, it makes it possible to drive a greater number of logic gates, which otherwise is significantly constrained by external load capacitance[175].
- **Density:** Since circuit components can be stacked on top of each other, chip's footprint can be reduced while increasing the device density. This reduced volume and/or weight of a chip is of great interest especially for wireless, portable electronics and military applications.
- **Performance:** 3D technology enables memory arrays to be placed above or under logic circuitry resulting in an increased bandwidth and thus significant performance gain in communication between memory and microprocessor.
- **Functionality:** 3D integration will allow incorporation of new elements and enable the implementation of related design flexibility including new system architecture that is currently prohibited by planar technology.

Current technology for making 3D interconnection either involves chip stacking, where bare dies are secured using epoxy to full chips and electrical connections are created using wire bonding techniques, or wafer scale fabrication. Wafer scale fabrication can again be either bottom-up or top-down. Bottom-up wafer scale fabrication involves creation of bottom-most layer using standard CMOS technology followed by formation of a second Si layer and device formation on the second layer. Subsequent layers can be formed in the same way as long as it is within thermal constraints. In top-down wafer scale fabrication multiple

2D IC circuits can be fabricated in parallel and then assembled to form 3D IC. These techniques use vias in the chip itself for connection. The vias are usually filled with copper.

Unfortunately as copper components get smaller, their resistance to the flow of electricity increases. Another problem with today's copper conductors is that one has to create deep, narrow trenches on silicon wafers in which to bury them. This presents an increasingly difficult manufacturing challenge while making smaller and smaller components. Hence makes it harder to shrink devices. Furthermore Cu interconnects require barrier and seed layers. By contrast, CNTs can carry much higher current due to their robustness. This property, in addition to their infinitely small size, opens the door for smaller chip configurations. The ITRS roadmap has included carbon nantubes as future replacement of Cu vias.

However fabrication of CNT based nanoelectronic architecture requires new challenges that need to be addressed such as interconnectivity, device alignment, interfacing between nano and micro regimes. This quest for nanoelectronic architecture requires new methodologies and techniques that can arrange nanotubes in proper positions and desired formations.

An approach towards this end is to make alternative three dimensional architecture that would overcome technical challenges in scaling such as patterning limitations, controllability of limited sum of electrons, and inter-cell noise. While several methods have been utilized to arrange nanotubes in desired formations and position including direct growth, magnetic[176], chemical[177] or electric field[178] assisted assembly, direct growth[179,180] has been

the only method so far to make 3D nanotube architectures. Unfortunately the direct growth method is a high temperature process requiring precise patterning of catalysts.

Utlilizing nanostructures in three dimensional architectures would significantly increase the density of Nano devices while providing a means for their integration into microdevices. 3D architecture would overcome technical challenges in scaling such as patterning limitations, controllability of limited sum of electrons, and inter-cell noise in addition to paving way for new device geometries. Developing intergrated nano-devices making use of the diverse properties of CNTs and nanowires in three dimensional architectures require techniques that assemble these building blocks in a precise, scalable and highly reproducible manner in addition to addressing technical challenges like (a) controlled placement of CNTs (b) control over their electrical properties and (c) low contact resistance. The only method that has been explored until now for the integration of nanotubes into three dimensional architectures is to grow them vertically using chemical vapor deposition (CVD). The CVD based nanotube growth process uses catalysts deposited either on a buried electrode[181,182] or directly on metal electrodes[183]. In the latter case, the inter-metallic dielectric (IMD) layer is deposited subsequent to the growth of the CNTs. CVD based approach to grow nanotubes on CMOS electronics have limitations due to high processing temperatures (>500°C) and nonselectivity to nanotube types.

In this chapter we describe a strategy that enables room temperature integration of SWNTs into a three dimensional architecture. We use a top-down photolithography approach to fabricate the 3D platform and use a bottom-up dielectrophoresis approach to assemble SWNTs in a 3D architecture. Photolithography is a high rate top down approach to define parallel arrays and dielectrophoresis is a bottom-up approach to assemble nano-building

blocks at high rate for integration into NEMS devices. We exploit the powerful characteristics of these two approaches to develop a technique to fabricate scalable and reproducible nano/micro devices based on 3D SWNT architectures. We also demonstrate the feasibility of this technique for making vertical interconnects. It has to be noted that this 3d platform is not limited SWNT based interconnects, but provides a generalized 3d platform for SWNT or other nano-building blocks for making 3D NEMS devices, nanosensors etc.

5.2 Dielectrophoresis

Dielectrophoresis is a phenomenon in which an uncharged object placed in a non-homogeneous electric field experiences a force. The electrical properties of the medium and object, the object size and shape as well as the frequency of the electric field determine the strength of the force. In the case of anisotropic objects such as nanotubes, a torque acts on the nanotubes aligning them along the electric field. A nanotube that is aligned with the field lines would move perpendicular to the field lines along the gradient. The dielectrophoretic force acting on the particle can be expressed as [19]:

$$F_{DEP} \propto \varepsilon_m ((\varepsilon_p - \varepsilon_m) / (\varepsilon_p + 2\varepsilon_m)) \nabla E^2_{rms} \quad \text{5-1}$$

where ε_p and ε_m are the dielectric constants of the nanostructures and the solvent medium, respectively and E_{rms} is the average field strength. Controlled assembly of SWNTs by AC field was first demonstrated by Yamamoto et. al.[184]. Krupke et. al.[185] and Mureau et. al.[186] recently demonstrated that it is possible to selectively assemble m-SWNTs from a solution containing m-SWNTs and semiconducting single walled carbon nanotubes (s-SWNTs) using dielectrophoresis. Their method exploits the relative difference in dielectric constant between the two types of SWNTs with respect to the solvent. Utilizing a higher

frequency results in the movement of m-SWNTs and s-SWNTs in opposite directions along the electric field gradient, thereby selectively assembling only m-SWNTs on microelectrode arrays. However to date DEP has only been used only for assembling SWNTs[187,188] on planar surfaces.

5.3 Experimental Procedure

5.3.1 Fabrication of 3D Architecture

3d microelectrodes were fabricated using standard photolithography technique.

- A 500 nm thick SiO_2 was grown thermally on top of a Si substrate.
- An optical photoresist PR 1805 was spun on top of the wafer on the brewer 100 CB photoresist baker and spinner at 4000 rpm for 60 seconds. Followed by a soft bake at 115 C for 60 seconds.
- Optically lithography is carried out to define the bottom metal.
- Cr/Au (17.5nm/150nm) was then sputter deposited on top of the SiO_2 using Material Research Corporation's DC magnetron sputter deposition system. The Cr layer was used as an adhesion layer between Au and SiO_2.
- A liftoff process is carried out in acetone to remove the additional metal.
- 0.7μm parylene layer is vapor deposited at room temperature in a SCS parylene deposition chamber.
- An optical photoresist PR 1805 was spun on top of the wafer on the brewer 100 CB photoresist baker and spinner at 4000 rpm for 60 seconds. Followed by a soft bake at 115 C for 60 seconds.
- The second mask is aligned and optically lithography is carried out to define the top metal.

- Cr/Au (17.5nm/150nm) was then sputter deposited on top of the SiO_2 using Material Research Corporation's DC magnetron sputter deposition system. The Cr layer was used as an adhesion layer between Au and SiO_2.
- A liftoff process is carried out in acetone to remove the additional metal.
- Using the second metal layer as a mask, the parylene-C layer is etched by oxygen plasma in ICP plasma therm 7900.
- The electrodes are ready for dielectrophoretic assembly of SWNTs.

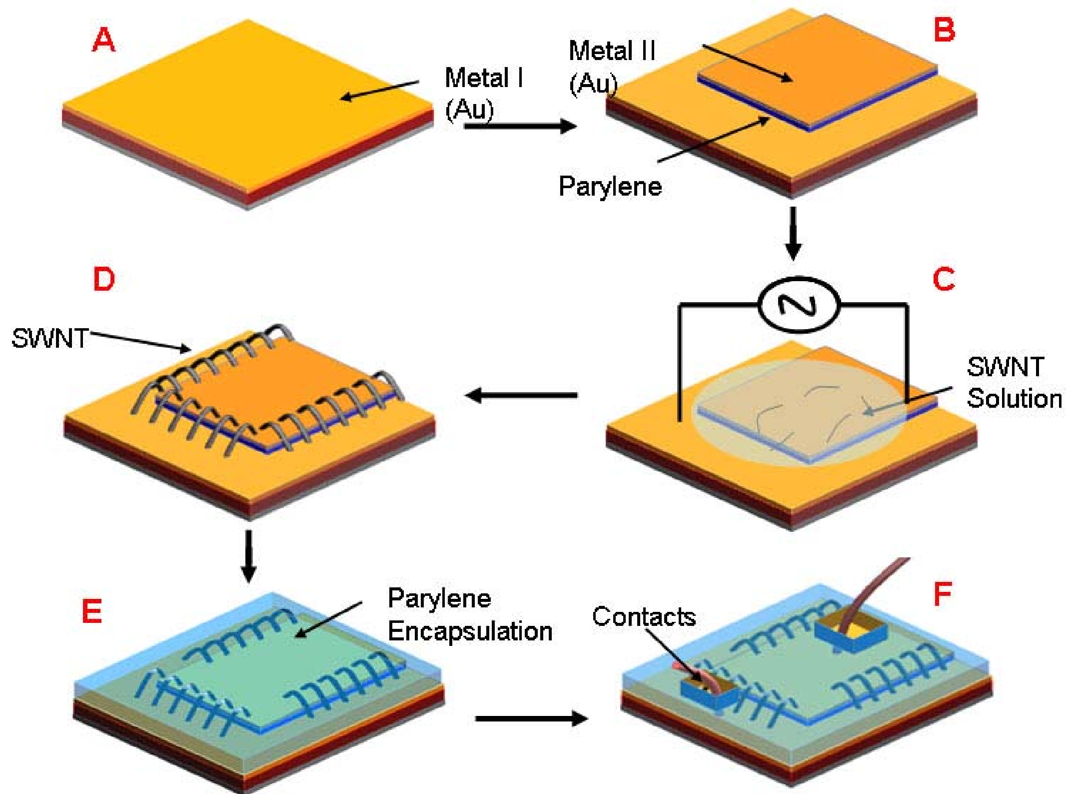

Figure 5.1: Fabrication process flow for SWNT based 3D interconnects

5.3.2 Procedure

Commercially available aqueous suspension of highly purified HIPCo-grown SWNTs with a concentration of .1 g/ml were used in our experiments. The average diameter of the SWNTs used is about 2 nm with an average length of 3 μm. The aqueous solution was further diluted to .001 g/ ml using de-ionized water and ammonium hydroxide was added to adjust the pH level to 8. The ammonium hydroxide is added in order to stabilize the pH, while still maintaining a low conductivity value. Low conductivity is desirable as it enhances the DEP effect[189]. All assembly experiments were conducted at a frequency of 10 MHz[190], while the AC voltage between the top electrode and the bottom electrode was varied from 1 to 10 Vpp. First the power supply is turned on and 2- 3 micro-liter of the SWNT suspension was placed over the electrodes. After 30 seconds of assembly, the solution was blow dried with 5 psi nitrogen. The power supply was subsequently turned off and successful assembly of SWNTs was confirmed first by continuity measurements between the electrodes and then by scanning electron microscopy (SEM) imaging. Following assembly we encapsulated the 3D SWNT architecture with a parylene-C layer. A third mask is then used to open contacts on the top parylene layer to enable electrical measurements.

5.4 Results and Discussion

SEM images of the assembled SWNTs are shown in figure 2. Well organized, parallel arrays of SWNT bundles are assembled between the top and the bottom electrodes. Figure 2(a) is an oblique SEM image of the selectively assembled SWNTs architecture. The images shows that all SWNTs assembled (figure 2(b)) are inclined at a specific angle to the surface. The experiments were also performed on multiple electrode structures connected to each other. The SEM micrographs show that the density of SWNTs assembled is uniformly

distributed on all the fingers (figure 3) demonstrating the scalability of our assembly technique. It has to be noted that the assembly takes place only on regions where the top electrode overlaps with the bottom electrode. The distribution of the SWNTs along the circumference of the top electrode is very uniform.

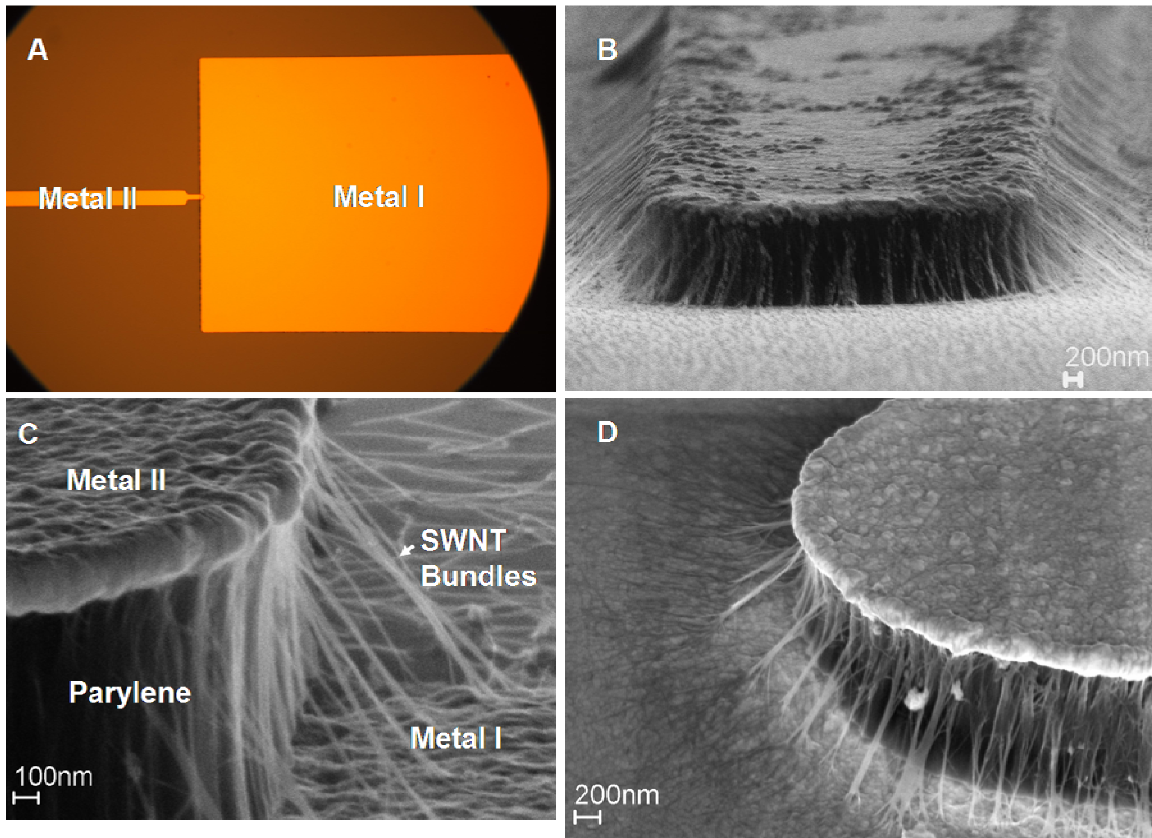

Figure 5.2: FESEM image of SWNTs assembled between the top and bottom metal. (a) An optical micrograph of the microfabricated platform (b) A high angle frontal SEM image of the SWNTs assembled at 10 Vpp connecting the top and bottom metals (c) A high resolution image of bundled SWNTs assembled at 5 Vpp. (d) Side view of the assembled SWNT architecture assembled 5 Vpp.

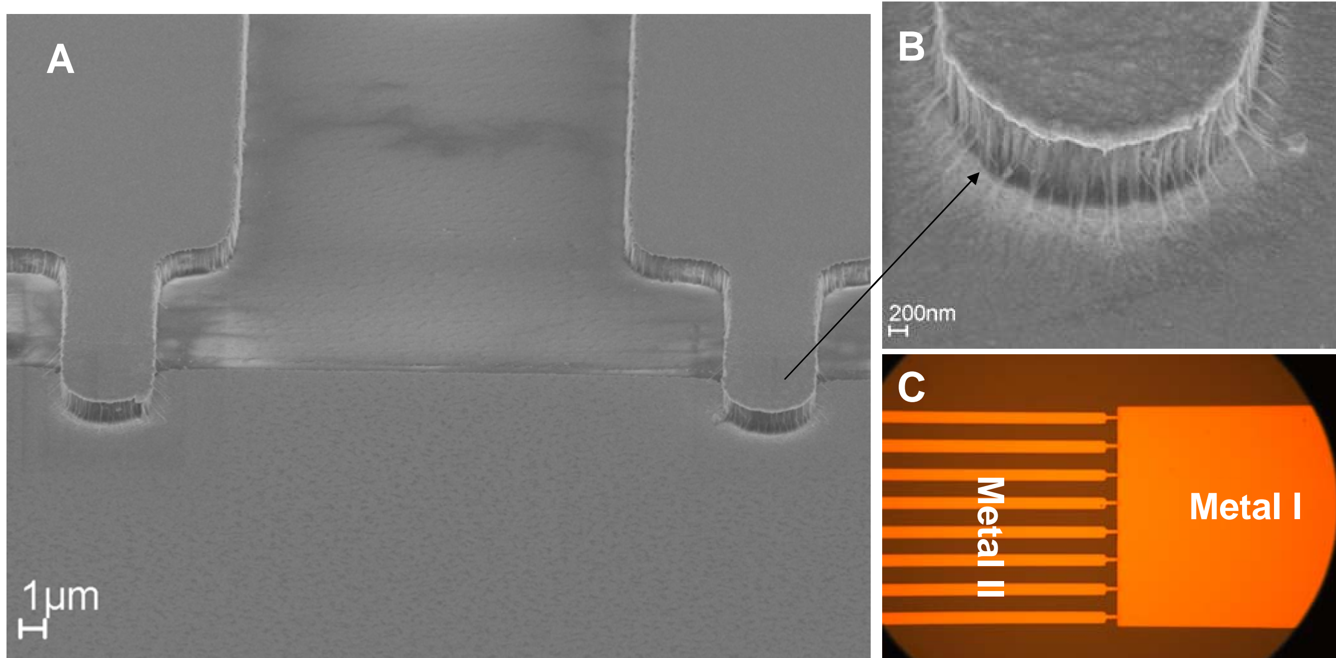

Figure 5.3: 3D assembly of SWNTs on multiple electrodes structure.(B) A close up SEM image of one of the fingers. (C) An optical image showing the microfabricated platform.

The I-V characteristics (figure 4) of the assembled SWNT bundles demonstrated a linear behavior indicating the presence of an ohmic contact at the nanotube – metal interface. The I-V measurements of all our assembled SWNTs demonstrating conductive behavior could be attributed to our technique assembling predominantly m-SWNTs. We measured two-terminal resistance values as low as 545 Ω between the two electrodes when assembling using an applied voltage of 10 Vp-p. We observed a decrease in the measured resistance value of the assembled SWNTs with the increase in the amplitude of the applied peak to peak voltage. From this we can deduce that the density and bundle size of assembled SWNTs is directly proportional to the amplitude of the applied AC voltage[191,192]. . The measured resistances of our 3D SWNT interconnect are comparable to those reported[193,194] for 2D SWNT architectures. Unfortunately estimating actual resistance of SWNTs is still hampered

by contact resistances arising from probe-to-contact pad resistance, electrode-to-SWNT contact resistance and the resistance of the SWNT bundle itself. Further work is being carried out to address and reduce these individual resistances.

The 3D SWNT architecture when encapsulated with a parylene layer continued to demonstrate a linear behavior but with a lower total resistance (~380 Ω at 10 Vpp) compared to the 3D SWNT architecture without the top parylene layer. This indicates that encapsulation with a parylene layer, secures the SWNTs, leading to an enhanced nanotube-metal contact and a lower resistance. In addition, this parylene layer protects the SWNTs from the environment.

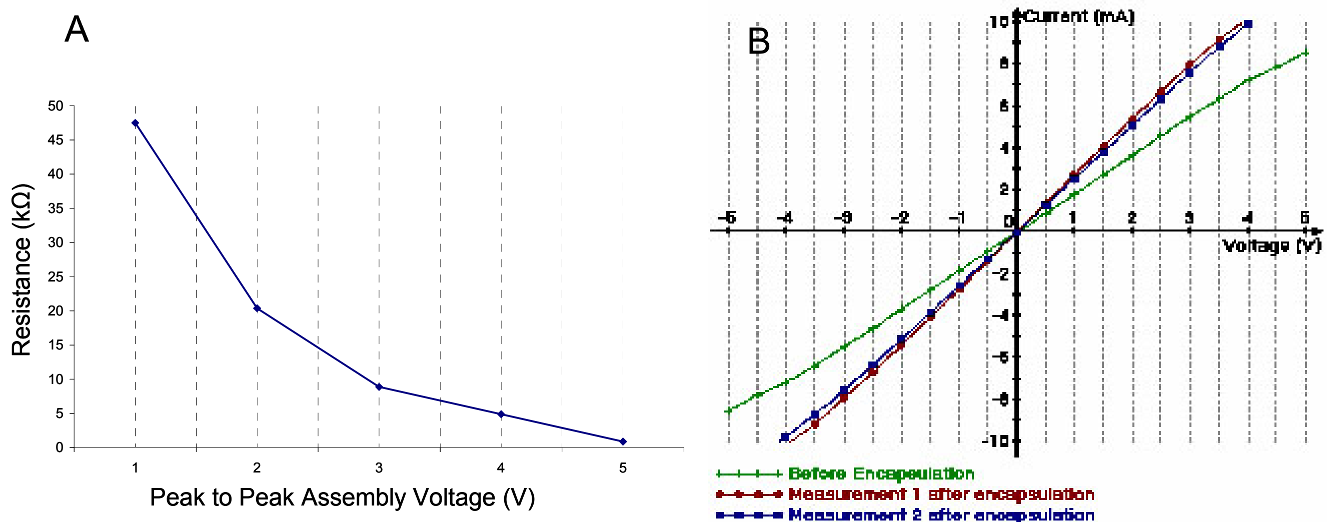

Figure 4: (A) Measured resistance of the 3D SWNT architecture assembled at different peak to peak voltages (B) I-V measurements at 10 Vp-p before and after encapsulation.

5.4.1 Assembly on Flexible Substrates

Due to the low temperature needs of the process, the technique can be used to make 3D architectures on flexible substrates too. We used a parylene substrate instead of SiO_2 and fabricated the structure as mentioned in section 5.3. The assembly of the SWNTs is shown in

figure 5. Figure 5A shows the flexible substrate with the 3D platforms fabricated on it. Figure 5B is a closer optical image of one of the 3D platforms. The assembled SWNTs after dielectrophoresis is shown in figure 5D. Well aligned parallel arrays of SWNTs are assembled between the top and the bottom electrode similar to the results obtained with the SiO_2 substrate.

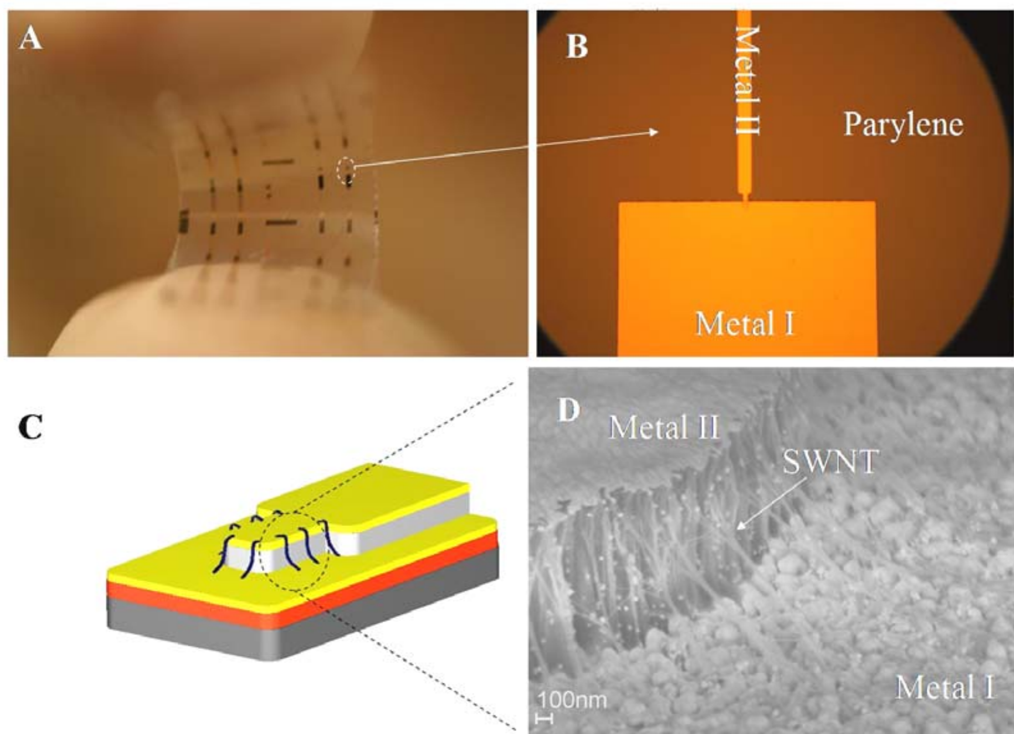

Figure 5.4: (A) Picture of the micromachined platform on flexible substrate. (B) Optical micrograph of the 3D platform. (C) Schematic of the 3D platform. (D) High resolution SEM image of the assembled SWNTs connecting the top and bottom electrode.

Electrical Measurements were carried out on the assembled SWNTs before and after flexing the parlyene substrate. The I-V measurement of the assembled SWNTs demonstrated a linear behavior with a resistance value of 900 Ω. This resistance was repeatable even after the substrate was flexed a couple of times. Even though this measured resistance value using our 3D assembly platform is lower than most of the resistance values from SWNTs

(100- 200 kΩ) reported[195, 196] to date. This resistance value would decrease as SWNT dispersion techniques mature and SWNT-metal contacts are improved.

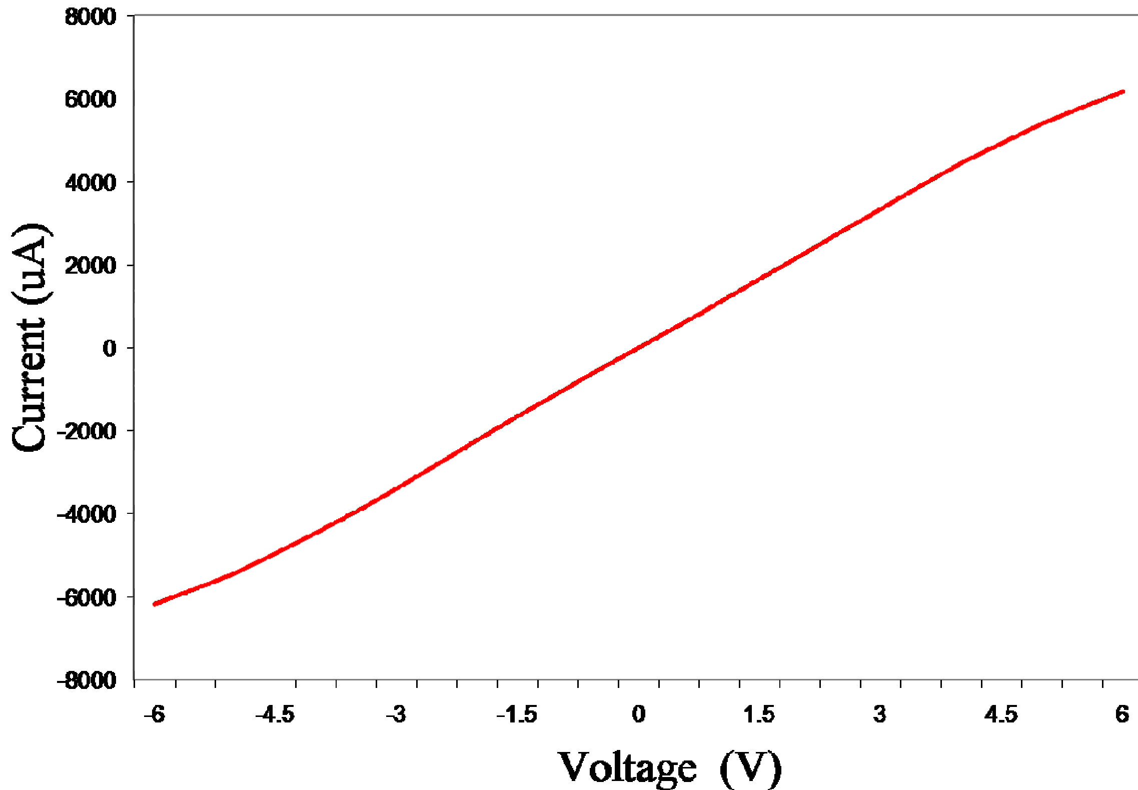

Figure 5.5: Electrical measurement showing IV characteristics of the SWNT 3D assembly.

5.5 Discussion

To gain insightful understanding of the motional and rotational behavior of the SWNTs during dielectrophoretic assembly process, we used FEMLAB multi-physics software (COMSOL) to simulate the electric field around the micro-fabricated platform and the field influence on the nanotube trapping. The electric field was simulated in both 3D and 2D for the microelectrode configuration. For simplification, here we focus on a 2D model

to explain the effect of DEP force and viscous drag on the movement and rotation of the SWNT. The geometry of the electrodes is defined based on actual fabrication details and

processes with a reasonable curvature and overhanging caused during overetching of the parylene. After assigning appropriate boundary conditions, the solution space is triangulated into a conformal mesh. The solver is then initialized to solve Laplace equation $^2\Phi = 0$, for all elements to obtain the electric potential. The electrical properties of the medium and object, the object size and shape as well as the frequency of the electric field, determines the strength of the dielectrophoretic force. The dielectrophoretic force acting on the nanotube strongly depends on the configuration of the geometry and can be calculated using the following expression.[197,198]

$$F_{dep} = \frac{\pi}{6} r^2 l \varepsilon_m \operatorname{Re}\{K(\omega)\} \nabla E_{rms}^2 \qquad 5\text{-}2$$

Where $K(\omega) = \left(\frac{\varepsilon_p^* - \varepsilon_m^*}{\varepsilon_m^*} \right)$, ε_p^* and ε_m^* are the complex permittivity of the rod-like particle and the suspending medium, respectively. Here $\varepsilon^* = \varepsilon - i(\sigma / \omega)$, where $i = \sqrt{-1}$, ε is the real permittivity and σ is the conductivity of the material. ε is a material property and can be written as a product of the relative permittivity of the material and permittivity of free space ε_0. The value of real permittivity ε for SWNTs varies from unity to infinity depending on whether the tube is metallic or semiconducting[199, 200, 201]. The conductivity of the semiconducting SWNT (s-SWNT) and metallic SWNT (m-SWNT) is reported in the literature to be 10^5 Sm^{-1} and 10^8 Sm^{-1} respectively[202,203,204]. The buffer solution is DI water based and the conductivity is controlled by adding ammonia. As a result, the medium dielectric property and conductivity is 80 and 40 μS, respectively. With these conditions our calculations revealed that a single s-SWNT experiences a negative DEP force while a single m-SWNT experiences a positive DEP force.

To theoretically determine the trajectories of the nanotubes is difficult because of the

electroorientation caused by the torque on the rod-lie objects. Such a torque acting on a nanotube can be calculated as:[205,206]

$$T = 4\pi r^2 l \varepsilon_m \operatorname{Re}\left(\frac{(\varepsilon_p^* - \varepsilon_m^*)^2}{\varepsilon_m^*(\varepsilon_p^* + \varepsilon_m^*)}\right) E_{rms}^2 \sin\theta \qquad 5\text{-}3$$

A previously described 3D model has simulated the nanotube trajectories by considering the flow and thermal effect,[198] however, the actual rotation of the nanotube is not included to accurately represent the complex behavior in a multi-physics environment. Also, the real-time response of nanoscale objects to an externally applied field is rarely studied due to the difficulty in theoretically describing relevant forces in simple forms and solving the equations.

The actual nanotube behavior under different forces and torques is complex. One has to consider the trajectories of the barycenter of a nanotube and the ration at the same time. In a finite element calculation, we can easily address such a problem by assuming the other factors as constant in a small time step. As a first step, we have developed simple and effective ways to simulate the trajectories of rod-like particles in a very short time domain. The following equations can be used to describe such transport behaviors.

$$m_o \cdot x_o'' = F(t, x_o, x_o') \qquad \mathbf{5\text{-}4}$$

where m_o represents the mass of an nanoscale object, x_o is the object coordinate in a 2-D plane, x_o' is the velocity of the object, and x_o'' is the acceleration of the object. A simplified model without considering the effect due to nanotube rotation is developed and the result is shown in figure 5. In the real situation, the torque rotates the SWNT to align its long axis along the electric field as the nanotubes move through the solution following the predicted

trajectory. A more practical model by coupling the ration effect is currently being studied to yield a better understanding of the presented assembly process.

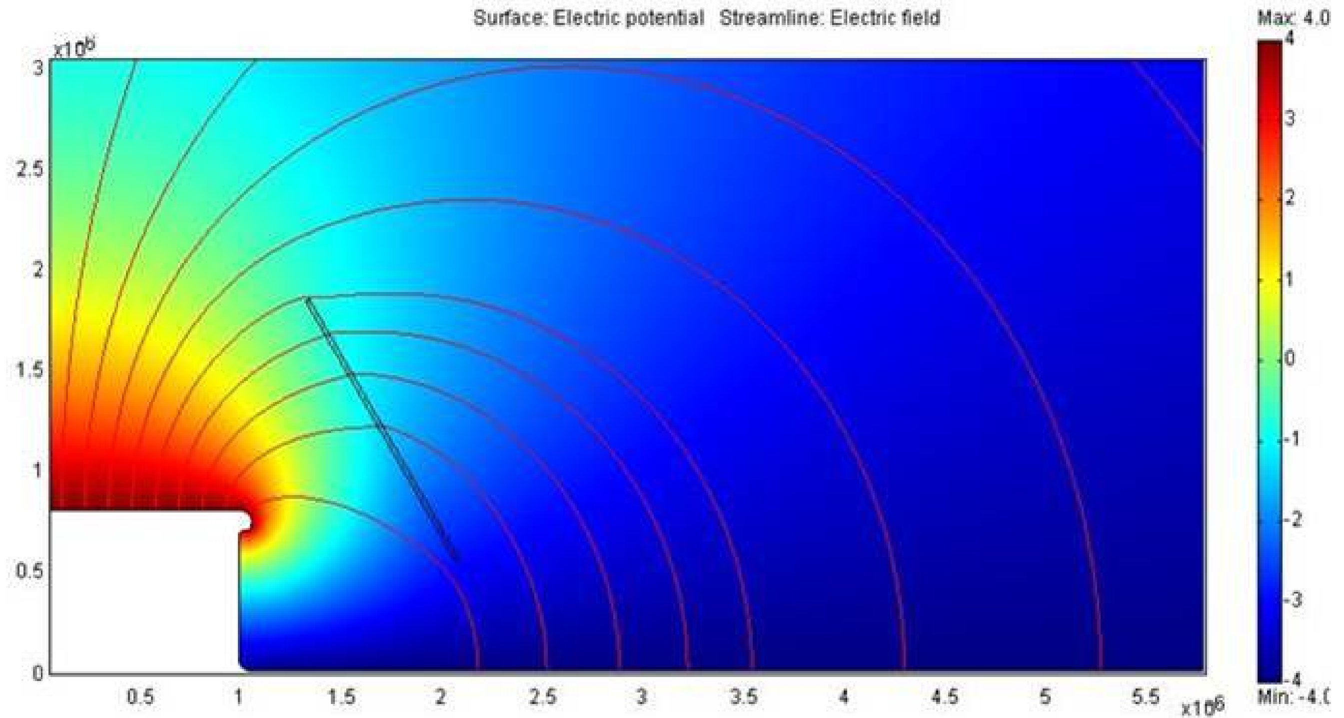

Figure 5.6: Finite element modeling of the dielectrophoresis process showing the electric field lines and a SWNT.

5.6 Conclusion and Future Work

In conclusion, we have developed a versatile low temperature technique that utilizes an hybrid approach combining micro-fabrication and dielectrophoresis to make SWNT based three dimensional interconnects. The two-terminal resistance of this 3D SWNT architecture resulted in a low resistance comparable to those reported for 2D SWNT architectures. To the best of our knowledge, these are the earliest reported results in the controlled fabrication of

3D architectures of SWNTs using a room temperature dielectrophoresis approach. We have used a parylene layer to encapsulate the SWNT bridge to protect it from the environment. Encapsulating the SWNT bridge with a parylene layer also improved the SWNT-metal contact resistance. This ability to integrate carbon nanotubes in a three-dimensional structure using a low temperature process without a catalyst would be a significant contribution to microelectronics and nanotechnology. This technique can be extended to multi-walled carbon nanotubes (MWNTs) and nanowires with direct applications in 3D interconnects, 3D nano-electromechanical systems, and for in-line characterization of manufactured nanomaterials.

6 Chapter 6: Summary and Future Work

In this thesis we describe new approaches towards integrated nanosystems by bottom-up assembly techniques using Single walled carbon nanotubes as the building blocks. All approaches involve the use of electric field to drive the SWNTs towards a prefabricated template.

The first two approaches involve the use of electrophoresis to drive the SWNTs on to prefabricated templates. Both approaches rely on the negative charge due to the presence of carboxylic groups present predominantly at the two open ends of the nanotubes. Once assembled either additional fabrication steps can be used to make the devices or the assembled SWNTs can be transferred onto a device substrate.

In the first approach SWNTs were assembled onto an interdigitated array of microfabricated electrodes. The SWNTs selectively assembled only on the positive electrode for all values of pH ranging from 4 to 10. Since it was not possible to measure the zeta potential of SWNTs with the current equipment capabilities, this method also enabled in analytical estimating the charge on the SWNTs. There was no control on the directionality of the assembled SWNTs while using micron sized electrodes. When nanosized electrodes were used to provide the required directionality, the SWNTs assembled only on the micropads connected to the nanoelectrodes. Computational fluidic model showed that when a microelectrode is placed near a nano-electrode, most of the SWNTs assembled on the microelectrodes, due to the intensity of the electric field being very high at the microelectrodes. Further IV measurements of the nano-electrodes showed that their resistance is three orders of magnitude higher than that of bulk gold. These problems along

with the degradation of gold and fabrication issues with the nanowires prompted finding an alternative approach.

The second approach used trenches created on polymer as the template for the assembly. The template consisted of PMMA deposited on a gold substrate. When the template along with a counter electrode was placed in a solution and a bias was applied. The SWNTs migrated towards the positive electrode and assembled inside these trenches. Following assembly the substrate was withdrawn using a dip coater. Both experimental as well as theoretical calculations revealed that the electric field helps in assembling the SWNTs while the capillary forces during the withdrawal of the substrate provide the required alignment. Thus by employing both electrophoresis and dip coating, SWNTs suspended in solution can be assembled on prefabricated structures with precise alignment and control over large areas within a short period of time. It is also shown that the direction of substrate withdrawal significantly affects the alignment and orientation of directed assembly of SWNT bundles.

We have also successfully fabricated SWNT interconnects and FETs using the assembly technique developed. These devices can be fabricated by carrying simple additional fabrication steps. Both devices showed performances comparable to previously produced results for similar SWNT devices. This technique is chemistry free, short time period, scalable and can be easily integrated with the current CMOS fabrication process.

The third approach adopts a hybrid technique combining both bottom-up dielectrophoresis and top-down microfabrication techniques to enable room temperature integration of SWNTs into three-dimensional architectures. The two-terminal resistance of this 3D SWNT architecture resulted in a low resistance comparable to those reported for 2D

SWNT architectures. Encapsulating the SWNT bridge with a parylene layer in addition to providing protection from the environment also improved the SWNT–metal contact resistance. This ability to integrate carbon nanotubes in a three-dimensional structure using a room temperature process without a catalyst would be of significant value to nanoelectronics. This technique can be extended to multi-walled carbon nanotubes (MWNTs) and nanowires with direct applications in 3D interconnects, 3D nano-electromechanical systems, and for inline characterization of manufactured nanomaterials.

6.1 Future Work

Eventhough we have successfully demonstrated large scale assembly technique for SWNTs along with some device concepts. There are still plenty of studies that can be carried out to make this process more robust. Listed below are some research topics that will be useful in extending the present work.

1. In the case of the interdigitated electrodes better electrode designs, like embedding the metal wires into oxide layers by a combination of lithographic and chemical polishing steps can help in avoiding the metal degradation and directing the SWNTs onto the nanowires.
2. All experiments used ammonium hydroxide to induce ions in the SWNT solution. Some experiments also used Sodium hydroxide. Additionally it would be interesting to study how different bases and acids affect the dispersion as well as assembly of SWNTs.
3. The insulating layer used for the assembly of SWNTs into trenches was PMMA. Additionally PR- 1805 and parylene was used for large scale patterns. Since surface properties play a key role in the directed assembly as well as for alignment, the effect

of different polymers as well as Self-assembled Monolayers (SAMs) would help in understanding and controlling the process better.

4. The conductive substrate used for the assembly was predominantly gold. But there were some efforts to assemble on ruthenium and titanium. Future study can involve the use of different substrates like platinum and palladium. An interesting outcome of this study would be to see how the different surfaces would affect the alignment and assembly of SWNTs. In addition electrical measurements can be carried out to see which metal would yield the least contact resistance.
5. The field effect transistor fabricated in this thesis displayed an N-type behavior as opposed to the normal p-type behavior observed in SWNTs. Since device characterization was beyond the scope of the work here, it would be interesting to carry out further transistor characterization and get an insight into why the SWNTs demonstrate an N-type behavior. Some of the possible reasons include doping by potassium or the polymer (parylene).
6. Transfer of the SWNTs onto both rigid and flexible substrates need to be studied in detail. Following transfer electrical and mechanical characterizations have to be carried out to validate the success of transfer.
7. The assembled substrate provides a generalized platform for making a plethora of devices. Some of the devices that can be developed using this technique but not limited to, include bio and other sensors, field effect transistors, composites, transmission lines, interconnects, logic devices, Electromagnetic interface (EMI), field emitters, photovoltaic devices etc.

8. On the theoretical side additional fluid dynamic simulations need to be carried out to further understand the behavior of the SWNTs both in the solution as well as during assembly and alignment.
9. The 3D SWNT architecture provides a room-temperature platform for fabricating a multitude of 3D devices. Some of the devices that can be developed using this platform can include vertical interconnects, 3D transistors, sensors, field emitters etc. The parameters of the assembly as well as the dimensions could be modified to develop vertical SWNT architectures.

In conclusion the technologies developed in this study provide a generalized platform that can employ a multitude of nanostructures including nanowires, nanoparticles etc. to create a plethora of nano-based products.

Appendix A: Fabrication Materials and Method

A1. Oxidation and Standard Cleans

The foremost step in any fabrication process is the chemical cleaning of the wafers to remove particulate matter on the surface including organic, ionic and metallic contaminants. A standard pre-diffusion cleaning procedure is widely adopted in the industry and research labs. The first step is the removal of organic and metal contaminants using Piranha. Piranha is a mixture of H_2SO_4 and H_2O_2 and removes organic contaminants by oxidizing them, and metals by forming soluble complexes. The mixture is self-heating and hence the H_2O_2 has to be added very slowly. Solution looses its effectiveness when it cools down. Addition of H_2O_2 helps in spiking up the temperature of the solution. This is followed by a HCl/ H_2O_2 wash to remove heavy metals. The final step involves the removal of the 2 nm native oxide layer using a HF clean. Each of the individual chemical cleaning process is followed by a deionized (DI) water rinse step until the desired resistivity is reached. The resistivity of a typical DI water system is about 18 Mohm-cm. A standard pre-diffusion wafer cleaning procedure is listed below.

A. Removal of organic contaminants and some metals

1). 10 minutes in Piranha bath H_2SO_4:H_2O_2 (2:1) @ 90 °C

2). 5 minutes rinse in DI water

B. Heavy metal clean

1). 10 minutes in H_2O:H_2O_2: HCl (6:1:1) @ 70 °C

2). 5 minutes rinse in DI water

C. Oxide Removal

1). 5 to 15 seconds in H_2O: HF (10:1)

2). 10 minutes rinse in DI water

Table A. 1: A standard pre-diffusion clean

Oxide layers are usually deposited on top of a wafer to isolate the semi-conducting silicon wafer from the rest of the device thereby avoiding leakage and shorts. This is accomplished by thermal oxidation, where in the wafer is exposed to an oxidizing environment at elevated temperature. Oxidation can be either dry or wet. In the former a silicon wafer is exposed to atmosphere containing oxygen while in the later the wafer is exposed to atmosphere containing water vapor. Dry oxidation is denser and hence used for thin oxide layers (<100 nm), while wet oxidation is faster and more uniform. Usually the oxide growth is a combination of both wet and dry oxidation cycles to get a very uniform oxide layer in short time.

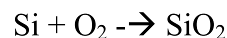

$$Si + O_2 \rightarrow SiO_2$$

$$Si + 2H_2O \rightarrow SiO_2 + 2H_2$$

A2. Metal Depostion

A2.1 Sputtering

Metal layers were deposited via a physical vapor deposition method using a DC magnetron sputtering system developed by Materials Research Corporation. This system can house 3 – 6” targets and 1 – 4” target at a time. The available metals on this system include TiW, W, Cr, Cu, Au, Al and Rh. Out of these only the Au is a 4” target and the rest are 6” targets. While all metals use a DC power source, the Au uses a RF power generator. Metals were also sputtered using a second DC magnetron system called Perkin Elmer 2400. This system can house 3- 8” targets with both RF and DC bias. The available materials on this

system are Al, Ti and Si. There is no load lock on either systems, and the whole chamber has to be vented for loading and unloading the samples. Before sputtering the metal onto the wafer, a presputtering process is generally carried out to clean the target and get a uniform deposition rate.

Sputtering involves the bombardment of a target (a disc of the material to be deposited) kept at a high negative potential, with positive argon ions. Due to momentum transfer the target material is sputtered away mainly as neutral atoms and the ejected surface atoms are deposited onto the substrate placed on the anode. Considerable heating can occur at this stage, which can be minimized by using a magnetron. In a magnetron sputtering apparatus, the crossed magnetic and electric field forcing the electrons forcing them to travel in long, helical paths, thereby increasing the probability of ionizing collision with an argon atom. Furthermore the crossed fields bend and collect at the ground shield any secondary electrons that are emitted by the cathode due to bombardment. This eliminates any unplanned substrate heating due secondary electron bombardment. Before sputter deposition, the substrate maybe sputter etched by connecting it to the negative pole of the power supply promoting adhesion of subsequent metallization. The plasma ions add energy to the film and keep the surface atoms mobile enough to fill virtually every void, thus providing a very uniform film.
Sputtering systems are more complex than evaporation systems, along with excessive heating of the substrate and slow deposition rates compared to evaporation system.

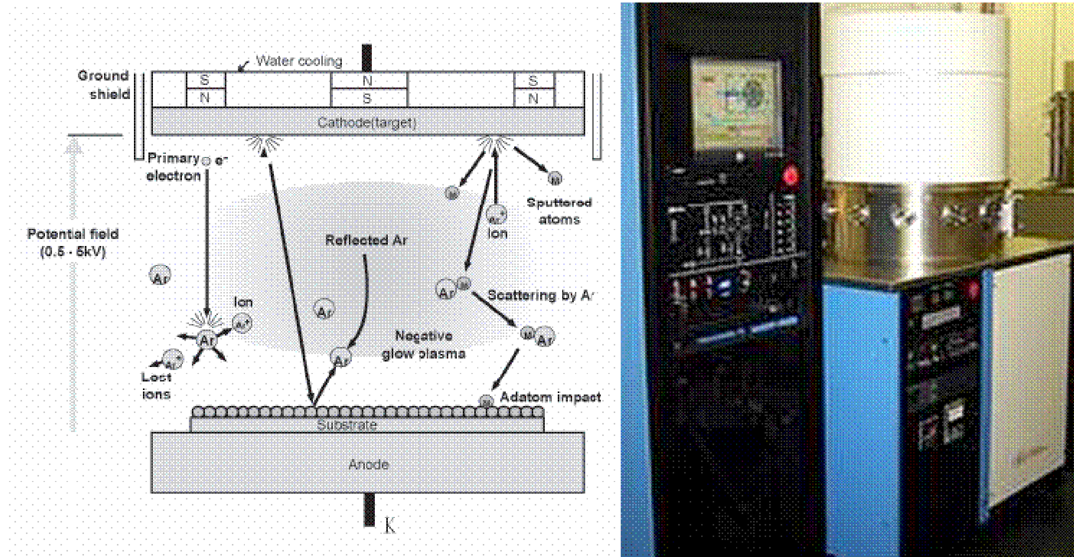

Figure A.6.1: (left) Mechanism of Sputtering (right) MRC tool at Kostas facility[207]

A2.2 Electron Beam Evaporation System

Metal layers were also depositing using an Electron beam evaporator system. It can hold one 3" wafer and has a 6cc pocket to place the metal pellets. Metals in the system include Ti, Cr, Au, Al and Ni. Similar to the sputtering system this system doesn't have a load lock and the chamber has to be completely vented.

In electron beam evaporation system the metal to be deposited is bombarded with an electron beam given by a charged tungsten filament under high vacuum. This causes the material to boil and evaporate. The atoms in gaseous phase precipitate into solid form, coating everything in the vacuum chamber with a thin layer of the material. A quartz crystal balance can be placed in the chamber to monitor the thickness of the material deposited.

The ebeam system has a higher deposition rate than sputtering systems, thousand atomic layers per sec as opposed to one atomic layer per sec. Ebeam systems are generally found in laboratory environments. Metal deposited using sputtering system was found to be better for our assembly process than ebeam evaporated metal.

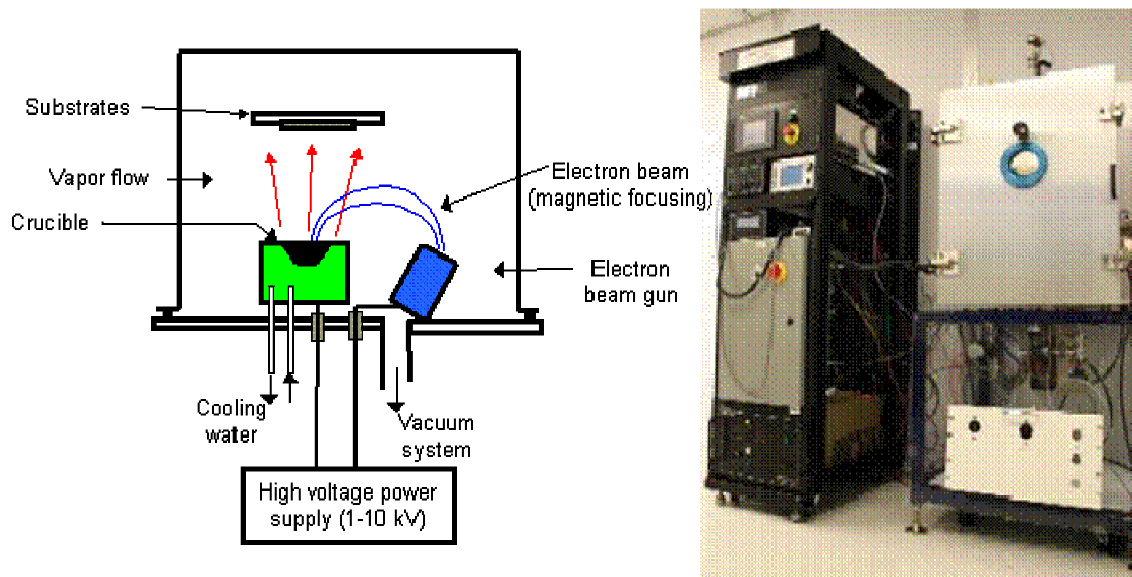

Figure A.6.2: (left) Mechanism of ebeam deposition[208] (right) Ebeam system at Kostas facility

A3. Lithography

Optical lithography was carried out using a quintel 4000- 6 mask aligner. It is a contact mask aligner that uses a laser with wavelength of to expose the resist. First the mask is placed with the pattern side down on top of the mask holder and is held by vacuum. The wafer is then loaded on to a substrate chuck. A joystick is used to align the features on the mask with the wafer. This is particularly important when using multiple lithography steps. Once aligned, the wafer is exposed for the desired time and then unloaded for development of the resist.

PHOTORESIST	EXPOSURE TIME	PRINTING OPTIONS
Shipley 1813	5 seconds	Pressure Contact
Shipley 1818	5 ~7 seconds	Pressure Contact

Table A. 2: Parameters for commonly used photoresists

To create submicron and nano featured patterns the Carl Zeiss FESEM was used. Resist coated patterns are loaded into the SEM through a load lock. With the use of software

called NPGS developed by jcnabity and a Raith beam blanker, patterns drawn on cad system are transferred onto an ebeam resist. This is done by selectively exposing areas on the resist to the electron beam. The resolution and the features are controlled by the dose and probe current. The probe current can be controlled by varying the size of the aperture used during writing.

Apperture	Probe Current (μA)
7.5	27
10	42
30	287

Table A. 3: Standard appertures and probe currents

Standard Resists

Photo resists S1805, S1813 and S1818 was used for carrying out optical lithography to make micron scaled patterns. The photo resists were developed by Shipley as part of their Microposit S1800 series[209].

Resist	Tone	Resolution	Contrast	Etch Resistance	Thickness	Shelf Life	Film Life	Sensitive To White Light
PMMA	Positive	Very High	Low	Poor	Many dilutions	Long @ RT	Long	No
P(MMA-MAA)	Positive	Low	Low	Poor	Many dilutions	Long @ RT	Long	No
NEB-31	Negative	Very High	High	Good	Several Dilutions	Long @ RT	Short	Yes
EBR-9	Positive	Low	Low	Poor	Single Dilution	Long @ RT	Long	No
ZEP	Positive	Very High	High	Good	Several Dilutions	Long @ RT	Short	Yes
UV-5	Positive	High	High	Good	Several Dilutions	Long @ RT	Short	Yes

Table A. 4: Properties of different optical and ebeam resists

A4. Etching

A4.1 Wet Etch of Metal

Gold Etchant GE-8148 from Transene Company, Inc. was used to etch the Au layer. GE-8148 contains complex KI-I_2 complex and phosphate compound as its main constituents. It is formulated to selectively etch gold. Hence doesn't affect either the negative or the positive photoresists. Etching can be readily controlled with uniform etch rates and minimum undercutting. Following etching the sample has to be rinsed with flowing DI water to remove the solution from the surface completely. The overall reaction for etching gold is given by equation. The potassium iodide increases the solubility of both the iodine and gold iodide in water, allowing a greater concentration of reactant in the solution and the etch product to be removed so that the etch can proceed.

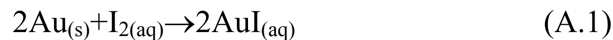

$$2Au_{(s)}+I_{2(aq)}\rightarrow 2AuI_{(aq)} \qquad (A.1)$$

Alternate gold etchant includes TFA, TFAC, GE-8110, etc. Table A.5 shows a comparison of the properties of these gold etchant. The following gives a comparison of different gold etchant[210]

<table>
<tr><th>Gold Etchants</th><th>pH @ 20 °C</th><th>Etch Rates @ 25 °C</th><th>Resist</th><th>Application</th></tr>
<tr><td>TFA</td><td></td><td>28 Å/sec</td><td rowspan="4">Negative and Positive</td><td rowspan="4">Thin Film Circuits
GaAs compatible
Ni compatible</td></tr>
<tr><td>TFAC</td><td></td><td>10 Å/sec</td></tr>
<tr><td>GE-8148</td><td>8.15 ± 0.2</td><td>50 Å/sec</td></tr>
<tr><td>GE-8110</td><td>7.9 ± 0.1</td><td>15 Å/sec</td></tr>
</table>

Table A. 5: Comparison of diferent gold etchants

Chromium mask etchant from Transene was used to etch the Cr layer. Chromium Mask Etchant permits precise etching of chromium. This particular etchant is relatively non-

toxic and non-hazardous to use, compared to conventional dangerous laboratory etchants in the mask making process. Similar to the gold etchant, this is room-temperature operated, offers excellent visual etch control and is compatible with both positive and negative photoresist materials. Fine line definition and geometrics are registered and held to tolerances in the sub-micron range. Table A.6 shows a comparison of the properties of different Chromium etchants.

Chromium Etchants	Etch Rates	Resist	Application
CHROMIUM ETCHANT 1020	40 Å/sec @ 40 °C	Negative and Positive	Thin Film Circuits
CHROMIUM ETCHANT 1020 AC	32 Å/sec @ 40 °C		
CHROMIUM MASK ETCHANT	800 Å/sec@ 25 °C		
CHROMIUM ETCHANT CRE-473	14 Å/sec@ 25 °C		

Table A. 6: Comparison of different chromium etchant[211]

A5. Dry Etching of Metals

A5.1 Ion Beam Milling

Ion beam milling is a physical etching process in which argon or other inert gas ions are extracted from a glow discharge region are accelerated in an electrical field toward the substrate, and etching happens by physical impact of the ions. This process is inherently nonselective, as there are no chemistry involved and ion energies are large compared to the differences in surface bond energies and chemical reactivities. Ion milling is a slower etch technique, with etch rates limited to several hundreds of angstroms per minute as opposed to thousands of angstroms per minute achieved by chemical etching processes.

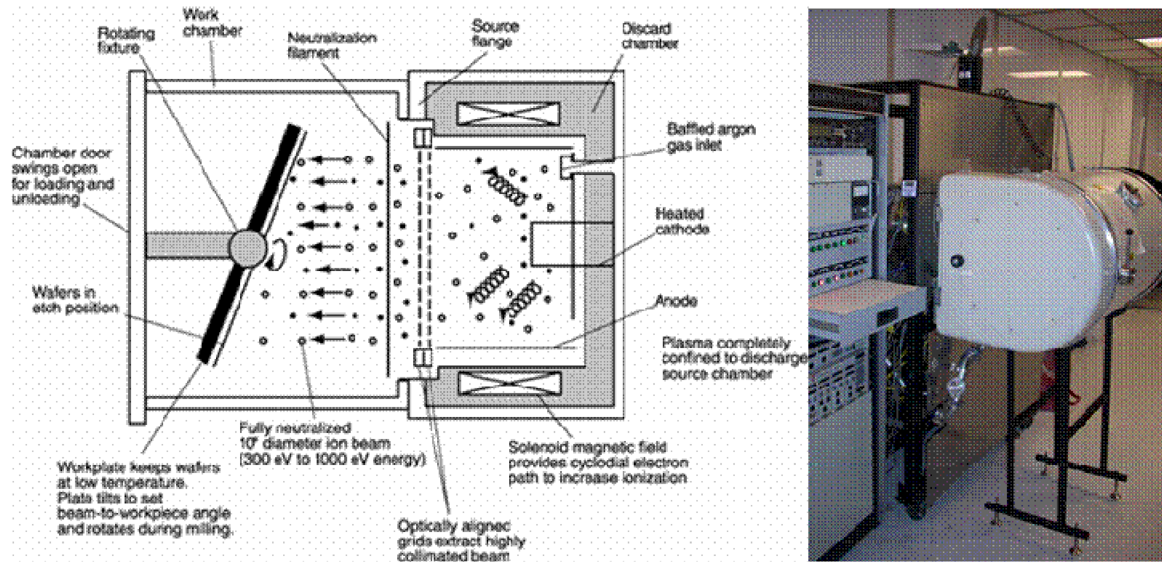

Figure A. 6.3 (left) Mechanism of Ion Beam Milling[212] (right) Veeco Microetch ion mill at Kostas facility.

Veeco Microetch ion mill was used to etch the Cr/Au layer for making the microfinger electrodes. The ion mill uses a 12 cm DC style gridded ion source for physical sputter etch removal of material from the substrate. The substrates are water cooled. The angle of incidence can be adjusted to get the desired effect and etch rate. The substrate can rotate in order to obtain uniform etching. Since ion milling is non-selective it is advisable to use a thick photoresist in order to avoid completely etching the resist. In our case we use PR - 1818. There is an option to etch 15 cm x 15 cm chips by using a metal plate to mask the remaining area. 5 wafers can be etched at one time. Ion-milling provides a much better profile of the etched electrodes as compared to wet etching because of high anisotropy and is easier to control. But the masking PR gets charred after etching due to the heat. Hence the wafer has to be left in piranha or 1165 bath for an hour to completely remove the remaining photoresist.

ION BEAM ETCH RATE DATA

ETCH RATES FOR 500 EV ARGON IONS AT 1 MA/CM²

Target Material	Angstroms / Minute	Target Material	Angstroms / Minute
Ag	1833	Sb	3238
Al	630	Si	310
Au	1553	Sm	990
Be	159	Sn	1217
Bi	8798	Ta	380
C	40	Th	740
Co	510	Ti	336
Cr	530	U	660
Cu	818	V	337
Dy	1040	W	340
Er	881	Y	837
Fe	429	Zr	570
Gd	1027		
Ge	900	Al_2O_3	129
Hf	590	Az 1350 (photoresist)	231
Ir	540	$Bi_{12}GeO_{20}$	1290
Mn	874	Cds (1010)	2100
Mo	421	GaAs (110)	1500
Nb	390	GaP (111)	1400
Ni	570	GaSb (111)	1700
Os	440	Hg:Cd:Te	2500
Pb	3073	InSb (unknown)	1300
Pd	1150	$LiNbO_3$ (Y-cut)	400
Pt	792	PbSe	1200
Rb	4000	PbTe (111)	3300
Re	470	Permalloy	470
Rh	650	SiC (0001)	320
Ru	580	SiO_2	400

All rates are for normal ion incidence.

Table A. 7: Source- iontech inc

A5.2 Plasma Etching

In reactive plasma etching, reactive neutral chemical species such as Cl or Fl atoms and molecular species are generated in the plasma diffuse to the substrate where they form voltatile products with the layer to be removed. It is a combination of both physical as well as

chemical etching processes. While the ionic species result in directional etching, the chemical reactive species results in high selectivity. By controlling the ratio of the physical/chemical etching, the rate of anisotropy and selectivity can be controlled. The role of the plasma is to supply reactive etchant species. Electric field is applied across two electrodes alternatively at radio frequency. A voltage bias develops between the plasma and the substrate due to the difference in mobilities of electrons and ions. This accelerates the ions towards the substrate. While the chemical species react with the substrate , the ions physically bombard the surface to provide the desired etch.

Inductively coupled plasma -reactive ion etcher was used in our fabrication process. The dry plasma etch reactor uses Ar/SF6/O2 gases to etch through a chemical reaction / bombardment of substrate material. The System is set for 4" wafers with He backside cooling. But chips smaller than 4” can be used too. The ICP was used predominantly for etching polymers. This involved the use of polymer.

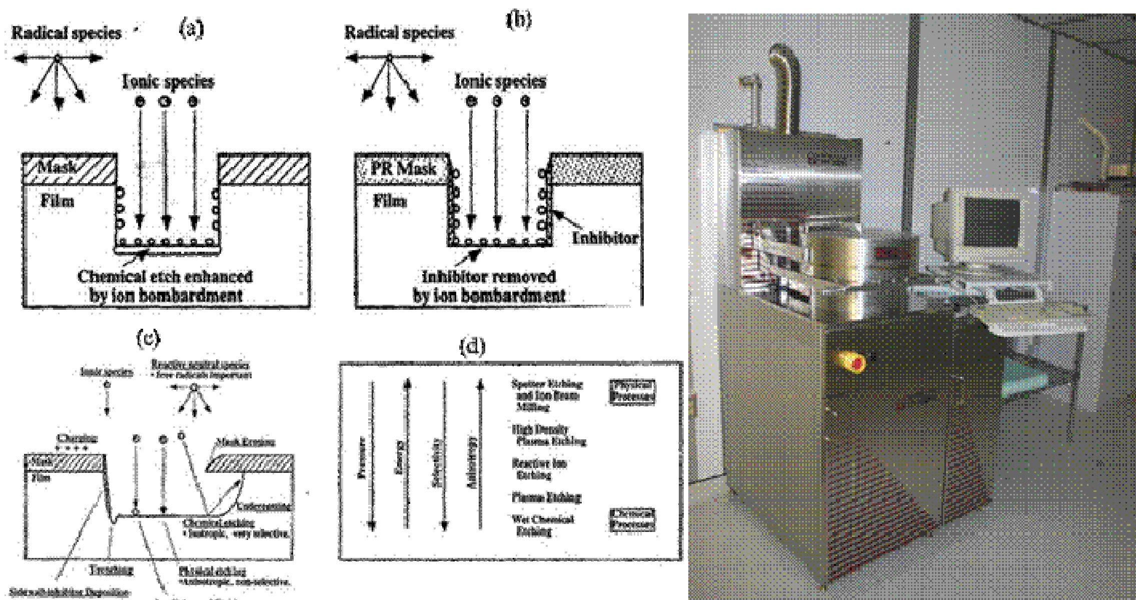

Figure A.6.4: (left) Mechanism of plasma etching (right) ICP plasmatherm at Kostas facility

Appendix B: Characterization Tools and Techniques

B1. Imaging

B1.1 Scanning Electron Microscope

Scanning electron Microscope was used for both imaging as well as for electron beam lithography to make sub-micron and nano scaled patterns. SEM is a microscopy technique that can be used for obtaining very high-resolution images. A typical SEM consists of electrons emitted from a thermionic source such as a tungsten or lanthanum hexaboride cathode and accelerated towards the anode. The SEM used here is a cold field emission SUPRA 25 made by Carl Zeiss. In a FESEM no heating of the cathode is necessary and something called a cold source is used. An extremely sharp and thin tungsten needle (10^{-7} – 10^{-8} m) is used as a cathode in front of a primary and secondary anode. The voltage between the cathode and anode is in the order of 0.5 to 30 KV. The electrons beam is focused using one or two condenser lenses. The beam passes through pairs of scanning coils or pairs of deflector plates in the electron optical column, typically in the ojective lens. These objective lens deflect the beam horizontally and vertically so that it scans in a raster fashion over a rectangular area of the sample surface. Upon interaction of the primary electron beam with the sample, the electrons lose energy by repeated scattering and absorption within a teardrop-shaped volume of the specimen known as the interaction volume, which extends from less than 100 nm to around 5 µm into the surface. This energy exchange between the beam and sample results in the emission of electrons and electromagnetic radiation which can be detected to produce an image.

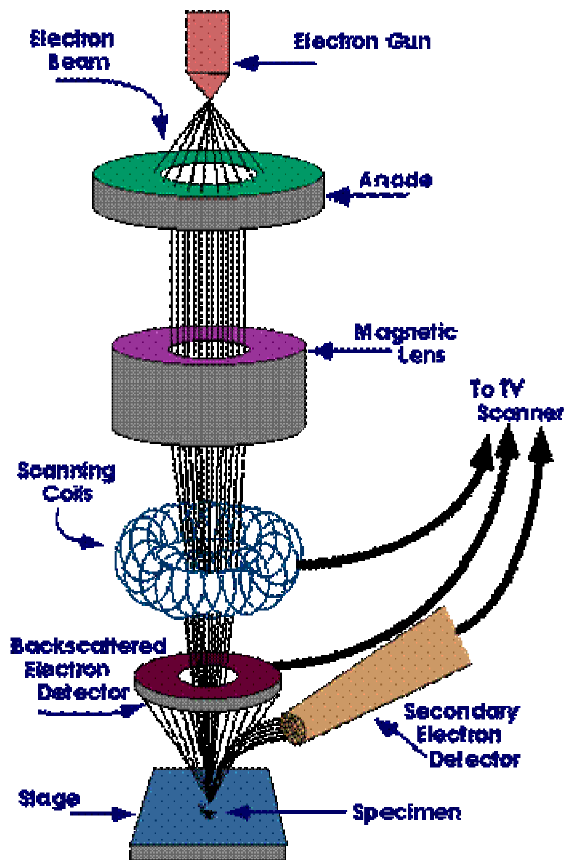

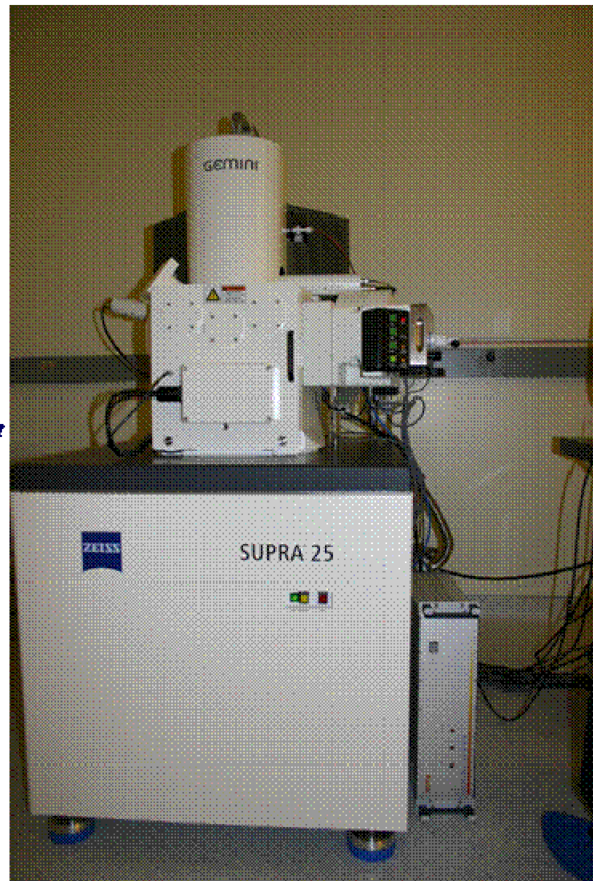

Figure B. 1: (left) Schematic of an SEM system (right) Zeiss Supra 25 at Kostas facility.

B1.2 Atomic Force Microscopy

The atomic force microscope or scanning force microscope (SFM) is a technique to obtain very high-resolution based on the scanning probe microscopy technique. A clear advantage of an AFM over an SEM is its ability to generate three dimensional images of the topography. Unlike traditional microscopes, scanning-probe systems do not use lenses, the information is gather by "feeling" the surface with a mechanical probe. Hence the size of the probe rather than the diffraction affects the resolution of the AFM. AFM operates by measuring the attractive or the repulsive forces between a tip and the sample[213]. When the tip is brought into proximity of a sample surface, forces between the tip

and the sample lead to a deflection of the cantilever according to Hooke's law. Usually the deflection is measured using a laser spot reflected from the top of the cantilever into an array of photodiodes. The cantilever is typically silicon or silicon carbide with a tip radius of curvature on the order of nanometers. There is generally a feedback mechanism employed to adjust the tip-to-sample distance to maintain a constant force between the tip and the sample, and to avoid the risk of the tip colliding with the surface. The AFM can operate in a number of modes depending on the application. In static mode, the static tip deflection is used as a feedback signal. Due to strong attractive forces and noise and drift issues the static mode AFM is always done in contact. In the dynamic mode, the cantilever is allowed to oscillate at or close to its resonance frequency. The tip-sample interaction forces modify the oscillation amplitude, phase and resonance frequency. The dynamic mode operation could be either frequency modulated or amplitude modulated.

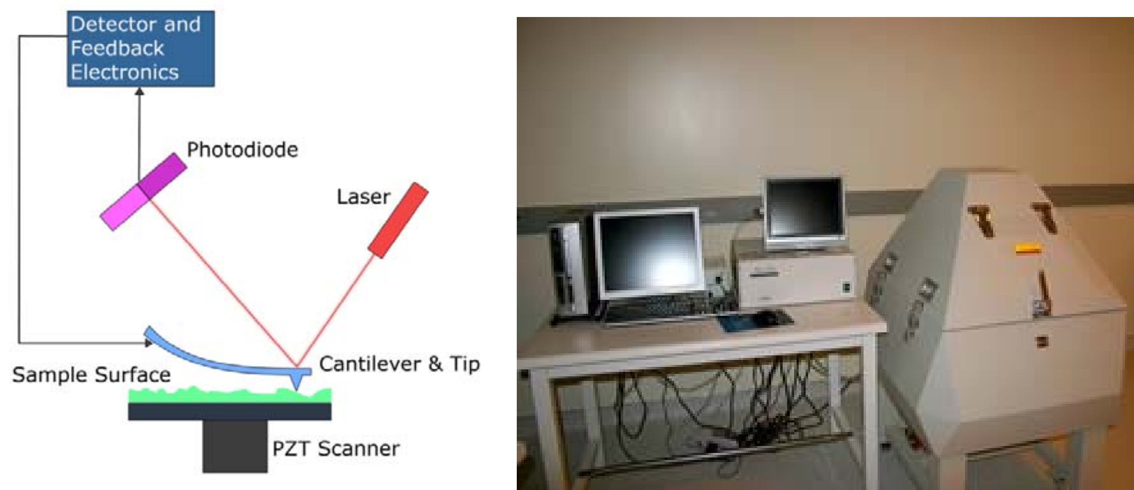

Figure B. 2: (left) Mechanism of the working of the AFM (right) PSIA XE-150 at the kostas facility

An XE-150 developed by PSIA is used to image the nanotube assembly. The Z scanner of the XE system has a resonance frequency significantly higher than those of conventional piezoelectric tube scanners resulting in greater feedback performance and more

accurate data acquisition. The cross talk between the x-y and z axes are eliminated by separating the z-scanner from the x-y scanner thereby providing distortion free scan. The sample is loaded onto the AFM using magnetic mounts. An acoustic enclosure is provided to shield the XE head from external acoustic and optical noise. Once the sample is inside the acoustic enclosure, a high quality optical microscope fitted with a CCD camera can be used to locate the specific area to be imaged. The stage is controlled by computer connected to the AFM. A manual approach is used to bring the sample in close proximity to the tip. Once the sample is in close proximity, an automatic approach is used to engage the tip and scan the surface. All carbon nanotube imaging was carried out using a non-contact method.

B2. Contact Angle Measurements214,215,216

Contact angle is a quantitative measure of the wetability of a surface. Geometrically it is defined as the angle formed by a liquid at the three phase boundary where a liquid, gas and solid intersect. The contact angle is specific for a particular surface and is determined by the interactions across the three interfaces. The Young-Laplace equation determines the shape of the droplet and is given by the following relation. Usually contact angles are measured using device called a contact angle goniometer. The contact angle is determined by the surface energy of the material that is being measured. When a liquid drop is placed on a solid surface, if the liquid is very strongly attracted to the solid surface (for example water on a strongly hydrophilic solid) the droplet will completely spread out on the solid surface and the contact angle will be close to 0°. Less strongly hydrophilic solids will exhibit contact angles of 0° to 30°. Hydrophobic surfaces usually demonstrate a contact angle that is larger than 90° and could be as high as 150° or even nearly 180°. These superhydrophobic surfaces where water

droplet just rests without wetting them can be obtained on fluorinated surfaces (Teflon-like coatings) that have been appropriately micropatterned. Hence the contact angle directly provides information on the interaction energy between the surface and the liquid. There are different techniques that can be used to measure the contact angle of a substrate.

- The static sessile drop method
- The dynamic sessile drop method
- Dynamic Wilhelmy method
- Single-fiber Wilhelmy method
- Powder contact angle method

We use a Pheonix 150 system made by SEO (Surface Electro Optics Co. Ltd.) for measuring the contact angle of our surfaces. It is a manual system and the fluid is dispensed from a manually controlled syringe. The equipment is also capable of carrying out surface energy measurements, pendant drop and contact angle calculations automatically. All contact angles measured were done in the static mode. Using this instrument we measured the contact angle of PMMA to be 65^0 and that of gold to be about 30^0.

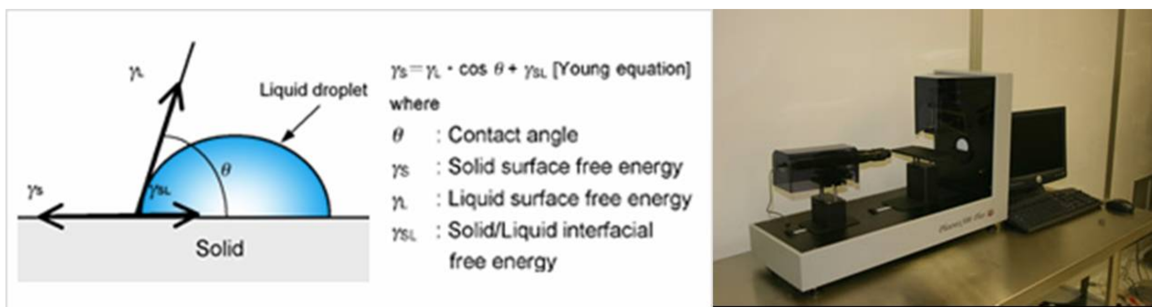

Figure B. 3: (left) Schematic describing the contact angle measurement (right) Pheonix 150 at Kostas facility.

B3. Raman Spectroscopy

Raman Spectroscopy is a widely used tool for the characterization of material composition, sample temperature and strain from analysis of the material specific phonon mode energies[217]. The advantage of this method is that it requires very little sample preparation and is a rapid, non-destructive optical technique.

It relies on inelastic scattering, or Raman scattering of monochromatic light, usually from a laser in the visible, near infrared, or near ultraviolet range. The incoming light interacts with an electron resulting in real or virtual transition of the electron to a higher energy state, where the electron interacts with a phonon (via electron-phonon coupling) before transiting back to the electronic ground state. If the molecules are excited from the ground state to a virtual energy state, their relaxation into a vibrational excited state will generate Stokes Raman scattering. If the molecule is already in an elevated vibrational energy state, the Raman scattering is then called anti-stokes Raman scattering. The choice of laser energy doesn't affect the Raman shift, but if the laser energy is in resonance with an electronic transition, the Raman intensity can be increased by many orders of magnitude. In a one-dimensional system like carbon nanotubes where the density of states is strongly peaked, resonance Raman scattering from nanotubes dominates over non-resonant contributions. Hence gives information of the vibrational mode from the Raman shift as well as of the optical transition energy.

In CNTs the most prominent Raman active peaks are the low frequency radial breathing modes (RBM) and the higher frequency, D, G and G' modes. The RBM mode is a unique CNT mode that arises from the radial expansion of the tube while the other modes are also found in graphite. Hence the RBM frequency can be used for determining the diameter

distribution of a nanotube sample. The RBM frequency (ω) is inversely proportional to the nanotube diameter with the relation

$$\omega(cm^{-1}) = A/dia(nm) + B(cm^{-1}) \quad 6\text{-}1$$

where the constants A and B have been determined experimentally with A = 223 cm^{-1}/nm and B = 10 cm^{-1} . In the case of isolated nanotubes the diameter can be directly calculated from the following relation [218].

$$\omega_r = 224/d_t \quad 6\text{-}2$$

The G-band (G- Graphite) is a tangential mode of the carbon atoms and there is a single one at ~1580 cm^{-1} in case of graphite. Whereas in CNTs this single mode transforms into several modes due to the confinement of wave-vectors along the circumference. While the higher energy branch, G^+ doesn't vary with diameter, the low energy branch, G^- gets softer for smaller diameter nanotubes. In case of semiconducting nanotubes, the highest mode G^+ = 1590 – 1595 cm^{-1} is a longitudinal optical shear mode parallel to the axis of the nanotube. While the transverse optical shear modes perpendicular to the tube axis, G^- modes are softed due to the curvature or smaller diameter, and the frequency depends on the tube diameter. The G band line shapes are lorentzian and relatively narrow even in a bundle for defect free nanotubes. In the case of metallic nanotubes the G^- band shows a broad and asymmetric Breit-Wigner-Fano line shape. The G^- band in metallic nanotubes decreases with decreasing diameter faster than semiconducting nanotubes while the G^+ remains essentially constant in frequency.

The D-band (D- Disorder) is located between 1330-1360 cm^{-1} and usually expected to be found in multi-walled nanotubes. But in SWNTs they correspond to a defect mode. The second order scattering could either be due to phonon-defect or defect-phonon scattering

which yields two Raman peaks of slightly different energies. The D to G ratio or the D to G' ratio is often used to evaluate the quality of the sample. For high quality samples usually the D/G ratio is ~< 2%. Since different nanotubes have different resonance energies, the D band frequency varies for different laser energies.

The G' band is an intrinsic property of the nanotube and graphite and is found at frequencies between 2500 – 2900 cm^{-1}. It is the second order process from the two zone boundary LO phonons with wave vectors q and –q, and is present even in defect free nanotubes.

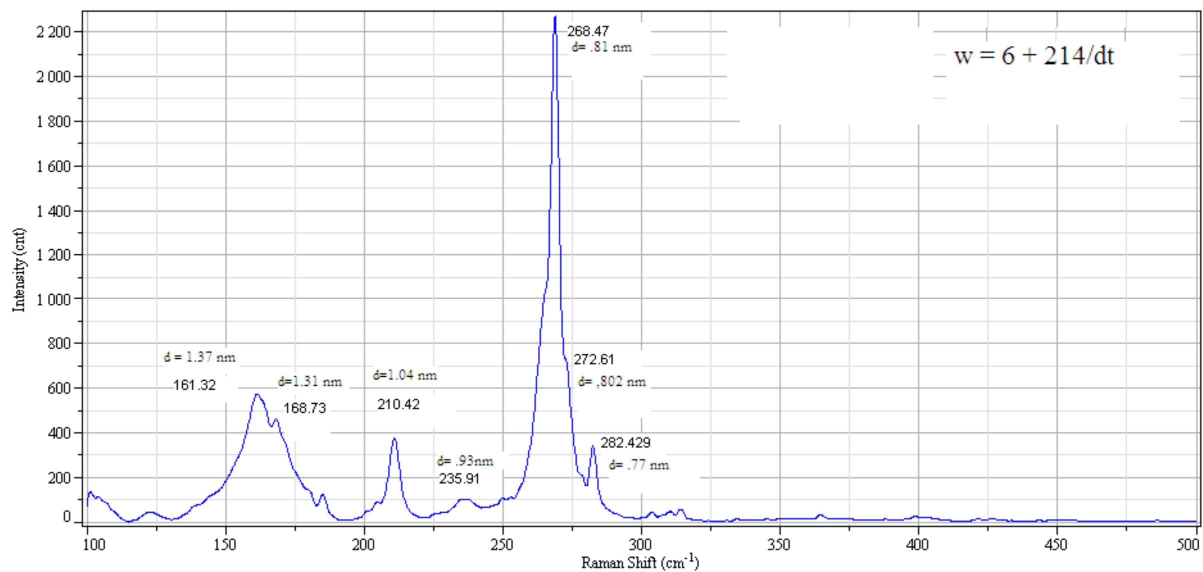

Figure B. 4: Ring Breathing mode of nantero's SWNTs along with the diameter distribution.

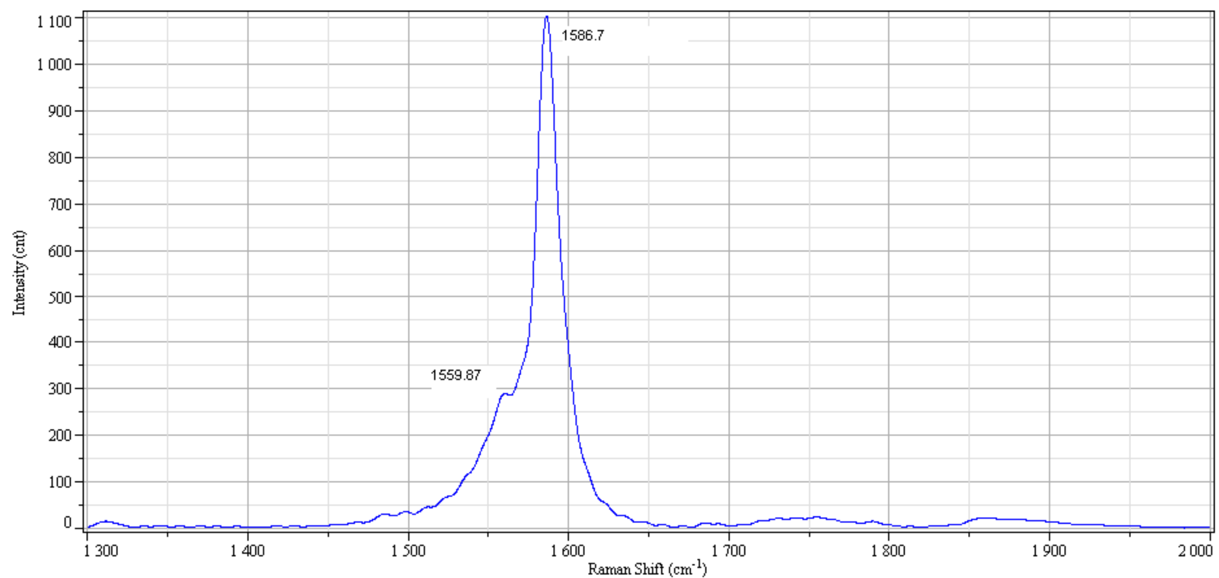

Figure B. 5: Tangential breathing mode of Nantero's SWNTs

Appendix C: Nanotube Solution

As grown carbon nanotubes are released from the substrate by either chemical or mechanical means. A series of chemical cleaning steps are used to remove metallic contaminants and catalytic particles. The pure SWNTs are then dispersed in a water based solution. The Nantero solution is compatible with any standard semiconductor fabrication process including CMOS and Silion on Insulator (SOI). Typical impurities consist of metal particles, amorphous carbon and other graphitic carbon particles. The raw SWNTs are not compatible with CMOS process flow due to the high contamination count. Moreover most solvents that readily suspend SWNTs are not permissible in CMOS fabs, hence the solubilization of the nanotubes is very important.

To address these issues, nantero uses a proprietary process that they have developed to purify, filter and solubilize the SWNTs into a semiconductor-grade solvent. This produces a sufficient metallic-free low – particulate solution that contains SWNTs with an average length of 3 µm and a diameter of 1-2 nm. . The time when this article was written, Nantero's nanotube solution was commercially available through Brewer Science Inc. The process involves the treatment of the nanotubes to a nitric acid wash. The nitric acid removes the excess metallic and catalytic nanoparticles through binding. The solution is then passed through multiple sonication and filtration steps to untangle the remaining nanotube bundles. This provides evenly dispersed individual nanotubes within a solvent volume.

It has to be noted that the mean length and chirality distribution of the resulting solution strongly depends on the growth mechanism and conditions of the raw nanotubes. Further purification steps may also contribute to the overall distribution in nanotube lengths and concentration due to defect-induced cleaving of nanotubes during the nitric acid wash. These

factors inturn affect the behavior of SWNTs during the assembly process, and any additional processing magnifies this batch to batch variation.

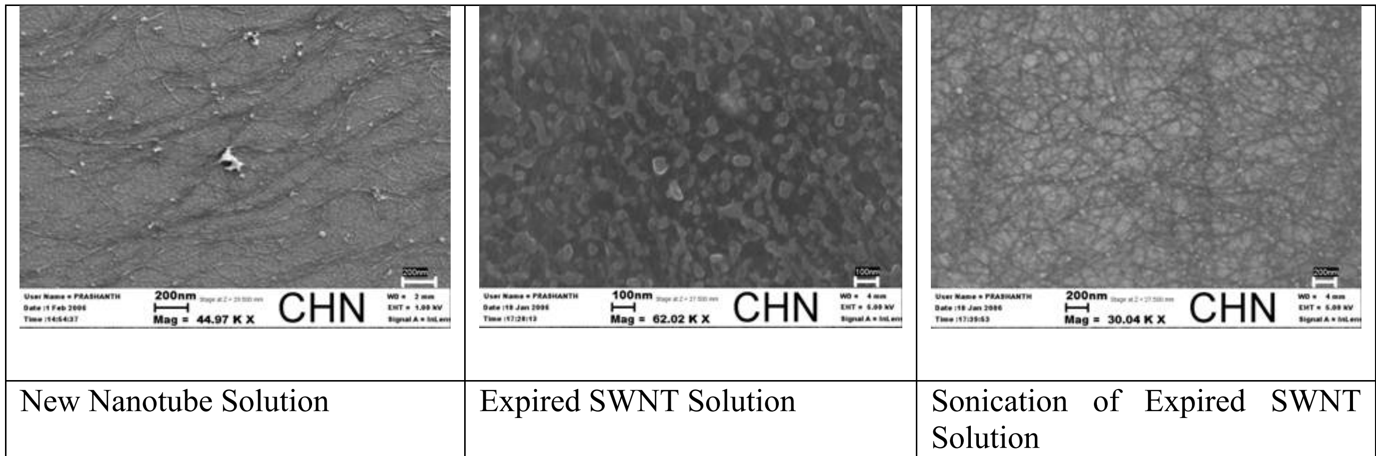

New Nanotube Solution	Expired SWNT Solution	Sonication of Expired SWNT Solution

Figure C. 1; Nantero SWNTs from a single batch during different stages of its lifetime

Figure C1 gives an example of how the nantero SWNTs look under the SEM at different stages. The lifetime of the SWNT solution is usually between 4- 6 months. After which the SWNT solution starts degrading and you can see accumulation of carbonaceous particles. Sonication of the solution momentarily stabilizes the solution, before the nanotube agglomerates again.

The expiration of the solution drastically affects the electrophoretic assembly of SWNTs. Under the influence of the electric field a mat of SWNTs get assembled on top of the trenches covering the entire trench area. But the nanotube structure is disconnected as opposed to complete mats seen when using high concentration or voltage. Moreover when PMMA is dissolved, the SWNTs come off leaving a black colored film on the gold. This film is probably due to the carbonaceous particles in the expired solution.

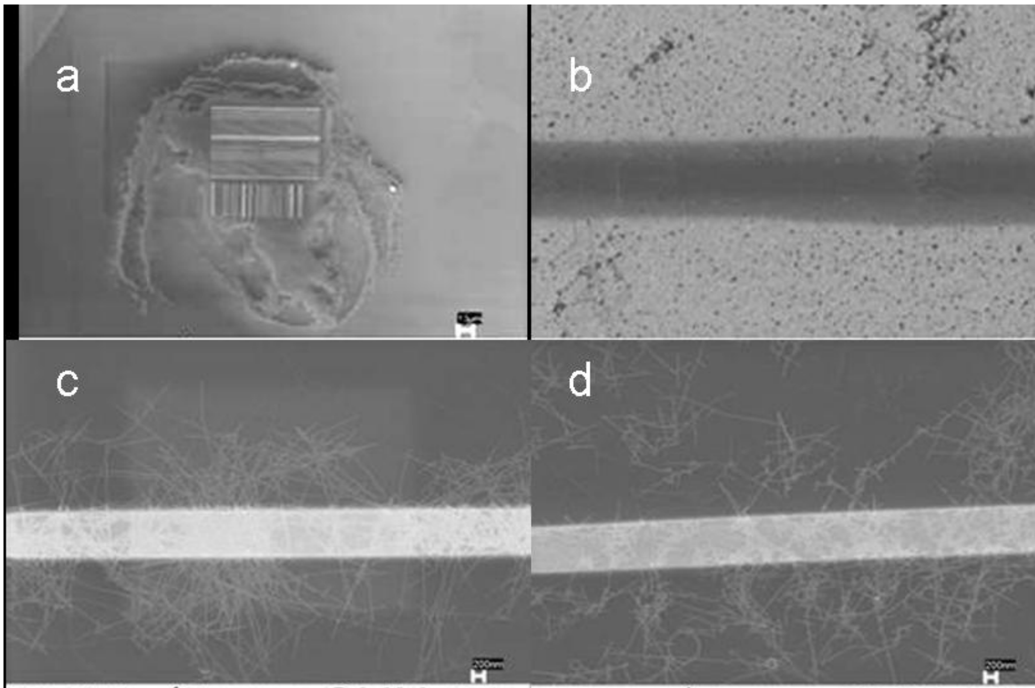

Figure C. 2: (a) Mat formation when assembling using expired SWNT solution. (b) Black coating on gold after stripping of PMMA (c) & (d) A SWNT batch that did not yield good assembly.

Every new batch of SWNT solution needs to be tested for consistency with previous batches using similar parameters. Figure C2 (c) & (d) shows a batch of SWNTs that didn't yield good assembly as previous nanotube solutions. Once the new batch of SWNTs show decent assembly results, it has to be then optimized in terms of voltage and concentration. This has to be carried out for every new batch of SWNT solution. Figure shows a flowchart designed to arrive at the optimum conditions for SWNT assembly. The flowchart assumes the withdrawal speed and pH of the solution to be constant. An example of how this technique has been adopted to optimize the Brewer Science solution is also shown.

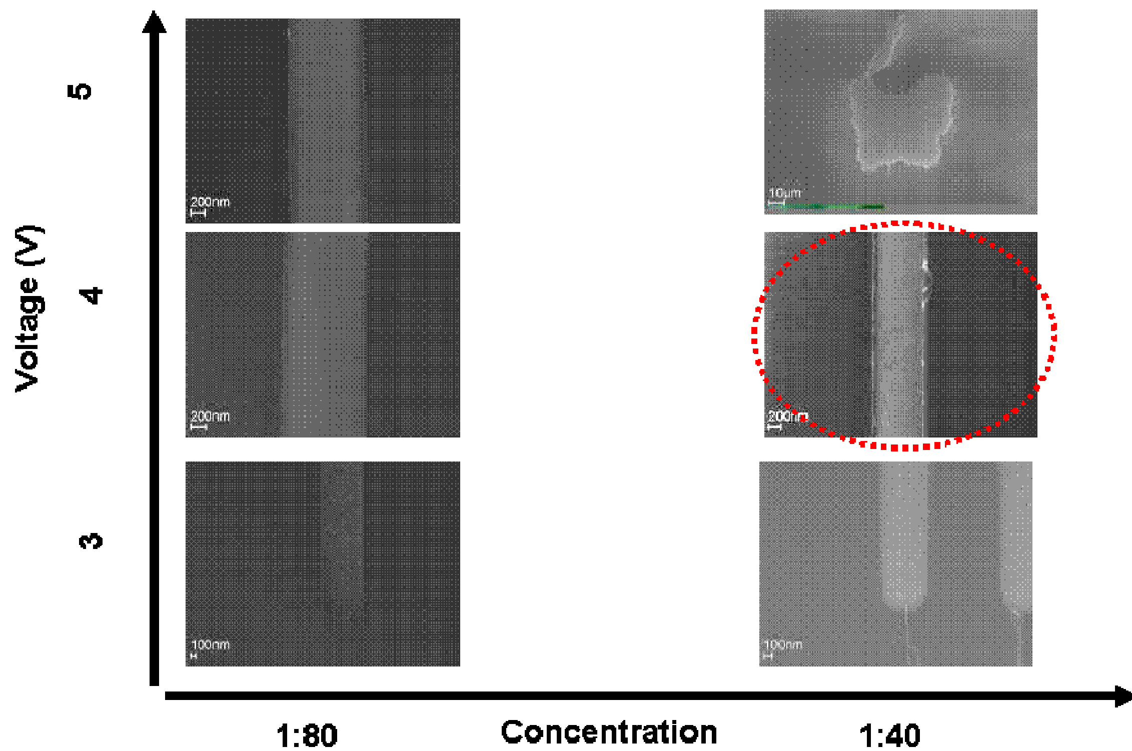

Figure C. 3: Voltage vs concentration of Brewer Sciences SWNT solution showing how to arrive at the optimum SWNT assembly conditions.

7 Bibliography

[1] Moore, G.E. *Electronics,* **1965,** *38*

[2] Dai, H. *Acc. Chem. Res.* **2002,** *35,* 1035 -1044.

[3] Ijima, S. *Nature,* **1991,** *354,* 56-58.

[4] Collins, P.G. ; Avouris, P *Scientific American,* **2000,** *63.*

[5] Bethune, D.S.; Kiang, C.-H.; de Vries, M. S.; Gorman, G.; Savoy, R.; Vazquez, J. and Beyers, R. *Nature* **1993,** *363,* 605-607.

[6] Journet C.; Maser W.K.; Bernier P.; Loiseau A.; Lamy de La Chapelle M.; Lefrant S., *Nature,* **1997,** *388*, 6644.

[7] Thess, A.; Lee, R.; Nikolaev, P.; Dai, H.; Petit, P.; Robert, J.; Xu, C.; Lee, Y.H.; Kim, S.G.; Rinzler, A.G.; Colbert, D.T.; Scuseria, G.E.; Tománek, D.; Fischer, J.E. and Smalley, R.E. *Science,* **1996,** *273,* 483.

[8] Yakobson, B.I.; Smalley, R.E. *American Scientist*, **1997,** *85*, 324.

[9] Fan, S.; Chapline, M.G.; Franklin, N.R.; Tombler, T.W.; Cassell, A.M.; and Dai, H. *Science,* **2000,** *77,* 2985.

[10] Li, W.Z.; Xie, S.S.; Qian, L.X.; Chang, B.H.; Zou, B.S.; Zhou, W.Y.; Zhao, R.A.; Wang, G. *Science,* **1996,** *274,* 1701-1703.

[11] Lee, C.J.; Lyu, S.C.; Kim, H-W.; Park, C-Y; Yang, C-W. *Chem. Phys. Lett.,* **2002,** *359,* 109-114.

[12] Hernadi, K. *Chem. Phys. Lett.* **2002,** *363,* 169.

[13] Wilson, M.; Kannangara, K.; Smith, G.; Simmons, M.; Ragues, B. *Nanotechnology: Basic Science and Emerging Technologies*l, **2002.**

[14] Ajayan, P.M.; Eddesen, T.W.; Ichihashi, T.; Ijima, S.; Tanigaki, K. And Hiura, H. *Nature,* **1993,** *362,* 522.

[15] Niu, C.; Moy, D.; Chishti, A. And Hoch, R. *Int. Patent WO 0 107694,* **2001.**

[16] Tsang, S.C. ; Chen, Y.K.; Harris, P.J.F and Green M.L.H. *Nature,* **1994,** *372,* 159.

[17] Dillon, A.C.; Gennett, T.; Jones, K.M.; Alleman, J.L.; Parilla, P.A. and Heben, M.J. *Adv. Mater.* **1999,** *11,* 1354.

[18] Dujardin, E.; Ebbesen, T.W.; Treacy, A. and Krishnan, M.M.J *Adv. Mater.* **1998,** *10,* 611.

[19] Nagasawa, S.; Yudasaka, M.; Hirahara, K.; Ichihashi, T. and Ijima, S. *Chem. Phys. Lett.* **2000,** *328,* 374.

[20] Yu, R.; Chen, L.; Liu, Q.; Lin, J.; Tan, K-L.; Ng, S.C.; Chan, H.S.O.; Xu, G.-Q. And Hor, T.S.A. , *Chem. Mater.* **1998,** *10,* 718.

[21] Delpeux, S.; Metenier, K.; Benoit, R.; Vivet, L.; Boufendi, L.; Bonnamy, S. And Begui, F. *AIP Conf. Proc.* **1999,** *486,* 470.

[22] Li, X.; Yang, Z.; Chen, Z.; Wang, H.; Li, T.; Sheng, N. And Li, J. *Xinxing Tan Cailiao,* **1999,** *14,* 32.

[23] Hiura, H.; Ebbensen, T.W. and Tanigaki, K. *Adv. Mater.* **1995,** *7,* 275.

[24] Martinez, M.T.; Callejas, M.A.; Benito, A.M.; Maser, W.K.; Cochet, M.; Andres, J.M.; Chreiber, J.; Chauvet, O. and Fierro, J.L.G. *Chem. Comm.* **2002,** 1000.

[25] Martel, R.; Shea, H.R. and Avouris, P. *J. Phys. Chem. B.* **1999,** *103,* 7551.

[26] McEuen, P.L.; Fuhrer, M.S.; Park, H., *IEEE transactions on Nanotechnology,* **2002**, *1*, 78 – 85.

[27] Tans, S.J.; Devoret, M.H.; Dai, H.; Thess, A.; Smalley, R.E.; Georliga, L.J.; Dekker, C. *Nature,* **1997,** *386,* 474-477.

[28] Bockrath, M.; Cobden, D.H.; McEuen, P.L.; Chopra, N.G.; Zettl, A.; Thess, A.; Smalley, R.E., *Science,* **1997,** *275,* 1922-1925.

[29] Tans, S.J.; Verscueren, R.M.; Dekker, C. *Nature,* **1998,** *393,* 49-52.

[30] Baughman, R.H., Zakhidov, A. A., and de Heer, W. A., *Science*, **2002,** *297*, 787-792.

[31] Tans, S.J.; Verschueren, A.R.M.; Dekker, C. *Nature,* **1998,** *393,* 49.

[32] Derycke, V.; Martel, R.; Appenzeller, J.; Avouris, P. *Nano Lett.,* **2001,** *1,* 453-456.

[33] Zhou, C.; Kong, J.; Yenilmez, E.; Dai, H. *Science,* **2000,** *290,* 1552-1555.

[34] Kong, J.; Cao, J.; Dai, H. *Appl. Phys. Lett.,* **2002,** *80,* 73.

[35] Nanpedia http://nanopedia.case.edu/NWPrint.php?page=nanofabrication

[36] Azonano http://www.azonano.com/details.asp?ArticleID=1079

[37] Dai, H.; Hafner, J.H.; Rinzler, A.G.; Colbert, D.T.; Smalley, R.E. *Nature* **1996,** *384*, 147-150.

[38] Hsu, D.S.Y.; Shaw, J. *Appl. Phys. Lett.* **2002**, *80*, 118-120.

[39] Tans, S.J.; Verschueren, A.R.M.; Dekker, C. *Nature* **1998**, *393*, 49-52.

[40] Wong, S.S.; Joselevich, E; Woolley, A.T.; Cheung, C.L.; Lieber, C.M. *Nature* **1998,** *394,* 52-54.

[41] Overney, G.; Zhong, W.; Tomanek, D.Z. *Phys. D* **1993,** *27,* 93.

[42] Ward, J.W.; Meinhold, M.; Segal, B.M.; Berg, J.; Sen, R.; Sivarajan, R.; Brock, D.K.; Rueckes, T. *IEEE* **2004,** 34-38.

[43] Javey, A.; Wang, Q.; Ural, A.; Li, Y.; Dai, H. *Nano Lett.,* **2002,** *2*, 929.

[44] Dai, L.M.; Patil, A.; Gong, X.Y.; Guo, Z.X.; Liu, L.Q.; Liu, Y.; Zhu, D.B. *ChemPhysChem* **2003,** *4,* 1150.

[45] Ago, H.; Komatsu, T.; Ohshima, S.; Uchida, K.; Kuriki, Y. And Yumura, M. *Appl. Phys. Lett.* **2000,** *77,* 79.

[46] Noda, S.; Sugime, H.; Osawa, T.; Tsuji, Y.; Chiashi, S.; Murakami, Y. and Maruyama, S. *Carbon,* **2006,** *44,* 1414.

[47] Maruyama, S.; Einarsson, E.; Murakami, Y. and Edamura, T. *Chem. Phys. Lett.* **2005,** *403,* 320.

[48] Hu, M.; Murakami, Y.; Ogura, M.; Maruyama, S. And Okubo, T. *J. Catal.* **2004,** *225,* 230.

[49] Maruyama, S.; Kojima, R.; Miyauchi, Y.; Chiaschi, S.; Kohno, M. *Chem. Phys. Lett.* **2002,** *360,* 229.

[50] Rao, C.N.R.; Sen, R.; Satishkumar, B.C. and Govindaraj, A. *Chem. Commun.* **1998,** 1525.

[51] Li, D.C.; Dai, L.; Huang, S.; Mau, A.W.H. and Wang, Z.L. *Chem. Phys. Lett.* **2000,** *316,* 349.

[52] Teo, K.B.K.; Chhowalla, M.; Amaratunga, G.A.J.; Milne, W.I.; Hasko, D.G.; Pirio, G.; Legagneux, P.; Wyczisk, F. and Pribat, D. *Appl. Phys. Lett.* **2001,** *79,* 1534.

[53] Huang, S.M.; Mau, A.W.H.; Turney, T.W.; White, P.A. and Dai, L.M. *J. Phys. Chem.B* **2000,** *104,* 2193.

[54] Zhang, Z.I.; Wei, B.Q.; Ramanath, G.; Ajayan, P.M. *Appl. Phys. Lett.* **2000,** *77,* 3764.

[55] Han, Y.S.; Shin, J.K.; Kim, S.T. *J. Appl. Phys.* **2001,** *90,* 5731.

[56] Huang, L.M.; Cui, X.D.; White, B.; O'Brien, S.P. *J. Phys. Chem. B,* **2004,** *108,* 16451.

[57] Jung, Y.J.; Homma, Y.; Vajtai, R.; Kobayashi, Y.; Ogino, T. and Ajayan, P. *Nano Lett.* **2004,** *4,* 1109-1113.

[58] Durkop, T.; Getty, S.A. , Cobas, E. and Fuhrer, M.S. *Nano Lett.* **2004,** *4,* 35.

[59] Walters, D.A.; Casavant, M.J.; Qin, X.C.; Huffman, C.B.; Boul, P.J.; Ericson, L.M.; Haroz, E.H.; O'Connell, M.J.; Smith,K.; Colbert, D.T. and Smalley, R.E. *Chem. Phys. Lett.* **2001,** *338,* 14.

[60] Rao, S.G.; Huang, L.; Setyawan, W. and Hong, S. *Nature,* **2003,** *36,* 425.

[61] Tsukruk, V.V.; Ko, H. and Peleshanko, S. *Phys. Rev. Lett.* **2004,** *92,* O65502.

[62] Bughard, M.; Duesberg, G.; Philipp, G.; Muster, J. And Roth, S. *Adv. Mater.* **1998,** *10,* 584.

[63] Oh, S.J.; Cheng, Y.; Zhang, J.; Shimoda, H. and Zhou, O. *Appl. Phys. Lett.* **2003,** *82,* 2521.

[64] Lay, M.D.; Novak, J.P. and Snow, E.S. *Nano Lett.* **2004,** *4,* 603.

[65] Hedberg, J.; Dong, L.F. and Jiao, J. *Appl. Phys. Lett.* **2005,** *86,* 143111.

[66] Kumar, M.S.; Kim, T.H.; Lee, S.H.; Song, S.M.; Yang, J.W.; Nahm, K.S. and Suh, E.K. *Chem. Phys. Lett.* **2004,** *383,* 235.

[67] Wakaya, F.; Takaoka, J.; Fukuzumi, K.; Takai, M.; Akasaka, Y.; Gamo, K. *Superlattices and Microstructures* **2003,** *34,* 401-405.

[68] Choi, W.B.; Jin, Y.W.; Kim, H.Y.; Lee, S.J.; Yun, M.J.; Kang, J.H.; Choi, Y.S.; Park, N.S.; Lee, N.S.; Kim, J.M. *Applied Physics Letters* **2001,** *78,* 1547-1549.

[69] Gao, B.; Guozhen, Z.Y.; Qiu, Q.; Cheng, Y.; Shimoda, H.; Fleming, L.; Zhou, O. *Advanced Materials* **2001,** *13,* 1770 – 1773.

[70] Kamat, P.V.; Thomas, K.G.; Barazzouk, S.; Girishkumar, G.; Vinodgopal, K. and Meisel, D. *J. Am. Chem. Soc.* **2004,** *126,* 10757.

[71] Chen, Z.; Hu, W.; Guo, J.; Saito, K. *J. Vac. Sci. Technol. B*, **2004,** *22,* 776.

[72] Li, J.; Zhang, Q.; Peng, N.; Zhu, Q. *Appl. Phys. Lett.* , **2005,** *86,* 1531161.

[73] Yamamoto, K.; Akita, S. and Nakayama, Y. *Jpn J. Appl. Phys.* **1996,** *35,* 917.

[74] Lu, J.P. *Phys. Rev. Lett.* **1995,** *74,* 1123.

[75] Walters, D.A.; Casavant, M.J.; Qin, X.C.; Huffman, C.B.; Boul, P.J.; Ericson, L.M.; Haroz, E.H.; O'Connell, M.J.; Smith, K.; Colbert, D.T. and Smalley, R.E. *Chem. Phys. Lett.* **2001,** *338,* 14.

[76] Niyogi, S.; Hangarter, C.; Thamankar, R.M.; Chiang, Y.F.; Kawakami, Myung, N.V. and Haddon, R.C. *J. Phys. Chem. B* **2004,** *108,* 19818.

[77] Long, D.P.; Lazorcik, J.L. and Shashidar, R. *Adv. Matl.* **2004,** *16,* 814.

[78] Lee, M.; Im, J.; Lee, B.Y.; Myung, S.; Kang, J.; Huang, L.; Kwon, Y. –K. and Hong. S. *Nature Nanotechnology,* **2006,** *1,* 66-71.

[79] Vijayraghavan, A.; Blatt, S.; Weissenberger, D.; Oron-Carl, M.; Hennrich, F.; Gerthsen, D.; Hahn, H. and Krupke, R. *Nano Lett.,* **2007,** *7,* 1556-1560.

[80] Lambert, P. *Capillary Forces in Microassembly,*

[81] Tian, Y.; Pesika, N.; Zeng, H.; Rosenberg, K.; Zhao, B.; McGuiggan, P.; Autumn, K.; and Israelachvili *PNAS,* **2006,** *103,* 19320 – 19325.

[82] Israelachvili, J; Maeda, N; Rosenberg, K.J.; Akbulut, M, *J Mater Res* **, 2005**, *20*,1952–1972.

[83] Israelachvili, J.N. *Intermolecular and Surface Forces*, Academic Press: London, Second ed. **(1991).**

[84] Akita, S.; Nishijima, H.; Nakayama; Y. *J. Phys. D: Appl. Phys*, **2000,** *33,* 2673-2677.

[85] Maslov, L. *Nanotechnology,* **2006,** *17,* 2475-2482.

[86] Orr, F.M.; Scriven, L.E.; Rivas, A.P. *J. Fluid Mech.* **1975,** *67,* 723-742.

[87] Scherge, M.; Gorb, S. *Biological Micro- and Nanotribology: Nature's Solutions* (Springer, Berlin, 2001)

[88] Gerdes, S.; Ondarcuhu, T.; Cholet, S. ;Joachim C. *Europhys. Lett.* **1999,** *48,* 292-298.

[89]Batchelor, G.K. *An Introduction to Fluid Dynamics,* **1967,** *1st ed.*. Cambridge University Press.

[90] Van Der Biest, O.O.; Vandeperre, L.J. *Annu. Rev. Sci.* **1999** , *29*, 327-352.

[91] Sarkar, P.; Nicholson, P.S. *J. Am. Ceram. Soc.* **1996,** *79,* 1987-2002.

[92] Zhang, Z.; Huang, Y.; Jiang, Z. *J. Am. Ceram. Soc. ,* **1995,** *78,* 3167-68.

[93] Ryan, C.B.; Stevenson, K.J.; Hupp, J.T.; *Advanced Materials* **2000**, *12*, 1930-1934.

[94] Teranishi, T.; Hosoe, M.; Tanaka, T.; Miyake, M. *J. Phys. Chem. B* **1999**, *103,* 3818.

[95] Trau, M.; Saville, D.A.; Aksay, I.A. *Science* **1996,** *272,* 706.

[96] Kumar, M.S.; Lee, S.H.; Kim, T.Y.; Kim, T.H.; Song, S.M.; Yang, J.W.; Nahm, K.S.; Suh, E.-K. *Solid-State Electronics* **2003**, *47*, 2075-2080.

[97] Du, C.; Heldbrant, D.; Pan, N. *Materials Letter* **2002**, *57,* 434-438.

[98] Wakaya, F.; Nagai, T.; Gamo, K.; *Microelectronic Engineering* **2002**, *63*, 27-31.

[99] Pohl, H. A. *J. Appl. Phys.,* 1958, *29*, 1182-1188.

[100] Pohl, H. A. *Dielectrophoresis*, Cambridge University Press, Cambridge **(1978).**

[101] Chen, Z.; Hu, W.; Guo, J.; Saito, K. *J. Vac. Sci. Technol. B*, **2004,** *22,* 776.

[102] Li, J.; Zhang, Q.; Peng, N.; Zhu, Q. *Appl. Phys. Lett.* , **2005,** *86,* 1531161.

[103]Asokan, S.B.; Jawerth,L; Carroll,R.L.; Cheney, R.E; Washburn, S.; Superfine, R, *Nano Lett*, **2003**, *3*,431-7.

[104] Dimaki M and Boggild P, 2004, *Nanotechnology*, **15**, 1-8.

[105]Yamamoto, K.; Akita, S.; Nakayama, Y. *J. Phys. D: Appl. Phys.*, **1998,** *31,* L34.

[106] Krupke, R.; Hennrich, F.; Weber, H.B.; Kappes, M.M.; Lohneysen, H.V. *Nano Lett.*, **2003,** *3,* 1019.

[107] Mureau, N.; Mendoza, E.; Silva, S.R.P.; Hoettges, K.F.; Hughes, M.P.; *Appl. Phys. Lett.,***2006,** *88,* 243109.

[108] Sao, H. W.; Han, C. S.; Choi, D.G.; Kim, K.S. and Lee, Y.H. *Microelectro. Engg.,* **2005,** *81,* 83-89.

[109] Brinker, J.C.; Hurd, A.J. *J. Phys. III France,* **1994,** *4,* 1231-1242.

[110] Huang, Y.; Duan, Z.; Wei, Q.; Lieber, C.M. *Science,* **2001,** *291,* 630 – 633.

[111] Jin, S.; Whang, D.; McAlpine, M.C.; Friedman, R.S.; Wu, Y.; Lieber, C.M. *Nano Lett. ,* **2004,** *4,* 915- 919.

[112] Oh, S.J.; Zhang, J.; Cheng, Y.; Shimoda, H.; Zhou, O. *Appl. Phys. Lett.* **2004,** *84,* 3738.

[113] Ko, H.; Tsukruk, V.V. *Nano Letters,* **2006,** *6,* 1443-1448.

[114] Biebuyck, H.A.; Whitesides, G.M. *Langmuir*, **1999,** *31*, 347.

[115] Qin, D.; Xia, Y.; Xu, B.; Yang, H.; Zhu, C.; Whitesides, G.M. *Adv. Mater.*, **1999,** *11,*

1433.

[116] Huang, Y.; Duan, Z.; Wei, Q.; Lieber, C.M. *Science,* **2001,** *291,* 630 – 633.

[117] Ko, H.; Peleshanko, S.; Tsukruk. V.V. *J. Phys. Chem. B,* **2004,** *108,* 4385-4393.

[118] Petit, C.A.P; Carbeck, J.D. *Nano Lett.,* **2003,** *3,* 1141-1146.

[119] Arnold, W.M, *Dielectrics and Electrical Insulation, IEEE Transactions on,* **2008,** *15,* 144-151.

[120] Bahukudumbi, P.; Everett, W.N.; Beskok, A.; Bevan, M.A. and Huff, G.H. *Appl. Phys. Lett.* , **2007,** *90,* 224102.

[121] Xiong, X.; Makaram, P.; Bakhtari, K.; Somu, S.; Busnaina, A.; Small, J.; Mcgruer, N. and Park, J. *Mater. Res. Soc. Symp. Proc. ,* **2006,** 0901-Ra04-01.1 – 0901-Ra04-01.5

[122] X. Xiong, *Thesis*, **2006**.

[123] Wakaya, F.; Nagai, T.; Gamo, K.; *Microelectronic Engineering* **2002**, *63*, 27-31.

[124] Kumar, M.S.; Lee, S.H.; Kim, T.Y.; Kim, T.H.; Song, S.M.; Yang, J.W.; Nahm, K.S.; Suh, E.-K. *Solid-State Electronics* **2003**, *47*, 2075-2080

[125] Wakaya, F.; Takaoka, J.; Fukuzumi, K.; Takai, M.; Akasaka, Y.; Gamo, K. *Superlattices and Microstructures* **2003,** *34,* 401-405.

[126] Sen, R.; Sivarajan, R.; Rueckes, T. and Segal, B.M. *U.S. Patent US205/02269554,* **2005.**

[127] Duggal, R.; Hussain, F. and Pasquali, M. *Advanced Materials,* **2005,** *29-34.*

[128] Bakhtari, K. *Thesis,* **2005**

[129] Kamat, P.V.; Thomas, K.G.; Barazzouk, G.; Girishkumar, G.; Vinodgopal, K ; Meisel, D., *J. Am. Chem. Soc.* **126***,* 10757 (2004).

[130] Lee, M. ; Im, J.; Lee, B.Y.; Myung, S.; Kang, J.; Huang, L.; Kwon, Y.-K.; Hong, S. *Nat. Nanotech.* **2006,** *1,* 66.

[131] Petit, C.A.P. ; Carbeck, J.D. *Nano Lett.,* **2003,** *3,* 1141.

[132] Ko, H. ; Peleshanko, S.; Tsukruk, V.V., *J. Phys. Chem.,***2004,** *B108*, 4385.

[133] Pop, P. ; Mann, D.; Reifenberg, J.; Goodson, K.; Dai, H. *IEEE-IEDM*, **2005,** 253.

[134] Albrecht, P.M.; Farrell, R.M.; Ye, W.; Lyding, J.W., *IEEE-NANO*,**2003,** 327.

[135] Sinha, N.; Ma, J.; Yeow, J.T.W., *J. Nanosci. Nanotech.* **2006,** *6,* 573.

[136] T. Someya, T.; Small, J.; Kim, P.; Nuckolls, C.; Yardley, J.T.; *Nano Lett*. **2003,** *3*, 877.

[137] Martel, R.; Schmidt, T.; Shea, H.R.; Hertel, T.; Avouris, Ph. *Appl. Phys. Lett.* **1998,** *73,* 2447.

[138] Liu, L. ; Jayanthi, C.S.; Tang, M.J.; Wu, S.Y.; Tombler, T.W.; Zhou, C.; Alexseyev, L.; Kong, J.; Dai, H. *Phys. Rev. Lett.* **2000**, *84,* 4950.

[139] Ozcan, C.; Hasrici, N. *J. Biomed. Sci.* , **2007,** *18,* 759 -773.

[140] Hu, H; Yu, A; Kim, E.; Zhao, B.; Itkis, M.E.; Bekyarova, E.; Haddon, R.C. *J. Phys. Chem. B,* **2005,** *109,* 11520 – 11524.

[141] Darhuber, A.A.; Troian, S.M.; Davis, J.M.; Miller, S.M.; Wagner, S. *J. Appl. Phys.* **2000,**

88, 5119.

[142] Gerdes, S.; Ondarcuhu, T.; Cholet, S.; Joachim, C. *Europhys. Lett.* **1999,** *48,* 292-298.

[143] Joanny, J.F; De Gennes, P.G. *J. Chem. Phys.* **1984,** *81,* 552.

[144] Petit, C.A. P.; Carbeck, J.D. *Nano Letters,* **2003,** *3,* 1141-1146.

[145] Vitard, M.; Regnier, S.; Lambert, P. *IEEE International Sumposium on Assembly and Manufacturing,* **2007,.**

[146] Schwartz, J.A.; Contescu, C.I. and Putyera, K. *Dekker Encyclopedia of Nanosciences and Nanotechnology*

[147] Werder, T.; Walther, J.H.; Koumoutsakos, P. *Technical Proceedings of the 2002 International Conference on Computational Nanoscience and Nanotechnology, Vol 2,* **2002** *,* 490-493.

[148] Israelachvili, J.N. *Intermolecular and Surface Forces*, Academic Press: London, Second ed. (1991).

[149] S. Akita, H. Nishijima, Y. Nakayama *J. Phys. D: Appl. Phys*, **2000,** *33,* 2673-2677.

[150] L. Maslov, *Nanotechnology,* **2006,** *17,* 2475-2482.

[151] Hu, J.J.; Jo, S.H.; Ren, Z.F.; Voevodin, and Zabinski, J.S. *Tribol. Lett.,* **2005,** *19,* 119-125.

[152] Tu, J.P.; Jiang, C.X.; Guo, S.Y.; Zhao, X.B. and Fu, M.F. *Wear,* **2005,** *259,* 759-764.

[153] Dickrell, P.L.; Pal, S.K.; Bourne, G.R.; Muratore, C.; Voevodin, A.A.; Ajayan, P.M.; Schadler, L.S. and Sawyer, W.G. *Tribol Lett,* **2006,** *24,* 85-90.

[154] Dickrell, P.L.; Sinnott, S.B.; Hahn, D.W.; Raravikar, N.R.; Schadler, L.S.; Ajayan, P.M. and Sawyer, W.G. *Tribol Lett.,* **2005,** *18,* 59-62.

[155] Tzeng, Y. *App. Phys. Lett.,* **1993,** *63,* 3586-3588.

[156] Xiong X, Jaberansari L, Hahm MG, Busnaina A, Jung YJ. *Small,* **2007,** *12,* 2006-10.

[157] Bakthari, K.; *PhD Thesis,* **2005.**

[158] Deegan, R.D.; Bakajin, O.; Dupont, T.F.; Huber, G.; Nagel, S.R.; Witten, T.A. *Nature,* **1997,** *389,* 827.

[159] Fischer, B.J. *Langmuir,* **2002,** *18,* 60.

[160] De Gennes, P.G. *Rev. Mod. Phys.,* **1985,** *57,* 827.

[161] Liddle, J.A.; Cui, Y.; Alivisatos, P. *J. Vac. Sci. Technol. B,* **2004,** *22,* 3409-3414.
[162] Tans, S.J.; Devoret, M.H.; Dai, H.; Thess, A.; Smalley, R.E.; Georliga, L.J. and Dekker, C. *Nature,* **1997,** *386,* 474-477.

[163] Tans, S.J.; Verschueren, R.M. and Dekker, C. *Nature,* **1998,** *393,* 49-52.

[164] McEuen, P.L.; Fuhrer, M.S.; Park, H. *IEEE Transactions on Nanotechnology*, **2003,** *1*).

[165] Kreupl, F. ; Graham, A.P.; Liebau, M.; Duesberg, G.S.; Seidel, R.; Unger, E. *International Device Meeting, IEDM Technical Digest*, **2004.**

[166] Hecht, D.; hu, L.; Gruner, G.; *Appl. Phys. Lett.,* **2006,** *89,* 133111.

[167] Collins, P.G.; Arnold, M.S.; Avouris, P. *Science,* **2001,** *292,* 706- 708.

[168] Snow, E.S.; Novak, J.P.; Campbell, P.M.; Park, D. *Appl. Phys. Lett.,* **2003,** *82*, 2145.

[169] Collins, P.G.; Arnold, M.S.; Avouris, Ph. *Science* **2001,** *292*, 706.

[170] Bachtold, A.; Hadley, P.; Nakanishi, T.; Dekker, C. *Science,* **2001,** *294*, 1317-1320.

[171] Martel, R.; Dervcke, V.; Lavoie, C.; Appenzeller, J.; Chan, K.K.; Tersoff, J.; Avouris, P. *Phys. Rev. Lett.,* **2001,** *87*, 256.

[172] Snow, E.S.; Campbell, P.M.; Ancona, M.G.; Novak, J.P. *Appl. Phys. Lett.,* **2005,** *86*, 033105.

[173] Yu, Z.; Burke, P.J. *SPIE,* **2005**.

[174] Al-sarawi, S. F.; Abbott, D.; Franzon, P. D. *IEEE Trans. Components, Pkg. & Manuf. Technol. B* **1998,** *21*, 1.

[175] Ieong, M.; Guarini, K.W.; Chan, V.; Bernstein, K.; Joshi, R.; Kedzierski, J.; Haensch, W. *Proceedings of the IEEE Custom Integrated Circuits Conference*, **2003**, 207–213.

[176] Long , D.P.; Lazorcik, J. L.; Shashidhar, R. *Adv. Matl.* **2004,** *16,* 814.

[177] Wang, Y.; Maspoch, D.; Zou, S.; Schatz, G.C.; Smalley, R.E.; Mirkin, C.A. *PNAS,* **2006,** *103,* 2026-2031.

[178] Yamamoto, K.; Akita, S.; Nakayama, Y. *J. Phys. D: Appl. Phys.*, **1998,** *31,* L34.

[179] Nihei, M.; Horibe, M.; Kawabata, A.; Awano, Y. *J. Appl. Phys,* **2004,** *43,* 1856.

[180] Graham, A.P.; Duesberg, G.S.; Kreupl, F.; Seidel, R.; Liebau, R.; Unger, E.; Honlein, W. *Diamond and related materials*, **2004,** *13,* 1296.

[181] Nihei, M. ; Horibe, M.; Kawabata, A.; Awano, Y. *J. Appl. Phys,* **2004,** *43,* 1856.

[182] Graham, A.P.; Duesberg, G.S.; Kreupl, F.; Seidel, R.; Liebau, R.; Unger, E.; Honlein, W. Diamond and related materials, **2004,** *13,* 1296.

[183] Li, J. ; Ye, Q.; Cassell, A.; Ng, H.T.; Stevens, R.; Han, J.; Meyyappan, M. *Appl. Phys. Lett.*, **2003,** *82,* 2491.

[184] Yamamoto, K.; Akita, S.; Nakayama, Y. *J. Phys. D: Appl. Phys.*, **1998,** *31,* L34.

[185] Krupke, R.; Hennrich, F.; Weber, H.B.; Kappes, M.M.; Lohneysen, H.V. *Nano Lett.*, **2003,** *3,* 1019.

[186] Mureau, N.; Mendoza, E.; Silva, S.R.P.; Hoettges, K.F.; Hughes, M.P. *Appl. Phys. Lett.* **2006,** *88***,** 243109.

[187] Chen, Z.; Hu, W.; Guo, J.; Saito, K. *J. Vac. Sci. Technol. B*, **2004,** *22,* 776.

[188] Li, J.; Zhang, Q.; Peng, N.; Zhu, Q. *Appl. Phys. Lett.* , **2005,** *86,* 1531161.

[189] Fan D.L.; Zhu F.Q.; Cammarata R.C.; Chien C.L. *App. Phys. Lett.,* **2004,** *85,* 4175.

[190] Krupke, R; Hennrich, F; Lohneysen, H; Kappes, M.M.; *Science,* **2003,** *301,* 344.

[191] Seo, H-W; Han, C- H; Choi, D-G; Kim, K-S; Lee, Y-H, *Microelectronic Engg.* **2005,** *81,* 83.

[192] Peng, H; Alvarez, N.T.; Kittrell, C.; Hauge, R.H.; Schmidt, H.K., *J. Am. Chem. Soc.* **2006,** *128,* 8396.

[193] Lewenstein, J.C.; Burgin, T.P.; Ribayrol, A.; Nagahara, L.A.; Tsui, R.K. *Nano Lett.* **2002**, *5* **,**443.

[194] de Pablo, P.J.; Gomez-Navarro, C.; Cochero, J.; Serena, P.A.; Gomez-Herrero, J.; Baro,A.M; *Phys. Rev. Lett.*, **2002**, *88*, 036804-1.

[195] Lewenstein, J.C.; Burgin, T.P.; Ribayrol, A.; Nagahara, L.A.; Tsui, R.K. *Nano Lett.* **2002,** *5* **,**443.

[196] de Pablo, P.J.; Gomez-Navarro, C.; Cochero, J.; Serena, P.A.; Gomez-Herrero, J.; Baro,A.M; *Phys. Rev. Lett.*, **2002**, *88*, 036804-1.

[197]Asokan, S.B.; Jawerth, L.; Carroll, R.L.; Cheney,R.E; Washburn, S.; Superfine, R. *Nano Lett*, **2003,** *3,*431-7.

[198] Dimaki,M.; Boggild, P., *Nanotechnology*, **2004,** *15,* 1-8.

[199] Benedict, L.X.; Louie, S.G.; Cohen, M.L. *Phys. Rev.* B **1995,** *52,* 8541 – 9.

[200] Ding, J.W.; Yan, X.H.; Cao, J.X. *Phys. Rev. B,* **2002,** *66,* 073401.

[201] Leonard, F.Tersoff, J. *Appl Phys. Lett.* **2002,** *81,* 4835.

[202] Martel, R; Schmidt, T; Shea, H.R.; Hertel, T.; Avouris, Ph. *Appl. Phys. Lett.* **1998,** *4***,** 35.

[203] Zhou, C; Kong, J.; Dai, H. *Phys. Rev. Lett.* **2000,** *84,* 5604.

[204] Javey, A.; Shim, M.; Dai, H. *Phys. Rev. Lett.* **2000,** *80***,** 1064.

[205] Jones,T.B.; *Electromechanics of particles; Cambridge University Press: Cambridge; New York,* **1995**.

[206] Stratton, J.A.; *Electromagnetic theory, 1st ed.; MaGraw-Hill: New York, London,* **1941**.

[207] The George Kostas facility http://kostas.coe.neu.edu

[208] http://www.icmm.csic.es/fis/g/evaporacion_electrones_in.gif

[209] MicroChem Corp. http://www.microchem.com/

[210] Transene Company Inc. http://www.transene.com/au_etchant.html

[211] Transene Company Inc. http://www.transene.com/cr.html

[212] http://www.ionbeammilling.com/about.html

[213] Binnig, G.; Quate, C.F.; Gerber,Ch.; *Phys. Rev. Lett.* **1986,** *56(9)*, 930-933

[214] de Gennes, P.G. *Reviews of Modern Physics*, **July 1985**, *57, 3 (part I)* , p.827-863

[215] Israelachvili, J. *Intermolecular and Surface Forces*, *Academic Press* **1985-2004.**

[216]Van Krevelen, D.W. *Properties of Polymers*, *2nd revised edition, Elsevier Scientific Publishing Company, Amsterdam-Oxford-New York* **1976.**

[217] Ferraro, J. *Introductory Raman Spectroscopy*, *Academic Press,* **2002**.
Smith, E. ;Dent, G. *Modern Raman Spectroscopy*, *Wiley,* **2005**.

[218] Dresselhaus; Eklund , *Adv. Physics*, **2000,** *49,* 705-814.

PUBLICATIONS

- Makaram. P.; Selvarash, S.; Xiong, X.; Chen, C-L.; Busnaina, A.; Khanduja, N. and Dokmeci, M.R. **Three Dimensional Assembly of Single-Walled Carbon Nanotube Interconnects using Dielectrophoresis,** *Nanotechnology,* **2007,** *18,* p395204 **(featured article).**
- Makaram, P.; Somu, S.; Xiong, X.; Busnaina, A., Jung, Y., J. and McGruer, N. **Scalable Nanotemplate Assisted Directed Assembly of Single Walled Carbon Nanotubes for Nanoscale Devices,** *Appl. Phys. Lett.,* **2007,** *90,* p243108**.**
- Xiong, X.; Makaram, P.; Busnaina, A.; Bakhtari, K.; Somu, S.; McGruer, N. and Park, J. **Large Scale Directed-assembly of Nanoparticles Using Nanotrench Templates,** *Appl. Phys. Lett.,* **2006,** *89,* p. 193108.
- Xiong, X.; Busnaina, A.; Selvarasah, S.; Somu, S.; Wei, M.; Mead, J.; Chen, C-L.; Aceros, J.; Makaram, P. and Dokmeci, M.R. **Directed Assembly of Gold Nanoparticle Nanowires and Networks for Nanodevices,** *Appl. Phys. Lett.* **2007,** *91,* p. 063101.
- Khanduja, N.; Selvarasah, S.; Xiong, X.; Makaram, P.; Chen, C-L.; Busnaina, A.and Dokmeci, M.R. **Three Dimensional Controlled Assembly of Gold Nanoparticles using a Micromachined Platform,** *Appl. Phys. Lett. ,* **2007,** *90,* p. 083105.
- Guldiken, O.O; Makaram, P.; Bakhtari, K.and Busnaina, A.A. **Nanoparticle scanning and detection on flat and structured surfaces using fluorescence microscopy,** *Microscopy Research and Technique* **(Accepted 2007).**
- Bakhtari, K.; Guldiken, R.; Makaram, P.; Busnaina, A.A.; and Park, J-G. **Experimental and Numerical Investigation of Nanoparticle Removal Using Acoustic Streaming and the Effect of Time,** *Journal of Electrochemical Society,* **2006.,** *153,* G846 – G850.

CONFERENCES

- Makaram, P.; Selvarash, S.; Chen, C.; Busnaina, A. and Dokmeci, M.R. **Single Walled Carbon Nanotubes based Three Dimensional Flexible Electronics,** *NSTI Nanotech – Santa Clara, USA,* **2007.**
- Makaram, P.; Busnaina, A.; Jung, Y.J. and McGruer, N. **Controlled Assembly and Orientation of Single Walled Nanotubes using Electrophoresis for Nanoelectronic Applications,** *NSTI Nanotech – Santa Clara, USA,* **2007.**
- Khanduja, N.; Selvarasah, S.; Makaram, P.; Chen, C-L.; Busnaina, A. and Dokmeci, M.R. **Three Dimensional Dielectrophoretic Assembly of Single-Walled Carbon Nanotubes for Integrated Circuit Interconnects,** *20th International Conference on Micro Electro Mechanical Systems – Kobe, Japan,* **2007.**
- Khanduja, N.; Selvarasah, S.; Xiong, X.; Makaram, P.; Chen, C-L.; Busnaina, A.and Dokmeci, M.R. **A Micromachined Platform for Three Dimensional Dielectrophoretic Assembly of Gold Nanoparticles for Nanodevices,** *2nd IEEE International Conference on Nano/Micro Engineered and Molecular Systems – Bangkok, Thailand,* **2007.**
- Selvarasah, S.; Makaram, P.; Chen, C.L.; Chao, S.H.; Busnaina, A.; and Dokmeci, M.R. "**A Three Dimensional Thermal Sensor Based on Single-Walled Carbon Nanotubes**", *Proceedings of the 14th International Conference on Solid-State Sensors, Actuators and Microsystems (Transducers '07)*, *Lyon, France*, June 10-14 **2007**.
- Selvapraba, S.; Khanduja, N.; Chen, C.L.; Chao, S.H.; Makaram, P.; Busnaina, A.; Dokmeci, M.R., "**Three Dimensional Dielectrophoretic Assembly of Nanostructures on a Micromachined Platform**", *8th International Symposium on MEMS and Nanotechnology, Springfield, MA*, **2007**.
- Chen, C.L.; Lopez, E.; Makaram, P.; Busnaina, A.; Jung, Y.J.; Muftu, S. and Dokmeci, M.R. "**Fabrication and Evaluation of Carbon Nanotube-Parylene Functional Composite-Films**", *Proceedings of the 14th International Conference on Solid-State Sensors, Actuators and Microsystems (Transducers '07*), *Lyon, France*, June 10-14 **2007**.
- Makaram, P.; Xiong, X.; Bakhtari, K.; Busnaina, A.A.; and Miller, G. **SWNT Directed Assembly Using Nanotemplates,***MRS Fall Meeting Symposium- Boston,* **2005.**

- Busnaina, A.A.; Bakhtari, K.; Xiong, X.; and Makaram, P. **Directed Assembly and Control of Nanoparticles,** *MRS Fall Meeting Symposium- Boston,* **2005.**
- Xiong, X.; Makaram, P.; Bakthari, K.; Busnaina, A.A.; Small, J.; Somu, S.; Miller, G.; and Park, J. **Directed Assembly of Nanoelements Using Electrostatically Addressable Templates,** *MRS Fall Meeting Symposium- Boston,* **2005.**
- Bakhtari, K.; Guldiken, R.; Makaram, P.; Busnaina, A.A.; and Park, J-G. **Removal Of Nano Scale PSL Particles Using Acoustic Streaming**, *Proceedings 28th Annual Meeting of the Adhesion Society, Inc.*, *Alabama* **2005**.

ISSN 0957-4484

NANOTECHNOLOGY

Volume 18 Number 39 3 October 2007

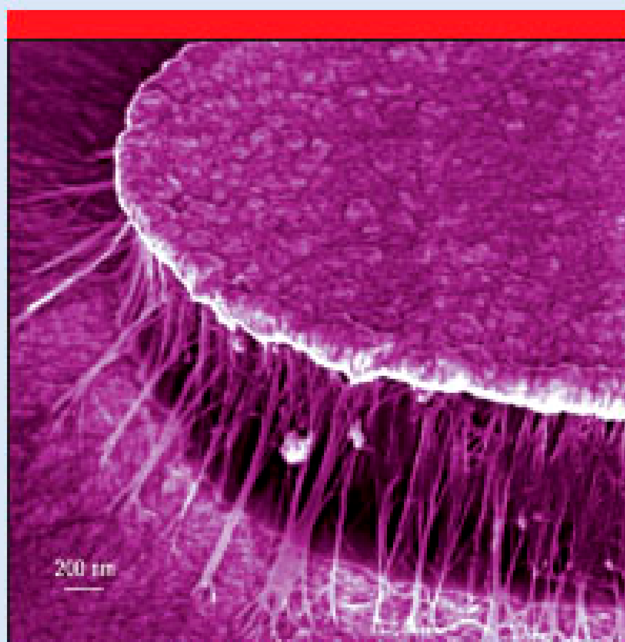

www.iop.org/journals/nano

Featured article:
Three-dimensional assembly of single-walled carbon nanotube interconnects using dielectrophoresis
P Makaram, S Selvarasah, X Xiong, C-L Chen, A Busnaina, N Khanduja and M R Dokmeci

IOP Publishing